Development of a Numerical Approach for the Simulation of Boatlanding Maneuvers

Vom Promotionsausschuss der
Technischen Universität Hamburg

zur Erlangung des akademischen Grades

Doktor-Ingenieur (Dr.-Ing.)

genehmigte Dissertation

von
Daniel Ferreira González

aus
Münster

2023

Vorsitzender des Prüfungsausschusses

Prof. Dr.-Ing. Jürgen Grabe

Gutachter

1. Prof. Dr.-Ing. Moustafa Abdel-Maksoud
2. Prof. Dr.-Ing. habil. Alexander Düster

Tag der mündlichen Prüfung

5. April 2023

Digital Object Identifier (DOI): 10.15480/882.5111

Summary

The present thesis deals with the development of a numerical method for the simulation of boat-landing maneuver at offshore platforms. The approach is based on a boundary panel method, and it is able to compute the boat-landing maneuver in the time domain considering the non-linear effects with a moderate effort regarding the modeling and the computation time. Within this thesis, an approach for the consideration of the non-linear free water surface has been derived. It is based on the mixed-Eulerian-Lagrangian method. Furthermore, a method to solve the acceleration potential is included to the approach. This is an important aspect for the free motion simulation of the crew transfer vessel regarding the computed hydrodynamic forces which particularly improves the numerical stability of the time integration of the motion. In addition to this, a simplified contact model is applied to solve the contact problem between the bow fender of the crew transfer vessel and the boat-landing structure. The model computes the reaction forces due to the deformation of the fender and it is able to describe the friction forces in the tangential direction of the contact plane. Here, the model distinguishes between static and kinetic friction and can therefore detect whether the fender slips or not during the landing maneuver.

Supplementary to the development of the numerical simulation approach, the boat-landing maneuver is investigated experimentally. A new approach to measure the wave elevation using optical infra-red cameras is presented. It allows evaluating the wave field in circumstance of the monopile and the diffraction effects. The second part of the experimental investigation deals with the boat-landing maneuver itself. Within these tests, the motion of catamarans and the forces at the boat-landing are measured in regular and irregular waves considering different encounter angles of the waves.

The developed numerical method is validated considering several hydrodynamic problems, for example, the non-linear wave forces on a monopile and the motion of a Wigley hull with forward speed in waves. The simulation of the boat-landing maneuver is validated by comparing the numerical results with model test data for two different crew transfer vessels in regular and irregular waves. The response amplitude operators for the motion in regular waves are compared for a freely-moving catamaran in the circumstance of the monopile and for a catamaran in contact with the boat-landing structure. Furthermore, the validation is done for the boat-landing maneuver in irregular waves. In general, the results are satisfactory as the motion of the vessel fairly match the tank test data and the results further prove that the simulation approach is able to forecast the occurrence of slip during the maneuver.

In conclusion, a numerical method for the simulation of a boat-landing maneuver is developed of which numerical effort regarding the setup and the computation is relatively small compared to more sophisticated fluid-structure interaction approaches using finite volume methods. Furthermore, it has been demonstrated within the presented work that the developed method can consider non-linear effects, and that it is a suitable and efficient approach to simulate the safety relevant aspects of the maneuvers at offshore platforms.

Acknowledgments

This work was carried out during my engagement at the Institute for Fluid Dynamics and Ship Theory at Hamburg University of Technology.

I am especially grateful to my supervisor Professor Moustafa Abdel-Maksoud for the helpful discussions, all his advices and the support during all phases of this research. Moreover, I sincerely appreciate the freedom he provided to pursue own ideas and the opportunity to present my work at conferences to an international audience.

I thank Professor Jürgen Grabe for chairing the examination and Professor Alexander Düster for reviewing the thesis and for the fruitful cooperation in the joint research project *Maritime Safety Aspects Regarding Installation and Maintenance of Offshore Wind Turbines* in which the foundations for this thesis were laid. The project was sponsored by the *Hamburg Behörde für Wissenschaft und Forschung* whose financial support is acknowledged.

Special thanks go to my colleagues on the fifth deck for the inspiring atmosphere. In particular, I thank my roommate Ulf Göttsche for all the interesting discussions and for opening up a whole new world for me, full of static casts, dynamic memory allocation and segmentation faults. Furthermore, the helpful contributions within student research projects of Raphael Bévand and Jonas Bechthold related to various parts of this thesis are highly appreciated.

I am very thankful to my parents and my siblings for their encouragement and motivation during all stages of my educational and academic career. Most of all, I thank my wife Sandy and my two kids Victor and Alba for their love, patience and support.

Hamburg, May 10, 2023
Daniel Ferreira González

Contents

1. Introduction

In the last decades, the offshore wind industry has grown strongly. According to the annual report of the European wind energy association WindEurope (2020), approximately one hundred wind farms have been installed by the end of 2019 and more than five thousands offshore wind turbines have been connected to the mains.

In addition to the difficulties associated with the installation, one of the most challenging tasks for the offshore wind industry is the optimization of the procedure for repairing and maintaining the turbines. For this procedure maintenance and repair staff and equipment of the wind farm operator have to be brought to the respective turbine plants. In contrast to onshore wind turbines, their accessibility is restricted not only due to the exposed location but also due to the harsh environmental conditions at sea. Therefore, the maintenance and repair are very cost- intensive. As the use of helicopters is much more costly and limited to relatively light weight cargo, it is common practice to do the transport by service vessels, so-called crew tranfer vessels (CTV). Often these CTVs are of catamaran type and they are relatively small compared to other offshore supply vessels. Their length mainly ranges between 15 m – 40 m.

The transfer of personnel and equipment to the offshore turbine plant is relatively time-consuming and the time window in which the weather conditions allow the approach is often limited. The transfer process can be subdivided into three stages. First, the transfer from the harbor to the wind farm, second, the approach to the turbine foundation and third, the boat-landing maneuver, in which the vessel is in contact with the foundation so that the embarkation and disembarkation of personnel and equipment can be done. This last stage represents the most crucial part of the transfer. Here, the vessel presses its bow fender against the so-called boat-landing structure of the foundation, which generally consists of two vertical pipes that are supported by stiff struts.

The contact between fender with rubber similar material and boat-landing provides a vertical friction force, which in turn should keep the bow of the vessel at rest. Here, loose contact instead of a fixed connection between vessel and boat-landing structure is intended since the forces due to the hydrodynamic wave loads may become too high for either the connection or the vessel which then would be damaged or destroyed.

The dynamic behavior of the bow fender that means whether the fender of the vessel actually remains fixed or starts to slide depends on several parameters. The most important factors are the hydrodynamic loads due to waves and current, the motion behavior of the vessel and the characteristic of the contact between fender and boat-landing, in particular, regarding the properties of friction. It is imperative to limit the relative motion between fender and structure, but even though the fender finds a rest position, the situation remains safety-critical as the fender still could suddenly start to slip, thus vessel and equipment may be damaged or, even worse, personnel may be harmed.

For example, such a sudden slip may be caused by unexpected waves with high amplitudes and the consequently high hydrodynamic loads or if the thrust of the vessel falls down. Latter effect can occur when the propeller operates very close to the water surface and starts to ventilate but also when the engine or the propulsion system fails due to the very high loading during the bollard pull condition. In practice, the captain of the respective vessel is responsible for safe execution of the boat-landing maneuver. Unfortunately, up to today the decision if the maneuver is safe or not is mostly made based on experience as there is still a lack of secured data and knowledge regarding this maneuver.

In April 2020 a CTV collided with a wind turbine foundation[1] at the wind-farm *Borkum Riffgrund 1*. Due to the collision, the bow of the ship was torn open over a length of half a meter and three crew members were injured, one of them seriously. According to the news, the water police suspected that the collision occurred during the boat-landing maneuver and was caused by violent waves or a technical defect. This recent accident exemplarily shows the considerable risk of the boat-landing maneuver and the importance to make it as safe as possible.

In this regard, a better understanding of the governing influences and the complex interactions between waves, vessel and offshore foundation is needed to be able to initially define operational limits more precisely and, then to improve the accessibility to the offshore turbine plant as well as the safety during the landing operation. In this context, scientific investigations are important in order to gain more insight into the whole maneuver and the interacting physical effects.

In addition to experimental approaches, which are relatively time-consuming and cost-intensive, an important tool for scientific investigations are numerical simulations. Due to the complexity of the problem simple mathematical approaches do not seem appropriate. On the one hand, an accurate and efficient method is needed to solve the strongly-coupled interaction problem that involves the motion of the vessel in waves and the contact forces between fender and boat-landing struts in an accurate manner. On the other hand, the computational effort should not be excessive as a relatively high number of cases should be taken into account for simulations of the dynamic behavior of bodies in waves.

[1] Homepage Offshore Wind magazine `https://www.offshorewind.biz/2020/04/24/three-injured-after-ctv-hits-wind-turbine-at-german-offshore-wind-farm/`

Currently existing simulation approaches concerning wave-body interactions either do not appropriately take into account the forces caused by the contact between fender and offshore structure or they are based on finite-element- or finite-volume-methods that therefore have a relatively high consumption of CPUs (central processing units) and memory. Due to this, the aim of this thesis is the development of a simulation method that computes the motion of a vessel during the boat-landing maneuver in an efficient but also accurate manner. Apart from the computation of the hydrodynamic loads of the waves and the motion response of the vessel, the method should take into account the forces caused by the contact between fender and boat-landing structure and it should distinguish between non-slip and slip condition.

The development of the numerical method has been part of the joint research project *Maritime Safety Aspects Regarding Installation and Maintenance of Offshore Wind Turbines* sponsored by the Hamburg Research and Science Foundation. Within this project, the work package *Simulation of safety-relevant situations regarding the interaction of service ships with offshore wind turbine plants* has been an elaborated cooperation with the Institute for Ship Structural Design and Analysis.

1.1. State of the Art

In general, hydrodynamic problems can be analyzed by experimental or numerical investigations. From the hydrodynamic point of view, the boat-landing maneuver is a seakeeping problem, in which the waves, the monopile and the moving vessel are interacting. Concerning the simulation of such seakeeping problems, methods applying a linearized free surface condition were widely applied in the past. Examples are methods based on strip theory or using wave Green function in the frequency domain. Latter approach is used by Yang et al. (2019) who investigated the motion behavior of a crew transfer vessel. The work, however, did not take into account the boat-landing maneuver itself. On the one hand, the linearization allows a fast computation and reduces the required memory capacity but on the other hand, these methods are limited regarding their application. For example, frequency domain methods assume that the entire hydrodynamic forces and all other influences are harmonically oscillating with the respective wave frequency. This assumption in turn, is not valid for many seakeeping problems, in particular, not for problems in which non-linear contact forces have an effect.

Also other non-linearities concerning the simulation of boat-landing maneuvers have to be considered, which would violate the linear assumptions of frequency domain methods:

- The friction forces at the fender generally are strongly non-linear.
- The vessel water line area may change significantly as the vessel does not follow the wave contour if its bow fender sticks to the boat-landing structure.

- The equilibrium position of the vessel changes if the bow fender starts to slide and remains stuck at an higher or lower position than before.

Consequently, frequency domain methods can hardly be used for the simulation of boat-landing maneuvers. In contrast to this, time domain methods can describe non-linear forces and motions, so that they are able to handle the special aspects of the landing maneuver. According to the final report and recommendation of the seakeeping committee of *Proceedings of the 27th International Towing Tank Conference* (2013) another advantage of time domain methods is that they can be more easily coupled or extended with other methods in order to include, for example, external force models for the propulsion or control devices.

Table 1.1 which is taken from *Proceedings of the 26th International Towing Tank Conference* (2011) gives an overview of existing time-domain approaches for the simulation of seakeeping problems. According to this, CFD methods solving field equations, like Euler or *Reynolds-Averaged Navier-Stokes* (RANS) equations, have the capability to compute the hydrodynamic loads accurately and to simulate violent ship motion. Luo-Theilen and Rung (2017) presented simulations of the landing maneuver using a finite volume method, which solves RANS equations, for the computation of the hydrodynamic forces and the resulting body motions. Here, the characteristics of the fender has been simplified by a spring-damper model and the friction force is computed in an iterative process within the implicit computation of the wave-body interaction. However, the main disadvantage of CFD methods is the heavy effort regarding modelling and computation.

In comparison to expensive CFD tools, boundary element methods which solve the problem in the time domain instead of the frequency domain provide a reasonable alternative. The consumption of CPU and the computational time is relatively moderate and these methods become more and more practicable due to the increasing computational power. The majority of boundary element methods in the time domain for solving three-dimensional problems uses Rankine panels. In contrast to boundary element methods in the frequency domain, as already mentioned before, Rankine panel methods allow the fully non-linear description of the hydrodynamic wave-body interaction considering the dominating hydrodynamic effects. Further advantages are the good practicality and good overall accuracy, as listed in Table 1.1.

Several time domain approaches have been developed which are directed to seakeeping problems. In this context, Söding and Bertram (2009) presented a method for the simulation of ship motions ins waves based on a patch method. In contrast to panel methods, the boundary conditions are not fulfilled at collocation points but averaged over the patch. Within the numerical method the steady wave problem is considered as non-linear problem whilst for the consideration of the incoming wave field a linear formulation is used. Another boundary element method for the simulation of non-linear ship motion and the structural response in waves was published by Y. Kim et al. (2011) and K.-H. Kim and Y. Kim (2011). In this approach, a B-spline Rankine panel method

is used and a weak-scatterer formulation for the free surface boundary conditions at the water surface is conducted.

A well-known numerical approach to solve the non-linear problem at the free water surface is the Mixed-Eulerian-Lagrangian (MEL) method. It has been introduced by Longuet-Higgins and Cokelet (1976) for two-dimensional waves. O. M. Faltinsen (1977) also presented an MEL method for the investigation of the two-dimensional, non-linear free surface outside and inside of oscillating bodies. After extending the method for axis-symmetric problems by Dommermuth and D. K. Yue (1987), it has also been successfully further developed for three dimensional problems by Isaacson (1982). Cao, Schultz, et al. (1991a,b) combined the MEL approach with a desingularized boundary integral equation method (DBIEM) and simulated the flow field due to an underwater disturbance. The MEL method combined with DBIEM has further be used by Celebi and M. Kim (1997) and M. Kim et al. (1998) to simulate forces on a truncated cylinder in a numerical wave tank (NWT). In addition to this, Ferrant (1999) and Ferrant et al. (2003) published numerical results of a cylinder in regular and irregular waves using an MEL approach. Zhang et al. (2010a,b) published simulation results of the radiation and diffraction forces during seakeeping with forward speed and, more recently, Cao and Beck (2016) published results investigating water sloshing in a tank applying the MEL approach in association with the DBIEM.

Computational simulations of seakeeping problems in the time domain often face numerical instabilities, in particular, if violent body motions occur. One major aspect concerning the numerical stability, consists in the accurate computation of the hydrodynamic pressure. The calculation of the time derivatives within the Bernoulli equation by a time-difference scheme often does not deliver the necessary precision. Therefore, in several BEM in the time domain the velocity potential itself as well as the so-called acceleration potential for the computation of the time derivative are applied. According to the review of Bandyk and Beck (2011), it not only increases the numerical accuracy and stability but also improves the efficiency of the computation. Söding (2019, 2020), for example, used the acceleration potential for the simulation of the non-linear wave response of ships based on a patch method. Here, the kinematic and dynamic boundary condition at the free surface is described in the semi-Lagrangian formulation in which the free surface deformation is only allowed in the vertical direction. Otherwise, the grid points on the free surface shift relative to each other during the simulation, thus, a remeshing would be necessary to ensure the quality of the grid.

Table 1.1.: Computational methodology for time-domain approaches according to the final report and recommendation of the seakeeping committee to the 26th ITTC in *Proceedings of the 26th International Towing Tank Conference* (2011).

Numerical Method	Advantage	Disadvantage	CPU capacity and time
Impulse-Response-Function approach	• Easy to implement • Fast computation • Requires small computer memory	• Needs pre-computed hydrodynamics coefficients • Limited applicability	Minimal
Strip/sectional-based approach	• 2D BVP • Fast computation • require small computer memory	• Limitation as 2D sectional method • Poor accuracy in low frequency	Minimal
Transient wave Green function approach	• Radiation condition is automatically satisfied • Panel distribution on only body surface	• Hard to compute Green function for non-zero speed • Limited application	Moderate
Rankine panel method	• Good practicality • Easy extension to non-linear analysis • Good overall accuracy	• Difficulty in 3D geometric modelling and panel generation • Needs a numerical method for radiation condition	Moderate
CFD method solving field equation(s)	• Capability for violent ship motion • Can include viscous effects	• Huge computational time and effort • Poor accuracy in memory flow	Heavy
Hybrid method combining two methods	• Takes advantages of combined method	• No benefits in many combinations • Additional effort for combinations	(Varying)

1.2. Contribution of Present Work and Thesis Outline

The objective of the present work is the development of an efficient numerical method for the simulation of boat-landing maneuvers. Therefore, an approach based on a boundary element method in the time domain is applied which solves the fluid problem under consideration of the non-linear free water surface. In addition, a simplified fender model is integrated into the simulation method to efficiently solve the contact problem between bow fender and boat-landing structure. Besides the reaction forces due to the deformation of the fender, the model is also able to describe the friction forces in the tangential direction of the contact plane. Here, the model distinguishes between static and kinematic friction and, therefore, it can detect whether the fender slips or not during the landing maneuver.

The approach followed is based on the low-order boundary-element method *pan*MARE (**pan**el Code for **Ma**ritime Applications and **Re**search) which originally was developed for propeller flow simulations in the time domain, see Bauer and Abdel-Maksoud (2012). In *pan*MARE the potential flow is assumed to be a superposition of an pre-defined 'background' flow and the disturbance induced by a body. In the context of this work, the simulation method is extended by introducing a free-surface model to make it suitable for treating wave-body interaction problems. Thus, the approach developed is able to compute the hydrodynamic excitation loads from the prevailing seastate on the catamaran hull considering the diffraction and radiation effects of catamaran and monopile structure. Thereby, the model also considers the hydrodynamic interaction between waves, the monopile and the catamaran which plays a major role concerning the boat motions during the landing maneuvers.

The implemented free-surface model is based on the mixed-Eulerian-Langrangian approach which is well-known and discussed in many scientific papers. In the present approach, the kinematic and dynamic boundary conditions at the free surface are described in the semi-Lagrangian formulation in which the free surface deformation is only allowed in the vertical direction. The advantage of this formulation is that remeshing can be avoided. Otherwise, this would be necessary in order to ensure the quality of the grid as the grid points will be shifted relative to each other during the simulation. In addition to this, the quantities in the two boundary conditions are separated into external and induced parts, following the superposition of the potential flow followed in *pan*MARE.

Regarding the boat-landing maneuver, in addition to the development of the numerical method, experimental investigations are also conducted within the scope of the present work. First, the hydrodynamic influence of the monopile on the wave field for regular waves is analyzed. An innovative method is employed to measure the wave elevation in the circumstance of the monopile. Then, trials regarding the boat-landing maneuver are carried out testing two different catamaran models in regular as well as in irregular waves. Here, the motion of the catamaran models and the forces at the fender are recorded.

The experiments give more insight in the physics in particular the hydrodynamic effects during the landing maneuver and provide relevant data for validation of the numerical method.

Within this thesis, the developed free-surface model is validated by comparing simulation results with other numerical methods. First, the wave making resistance of a spheroid and the induced free surface waves are computed. Furthermore, the simulation of a cylinder in waves and the motion of a Wigley hull in waves are investigated. Then the ability of the method to simulate boat-landing maneuvers and to predict the dangerous slip situation are proven by validation on basis of the experimental results.

The thesis is structured as follows: Chapter 2 summarizes the main theory and governing equations related to the simulation of boat-landing maneuvers and the developed simulation method. First, the chapter introduces the coordinate system, denotes the general notations and definitions. Then the mathematical description of the potential flow field and the boundary value problem are presented. The following sections respectively deal with the description of the hydrodynamic wave-body interaction and the mechanics associated with the contact between fender and boat-landing structure.

Chapter 3 is devoted to the numerical approach. In this context, the boundary-element method *pan*MARE is briefly explained, followed by a description on how the MEL approach for solving the non-linear free surface problem is implemented into the BEM. In this context, the integration of the time-depending quantities is described and the treatment of the numerical instabilities associated with time domain simulations of the free water surface are discussed. Furthermore, the solving routine of the acceleration potential in relation with the free motion model of *pan*MARE is explained.

Chapter 4 presents the experimental investigations regarding the boat-landing maneuver. It begins with the analysis of the wave diffraction due to a monopile foundation in regular waves. After that the motion of a catamaran is experimentally tested during a boat-landing maneuver in regular and irregular waves.

In Chapter 5 simulation results computed by the developed method are shown and discussed. First, the free surface model is validated by comparing the results with published data of other numerical methods. Here, the resistance and the forces due to external waves are computed for submerged bodies as well as for a Wigley hull considering the diffraction and radiation. Furthermore, the non-linear wave forces on a truncated cylinder in regular waves are validated.

Finally, in Chapter 6 the discussed results are summarized, conclusions are drawn and proposals for future work are given.

2. Theoretical Background

This chapter deals with the governing mathematical equations behind the numerical method for the simulation of boat landing maneuvers. Among others, this includes the equations to describe the free surface flow. After defining the coordinate systems and introducing further definitions, the potential flow field related to the Laplace equation is derived from the conservation equations. Based on this, the boundary value problem is defined for the free surface problem, which includes the interaction between waves and body. Furthermore, the mathematical description of the hydrodynamic forces and the approach of the acceleration potential that is related to the equation of motion are discussed. The end of this chapter addresses the contact mechanics between fender and the boat landing structure. Here, the focus lies on the friction model.

2.1. Definitions and Coordinate Systems

Three different Cartesian coordinate systems (COS) are defined for the description of the free surface and the associated wave-body interaction problem. First, a stationary coordinate system (ξ, η, ζ) is assumed. The origin is located on the undisturbed water surface, which is spanned by the ξ- and η-axis. The ζ-axis points against the direction of the gravitation g. Second, a body fixed coordinate system (x, y, z) of which the origin is denoted at the center of gravity. The third coordinate system is an intermediate system $\left(\bar{\xi}, \bar{\eta}, \bar{\zeta}\right)$ that follows the horizontal motion of a body with forward speed but does not participate to heave, roll and pitch motion. The position of a body fixed point with respect to global coordinate system $\xi = (\xi, \eta, \zeta)^T$ is given by

$$\xi = \xi_b + \mathbf{S}\,\mathbf{x}, \tag{2.1}$$

where $\mathbf{x} = (x, y, z)^T$ is the position referred to body-fixed coordinates. Following Figure **??**, the vector $\xi_b = (\xi_b, \eta_b, \zeta_b)^T$ denotes the position of the origin of the body fixed coordinate system and the matrix $\mathbf{S}$ describes the rotation of the body-fixed COS with respect to the stationary coordinate system.

Under the assumption that the point $\mathbf{x}$ is fixed in the body-frame and with $\mathbf{r} = \mathbf{S}\,\mathbf{x}$ being the local position vector related to the global coordinate system, the velocity and the acceleration, with respect to the global COS become:

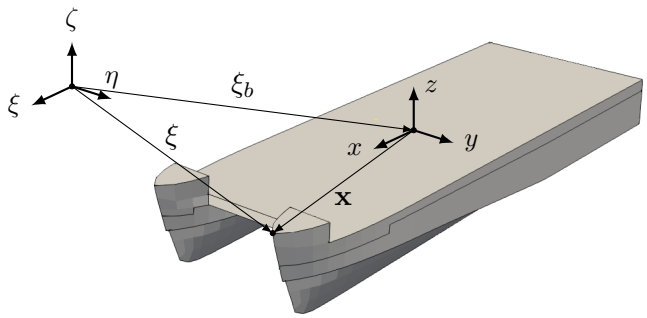

Figure 2.1.: Definition of the coordinate systems for the wave-body interaction problem.

$$\frac{\mathrm{d}\xi}{\mathrm{d}t} = \mathbf{u}_b = \dot{\xi}_b + \omega \times \mathbf{r}\,, \tag{2.2}$$

$$\frac{\mathrm{d}\mathbf{u}_b}{\mathrm{d}t} = \ddot{\xi}_b + \omega \times (\omega \times \mathbf{r}) + \dot{\omega} \times \mathbf{r}\,. \tag{2.3}$$

Here, $\dot{\xi}_b$, $\ddot{\xi}_b$ are the translational velocity and acceleration of the origin of the body fixed coordinate system, and, ω and $\dot{\omega}$ are the rotational velocity and acceleration of any location in the body with respect to the body-fixed coordinate system, respectively.

2.2. Description of the Potential Flow Field

The velocity of a fluid particle can be described by the vector $\mathbf{v} = (v_\xi, v_\eta, v_\zeta)^T$. Further, the flow field can be derived using the equations for the conservation of mass and impulse, which are generally called Navier-Stokes equations. Following Ferziger et al. (2002), the fluid can be assumed incompressible if the Mach number M_a, which represents the ratio between the absolute fluid velocity $|\mathbf{v}|$ and the speed of sound, is small ($M_a < 0.3$). Then, the density ρ can be defined to be constant and the equation for the mass conservation becomes:

$$\nabla \cdot \mathbf{v} = 0\,, \tag{2.4}$$

where $\nabla = (\partial/\partial\xi, \partial/\partial\eta, \partial/\partial\zeta)^T$ is the Nabla operator. The Navier-Stokes equations can be reduced to the Euler equations by neglecting the viscosity. Here, the mass continuity Eq. (2.4) remains the same and the impulse conservation can be written as:

$$\rho\left(\frac{\partial \mathbf{v}}{\partial t} + (\nabla \cdot \mathbf{v})\,\mathbf{v}\right) + \nabla p = \mathbf{f}\,, \tag{2.5}$$

with p being the pressure and $\mathbf{f}$ being an external force. If the flow is assumed furthermore irrotational, then, there exists a potential function Φ for which following equation is valid:

$$\mathbf{v} = \nabla\Phi\,. \tag{2.6}$$

Then, from substituting Eq. (2.6) into the continuity Eq. (2.4), the Laplace equation follows:

$$\Delta\Phi = \nabla^2\Phi = 0\,, \tag{2.7}$$

where Δ is known as the Laplace Operator. The pressure p in the flow can be derived by the integration of the impulse conservation Eq. (2.5) with respect to the spatial coordinates and describing the velocities in terms of the potential Φ. Including the external force due to the gravity acceleration g results in the well-known Bernoulli equation:

$$p + \rho\left(\frac{\partial\Phi}{\partial t} + \frac{1}{2}\,\nabla\Phi^2 + g\zeta\,.\right) = \text{const.} \tag{2.8}$$

with $\partial/\partial t$ denoting the partial time derivative.

2.3. Boundary Value Problem

Figure 2.2 gives an overview of the fluid domain and the boundaries. According to this, a fluid volume $\mathcal{V}$ is assumed which is bounded by the surfaces S_b of arbitrary solid bodies, by the seabed S_{sb} and by S_{fs} at the free surface. Furthermore, the volume has imaginary boundary walls S_∞ in infinity. The geometry of the domain and its boundaries are described with respect to the global coordinate system (ξ, η, ζ). Here, the velocity field in the fluid domain can be defined by a potential function $\Phi(\xi, t)$, which is depending on the position ξ and the time t . The boundaries do not necessarily have to be stationary. Instead, they may have a motion velocity, which does not have to be constant over the whole surface, so that also rotations of a body can be considered.

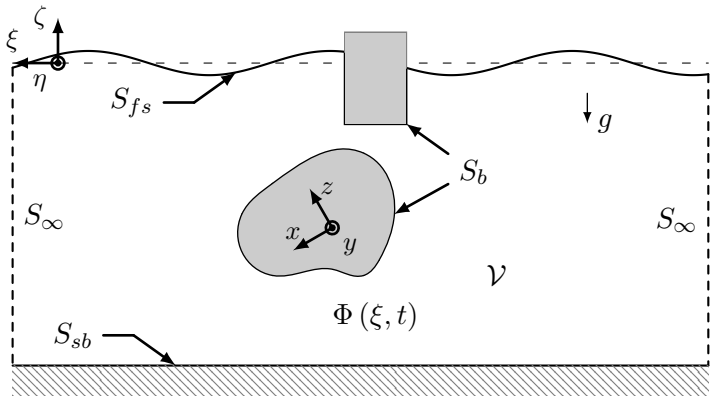

Figure 2.2.: Definition of the fluid domain $\mathcal{V}$ and the coordinate system.

Following the general assumptions for potential flows, the fluid is inviscous, incompressible and irrotational, so that the velocity potential of the fluid $\Phi(\xi,\, t)$ meets Laplace's Eq. (2.7) and, thus:

$$\Delta\Phi\left(\xi, t\right) = 0 \qquad \text{for} \quad \xi \in \mathcal{V}\,, \tag{2.9}$$

The Laplace equation itself does not directly depend on the time t. This means that the time dependency must be introduced by the boundary conditions. Due to the linearity of Laplace's Eq. (2.9), the velocity potential can be superposed from an arbitrary number of basic solutions. In the present work, the velocity potential Φ is primarily subdivided into an external part ϕ_e, which may include a given background flow or the potential of incoming waves, and an induced potential ϕ_i that describes the hydrodynamic effect of a floating or submerged bodies on the fluid velocity:

$$\Phi = \phi_\mathrm{e} + \phi_\mathrm{i}\,. \tag{2.10}$$

The application of Green's second identity leads to the equation for the evaluation of the induced potential ϕ_i at the position ξ in the fluid domain $\mathcal{V}$:

$$0 = \phi_\mathrm{i}\left(\xi\right) - \frac{1}{4\pi}\int\limits_S \left(\phi_\mathrm{i}\left(\xi_r\right)\, G_n\left(\xi, \xi_r\right) - \frac{\partial}{\partial n}\phi_\mathrm{i}\left(\xi_r\right)\, G\left(\xi, \xi_r\right)\right) \mathrm{d}S\,, \qquad \xi \in \mathcal{V}\,, \tag{2.11}$$

where $G(\xi, \xi_r) \equiv 1/|\xi - \xi_r|$ is the source Green function and $G_n(\xi, \xi_r)$ its directional derivative. Substituting the velocity potentials by sources and doublets, where the source strength is denoted as $\sigma = \partial\phi_\mathrm{i}/\partial n$ and the doublet strength as $\mu = -\phi_\mathrm{i}$, the induced potential in the fluid domain can be determined as follows:

$$\phi_\mathrm{i}(\xi) = \frac{1}{4\pi} \int_S \left(\mu \frac{\partial}{\partial n} \frac{1}{r} - \sigma \frac{1}{r} \right) \mathrm{d}S \,, \tag{2.12}$$

with $r = |\xi - \xi_r|$ denoting the distance between the evaluated position ξ and ξ_r which denotes the position of the collocation point of the respective source and doublet on the surface S. This solution satisfies the Laplace Eq. (2.9). Boundary conditions have to be defined to solve Eq. (2.12) in order to determine the potential ϕ_i and the induced velocities $\nabla\phi_\mathrm{i}$. These boundary conditions are discussed in the following.

Boundary Conditions

The potential function is linear, therefore, it can be superposed by an arbitrary number of functions, see Eq. (2.10). Furthermore, different types of boundary conditions can be combined. According to Figure 2.2, three different types of boundary have to be considered in this case. First, the solid boundaries at the body surfaces and the sea bottom, second, the boundary at the free water surface and last the far field boundary at infinity. At the two former types of boundary, the Dirichlet boundary condition ensures that the induced potential is spatially constant outside of the simulation domain, thus:

$$\phi_\mathrm{i}(\xi) = 0 \,, \qquad \text{for} \quad \xi \notin \mathcal{V}. \tag{2.13}$$

Beside of this, at the latter boundary the far field condition has to be matched, so that the induced potential has to vanish towards infinity, thus:

$$\lim_{\xi \to \infty} \nabla\phi_\mathrm{i} = 0 \,. \tag{2.14}$$

Last condition is satisfied by the formulation of the Green function and the induced potential in Eq. (2.12). Further boundary conditions at the solid hull and the free water surface are introduced in the following.

Solid boundaries

On the solid surfaces of body and seabed, the Neumann boundary condition that there is no flow through the surface has to be valid, thus:

$$(\nabla\Phi - \mathbf{u}) \cdot \mathbf{n} = 0 \qquad \text{on} \quad S \in [S_b, S_{sb}]\,. \tag{2.15}$$

Here, $\mathbf{u}$ is the motion velocity at the position ξ and $\mathbf{n}$ the normal vector of the surface, both denoted with respect to the global coordinate system. Input Eq. (2.10) into Eq. (2.15) yields:

$$\nabla\phi_\mathrm{i}\,\mathbf{n} = (\mathbf{u} - \nabla\phi_\mathrm{e}) \cdot \mathbf{n}\,. \tag{2.16}$$

Free water surface boundary

The deformation of the free surface is described by the elevation ζ_fs, which denotes the vertical displacement from the mean water level. In the same way as the potential, the elevation of the free surface is separated into two parts:

$$\zeta_\mathrm{fs} = \zeta_\mathrm{e} + \zeta_\mathrm{i}\,, \tag{2.17}$$

where ζ_e is the external elevation that, for example, may arise from incoming waves and ζ_i that is the elevation due to the disturbance of a body.

At the elevation $\zeta = \zeta_\mathrm{fs}\,(\xi, t)$, two additional equations, the kinematic and dynamic boundary condition, have to be satisfied beside of the Dirichlet boundary condition in Eq. (2.13). In this work, both conditions are formulated in the semi-Lagrangian form. This means, that the values are given with respect to a point on the surface that moves with the same horizontal velocity $\mathbf{u}_{fs} = (u_{fs}, v_{fs}, 0)^T$ as the simulation domain and that is only allowed to displace relatively to the domain coordinate system in the vertical direction. The two boundary conditions are defined as follows:

1. The kinematic boundary condition ensures that the free surface follows the fluid velocity, thus:

$$\frac{\partial\zeta_\mathrm{fs}}{\partial t} = \frac{\partial\Phi}{\partial\zeta} - \nabla\Phi\nabla\zeta_\mathrm{fs}\,. \tag{2.18}$$

Including Eqs. (2.10) - (2.17) into Eq. (2.18) the kinematic boundary condition can be rewritten:

$$\frac{\partial(\zeta_\mathrm{i}+\zeta_\mathrm{e})}{\partial t} = \frac{\partial\phi_\mathrm{i}}{\partial\zeta} + \frac{\partial\phi_\mathrm{e}}{\partial\zeta} \; - (\nabla\phi_\mathrm{i}+\nabla\phi_\mathrm{e})\;(\nabla\zeta_\mathrm{i}+\nabla\zeta_\mathrm{e})\;. \tag{2.19}$$

2. The dynamic boundary condition for a point on the free surface can be derived from Bernoulli's Eq. (2.8). Assuming that the pressure p is equal to the atmospheric pressure p_0 and considering again Eqs. (2.10) - (2.17), the dynamic boundary condition is:

$$\frac{\partial(\phi_\mathrm{i}+\phi_\mathrm{e})}{\partial t} = -g\;(\zeta_\mathrm{i}+\zeta_\mathrm{e}) - \frac{1}{2}\,(\nabla\phi_\mathrm{i}+\nabla\phi_\mathrm{e})^2\;. \tag{2.20}$$

In contrast to Laplace's Eq. (2.9), the kinematic and dynamic boundary conditions are non-linear. Therefore, they have to be meet at the instantaneous free surface position.

2.4. Wave-Body Interactions

The following section deals with the theory to describe the interaction between waves and floating or submerged bodies. This theory is mainly based on the boundary value problem and the velocity potential, which have been introduced in the previous Section 2.3. In the first part, the implementation of the waves into the boundary value problem is explained and then different wave theories and their mathematical description are introduced. After this, the computation of hydrodynamic forces is explained. In association to this, the definition of the acceleration potential is presented. At the end of this section, the equation of the free motion model are derived.

2.4.1. Mathematical Description of Waves

In the present work, waves are considered as external potential ϕ_e that are included in Eq. (2.10) taking advantage of the linearity of the Laplace Eq. (2.9). The potential is given as an analytic formulation. Based on this the fluid velocities $\nabla\phi_\mathrm{e}$ caused by the waves and the respective free surface elevation ζ_e can be computed. Defining the time derivative

$$\mathrm{d}/\mathrm{d}t \equiv \partial/\partial t + \mathbf{u}\cdot\nabla\,, \tag{2.21}$$

and under the term that there are no other external influences than from waves, thus:

$$\phi_\mathrm{e} = \phi_w\,, \tag{2.22}$$

the kinematic and dynamic boundary conditions in Eqs. (2.19) – (2.20) can be rewritten as follows:

$$\frac{\mathrm{d}(\zeta_\mathrm{i}+\zeta_w)}{\mathrm{d}t} = \frac{\partial\phi_\mathrm{i}}{\partial\zeta} + \frac{\partial\phi_w}{\partial\zeta} \; - (\nabla\phi_\mathrm{i} + \nabla\phi_w - \mathbf{u}) \; (\nabla\zeta_w + \nabla\zeta_w) \; , \tag{2.23}$$

$$\frac{\mathrm{d}(\phi_\mathrm{i}+\phi_w)}{\mathrm{d}t} = -g \; (\zeta_\mathrm{i}+\zeta_w) - \frac{1}{2}\left(\nabla\phi_\mathrm{i} + \nabla\phi_w\right)^2 + \mathbf{u} \; (\nabla\phi_\mathrm{i} + \nabla\phi_w) \; . \tag{2.24}$$

Furthermore, assuming that the wave itself satisfies the kinematic and dynamic boundary condition:

$$\frac{\mathrm{d}\zeta_w}{\mathrm{d}t} = \frac{\partial\phi_w}{\partial\zeta} - (\nabla\phi_w - \mathbf{u})\,\nabla\zeta_w \, , \tag{2.25}$$

$$\frac{\mathrm{d}\phi_w}{\mathrm{d}t} = -g\,\zeta_w - \frac{1}{2}\nabla\phi_w^2 + \mathbf{u}\cdot\nabla\phi_w \, , \tag{2.26}$$

the boundary conditions at the free surface in Eqs. (2.19) – (2.20) can be simplified. Accordingly, input Eq. (2.25) into the kinematic boundary condition in Eq. (2.19) yields:

$$\frac{\mathrm{d}\zeta_\mathrm{i}}{\mathrm{d}t} = \frac{\partial\phi_\mathrm{i}}{\partial\zeta} - \nabla\phi_\mathrm{i}\,(\nabla\zeta_\mathrm{i} + \nabla\zeta_w) - (\nabla\phi_w - \mathbf{u}) \; \nabla\zeta_\mathrm{i} \, , \tag{2.27}$$

and from including Eq. (2.26) into the dynamic boundary condition in Eq. (2.20) further follows:

$$\frac{\mathrm{d}\phi_\mathrm{i}}{\mathrm{d}t} = -g\,\zeta_\mathrm{i} - \frac{1}{2}\nabla\phi_\mathrm{i}^2 - (\nabla\phi_\mathrm{i}\,\nabla\phi_w) + \mathbf{u}\cdot\nabla\phi_\mathrm{i} \, . \tag{2.28}$$

In the following, different wave definitions are described and their formulation is given. First, linear wave theory, including equation for Airy waves, the diffraction of a cylinder and irregular waves, is discussed and after that the non-linear Stokes theory is introduced.

Airy Wave Theory

In general, regular waves are defined relating to their length λ_w, their height H_w and the water depth d, see also Fig. 2.3. Under the assumption that the wave height H_w is small relative to the wavelength λ_w, linear wave theory, also called Airy wave theory, can be applied. According to Clauss et al. (2014), in deep water, where $d > 3/(2\pi)\,\lambda_w$, the wave height H_w should not be greater than $2\,\pi\cdot 10^{-3}\,\lambda_w$.

Then, the kinematic and dynamic boundary conditions of the free surface can be linearized, e.g. see Mei (1989). Furthermore, both conditions can be combined and evaluated at the mean water level. Because of the linearized free surface boundary condition,

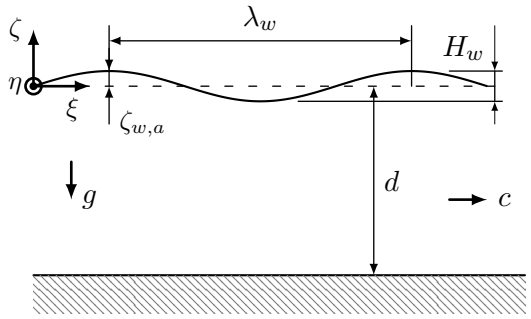

Figure 2.3.: Sketch of linear Airy waves from side view.

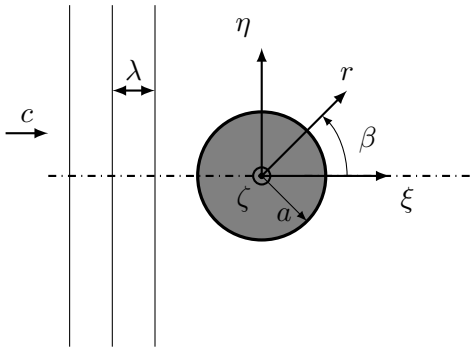

Figure 2.4.: Sketch of cylinder in waves from top view.

the dispersion equation can be derived. It gives the relationship between the wave number k and angular frequency ω of the wave as follows:

$$\omega = \sqrt{k\, g \tanh\left(k\, d\right)}\,, \tag{2.29}$$

Apart of this, a linear solution for the potential of an incident wave can be formulated for a certain position $\xi = (\xi, \eta, \zeta)^T$ and time t in a complex representation. Defining i to be the imaginary number and Re to denote the real part of the complex number, the velocity potential of the linear wave is:

$$\phi_w(\xi, t) = -i\hat{\zeta}_a \frac{\omega}{k} \frac{\cosh\left(k\left(\zeta + d\right)\right)}{\sinh\left(k\, d\right)} \mathrm{Re}\left\langle e^{i\left(-\omega t + k\,\bar{\xi}\right)} \right\rangle\,, \tag{2.30}$$

where $\hat{\zeta}_a = 1/2\, H_w \cdot e^{i\varphi}$ is the complex amplitude of the wave. Here, φ defines the phase information and $\bar{\xi}$ denotes the distance of the reference point ξ related to the direction of wave propagation $\xi_{w,p} = (\xi_{w,p}, \eta_{w,p}, 0)^T$. It can be determined by

$$\bar{\xi} = \xi \cdot \frac{\xi_{w,p}}{|\xi_{w,p}|} = \frac{\xi\, \xi_{w,p} + \eta\, \eta_{w,p}}{|\xi_{w,p}|}\,. \tag{2.31}$$

Considering the spatial derivatives of the vector $\bar{\xi}$ from Eq. (2.31), the spatial derivatives of the potential in Eq. (2.30) can be derived. They provide the velocities in the three

dimensions:

$$v_{w,\xi} = \frac{\partial \phi_w}{\partial \xi} = \hat{\zeta}_a\, \omega\, \frac{\xi_{w,p}}{|\xi_{w,p}|} \frac{\cosh\left(k\left(\zeta + d\right)\right)}{\sinh\left(k\, d\right)} \mathrm{Re}\left\langle e^{i\,(-\omega t + k\,\bar{\xi})} \right\rangle\,, \tag{2.32}$$

$$v_{w,\eta} = \frac{\partial \phi_w}{\partial \eta} = \hat{\zeta}_a\, \omega\, \frac{\eta_{w,p}}{|\xi_{w,p}|} \frac{\cosh\left(k\left(\zeta + d\right)\right)}{\sinh\left(k\, d\right)} \mathrm{Re}\left\langle e^{i\,(-\omega t + k\,\bar{\xi})} \right\rangle\,, \tag{2.33}$$

$$v_{w,\zeta} = \frac{\partial \phi_w}{\partial \zeta} = -i\hat{\zeta}_a\, \omega \frac{\sinh\left(k\left(\zeta + d\right)\right)}{\sinh\left(k\, d\right)} \mathrm{Re}\left\langle i\, e^{i\,(-\omega t + k\,\bar{\xi})} \right\rangle\,. \tag{2.34}$$

The time integration of the velocity $v_{w,\zeta}$ further leads to the elevation ζ_w at the respective point $\xi_{\mathrm{fs}} = (\xi_{\mathrm{fs}}, \eta_{\mathrm{fs}}, 0)^T$ on the water surface:

$$\zeta_w\left(\xi_{\mathrm{fs}}, t\right) = \int v_{w,\zeta}\left(\xi_{\mathrm{fs}}, t\right)\, \mathrm{d}t = \hat{\zeta}_w\, \mathrm{Re}\left\langle e^{i\,(-\omega t + k\,\bar{\xi})} \right\rangle. \tag{2.35}$$

Additionally, the linearized dynamic pressure follows from the partial time derivative of the velocity potential ϕ_w:

$$\frac{\partial \phi_w}{\partial t} = -\hat{\zeta}_w \frac{\omega^2}{k} \frac{\cosh\left(k\left(\zeta + d\right)\right)}{\sinh\left(k\, d\right)} \mathrm{Re}\left\langle e^{i\,(-\omega t + k\,\bar{\xi})} \right\rangle. \tag{2.36}$$

Cylinder Diffraction

The presence of solid bodies at or near the free surface leads to wave reflection or diffraction. Reflection effects are important if the wavelength is very short compared to the body dimension. In this work, the focus lies on wavelengths where diffraction effects are dominating. For some simple geometries like vertical cylinder shapes, the diffraction can be described analytically. The problem of the wave diffraction around a cylinder in deep water has been solved by Havelock (1940). Later Mccamy and Fuchs (1954) extended it for finite depths. Here, the velocity potential of the diffraction is defined as ϕ_{cd}, so that the total wave potential becomes:

$$\phi_{w,d} = \phi_w + \phi_{cd}. \tag{2.37}$$

As shown in Figure 2.4, a polar coordinate system is defined for the formulation of the diffraction potential, where r is the distance and β denotes the angle with respect to the center of the cylinder cross section on the water surface. According to Chakrabarti (1987), the potential for the cylinder diffraction at a certain point $\mathbf{r} = (r, \beta, \zeta)^T$ and an instant of time t is:

$$\phi_{cd}(\mathbf{r}, t) = \hat{\zeta}_a \frac{\omega}{k} \frac{\cosh(k(\zeta + d))}{\sinh(k\, d)} \mathrm{Re}\left\langle \sum_{m=0}^{\infty} E_m H_m^{(1)}(k\, r)\, \cos(m\, \beta)\, e^{-i\,\omega t} \right\rangle. \tag{2.38}$$

Here, $H_m^{(1)}$ is the m^{th}-order Hankel function of the first kind. According to Abramowitz and Stegun (1965), it can be derived as follows:

$$H_m^{(1)}(r) = J_m(r) + iY_m(r)\ , \tag{2.39}$$

where J_m and Y_m denote the m^{th}-order Bessel function of the first and second kind, respectively. The factors E_m in Eq. (2.38) follow from the boundary condition that there is no flow through the cylinder surface. Hence, for a cylinder with the radius a the boundary condition is

$$\left.\frac{\partial \phi_{w,d}}{\partial r}\right|_{r_a = a} = 0. \tag{2.40}$$

Therefore, the radial velocity at the cylinder radius $\mathbf{r}_a$ due to the cylinder diffraction $v_{cd,r}(\mathbf{r}_a, t)$ must eliminate the wave velocities $v_{w,\xi}$ $v_{w,\eta}$ from Eqs. (2.32) – (2.33) in radial direction. The radial velocity due to the cylinder diffraction follows from the spatial derivative of the potential in Eq. (2.38), hence:

$$v_{cd,r}(\mathbf{r}_a, t) = i\,\hat{\zeta}_a \omega \frac{\cosh(k(\zeta + d))}{\sinh(k\, d)} \mathrm{Re}\left\langle \sum_{m=0}^{\infty} E_m H_m^{'(1)}(k\, a)\, \cos(m\, \beta)\, e^{-i\,\omega t} \right\rangle, \tag{2.41}$$

According to Chakrabarti (1987), it can be shown, that satisfying this condition leads to the following equation:

$$E_m = n_m\, i^{m+1} \frac{J_m^{'}(k\, a)}{H_m^{(1)'}(k\, a)}, \quad m = 0,\ 1,\ 2, \ldots, \tag{2.42}$$

where $n_0 = 1$ and $n_m = 2$ for $m \geq 1$. Further, $J_m^{'}$ and $H_m^{(1)'}$ are the spatial derivatives with respect to r of the Bessel and Hankel function, respectively. According to the handbook of mathematics (Abramowitz and Stegun 1965), the derivatives can be computed as follows:

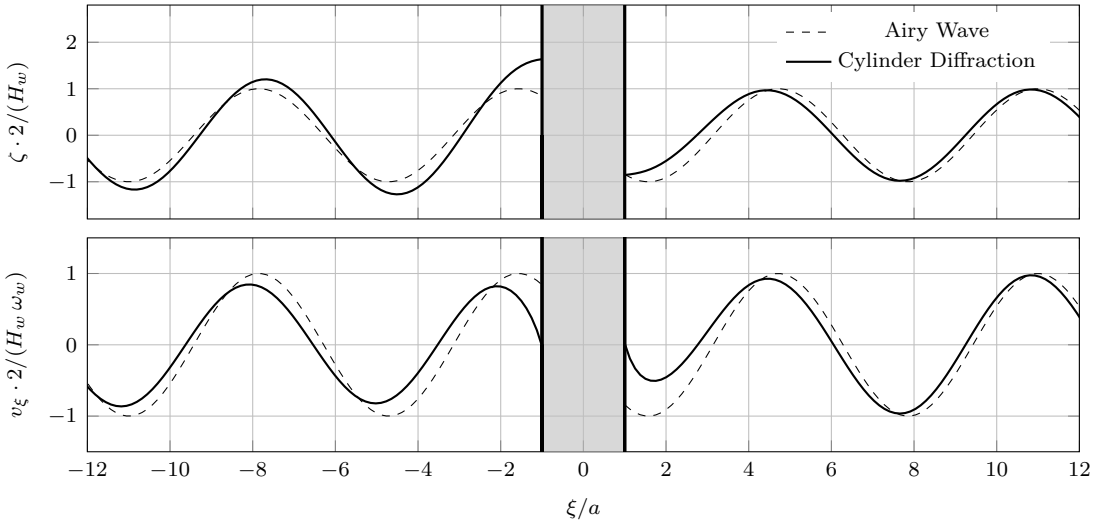

Figure 2.5.: Surface elevation ζ and horizontal fluid velocity v_x near the cylinder according to the cylinder diffraction model in comparison with regular Airy wave for the case $ka = 1$.

$$J'_m(r) = -J_{m+1}(r) + \frac{m}{r} J_m(r) \tag{2.43}$$

$$H_m^{(1)'}(r) = -H_{m+1}^{(1)}(r) + \frac{m}{r} H_m^{(1)}(r) \ . \tag{2.44}$$

In Figure 2.5, the surface elevation ζ (upper plot) and the horizontal fluid velocity v_ξ (lower plot) due to a regular wave travelling in positive ξ-direction are plotted over the distance ξ/a. The center of the cylinder is located at $\xi = 0$ and the non-dimensional wave number is $ka = 1$. The dashed lines show the solution from the Airy wave potential and the solid line denotes the result delivered by the superposition of Airy wave and cylinder diffraction $\phi_{w,d}$. The plot shows that the horizontal velocities at the cylinder surface become zero, thus, the condition that there is no flow through the cylinder is satisfied. The upper plot indicates that the maxima and the minima of the elevation are increased in front of the cylinder ($\xi/a < -1$) whilst in the back they remain almost the same ($\xi/a > 1$).

Irregular Waves

Following Tucker and Pitt (2001), a natural seaway can be represented by a linear superposition of a finite number of regular Airy waves j, which vary regarding their length $\lambda_{w,j}$ or wave frequency ω_j. Assuming that the seaway is not omnidirectional, the

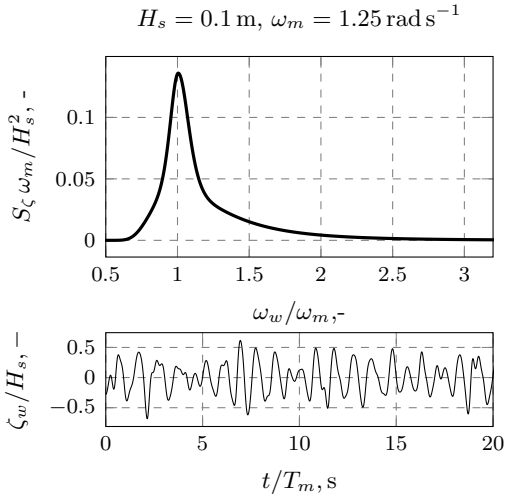

Figure 2.6.: JONSWAP spectrum and an example for the associated wave record.

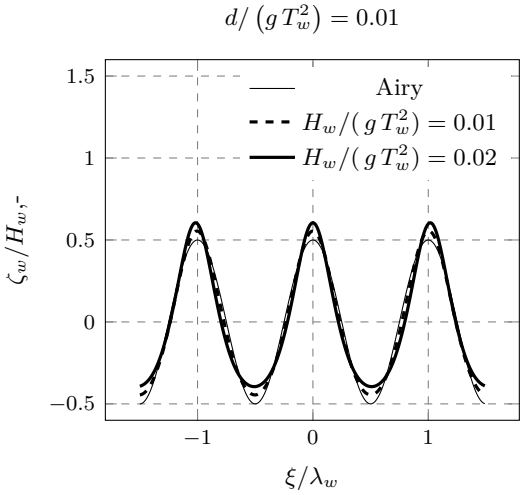

Figure 2.7.: Comparison of wave contour according to linear Airy theory and Stokes Wave.

waves are constrained to one direction $\xi_{w,p}$. This is for example the case, for a wave train generated in a wave tank. Then, the time record of the wave elevation $\zeta_w(t)$ at a fixed position ξ can be subdivided into a number of regular waves:

$$\zeta_w(t) = \sum_j \zeta_{w,j}\,\cos\left(-\omega_j\,t + \varphi_j\right)\,, \tag{2.45}$$

where $\zeta_{w,j}$ and φ_j are the amplitude and the phase information of the wave j, respectively.

The wave energy over the averaged time is depending on the amplitudes $\zeta_{w,j}$ of the respective waves j. Denoting the energy in the wave train as E_w, it can be written:

$$E_w = \rho\,g\,\overline{\zeta_w^2(t)} = \rho\,g\,\sum_j \frac{1}{2}\,\zeta_{w,j}^2\,. \tag{2.46}$$

Assuming that the energy in the seaway or in a wave train is distributed over different wave frequencies, an energy density function $S_\zeta\left(\omega\right)$ can be defined:

$$S_\zeta\left(\omega\right) = \frac{1}{2}\,\frac{\zeta_{w,j}^2}{\Delta\omega_j}\,. \tag{2.47}$$

Here, $\Delta\omega$ denotes the range between the frequencies. Generally, S_ζ is also denoted as wave energy density spectrum. In literature, there exist some commonly used formulae for the description of a realistic wave spectrum, for example the *Pierson-Moskowitz* spectrum or *Bretschneider* spectrum. In this work, the JONSWAP spectrum is used. It has been derived within the *Joint North Sea Wave Observation Projekt* (JONSWAP) as a result from extensive measurements in the North Sea, see K. Hasselmann et al. (1973). There exist several formulations for the JONSWAP spectrum. In the present work, the formulation proposed by Lewandowski (2004) is used:

$$S_\zeta = \alpha \, \frac{g^2}{\omega^5} \cdot \exp\left[-\frac{5}{4}\left(\frac{\omega_m}{\omega}\right)^4\right] \cdot \gamma^r \,, \tag{2.48}$$

with

$$r = \exp\left[-\frac{(\omega-\omega_m)}{\sqrt{2}\,\sigma\,\omega_m}\right]^2 , \qquad \text{and} \qquad \sigma = \begin{cases} 0.07\,, & \text{if} \quad \omega \le \omega_m, \\ 0.09\,, & \text{else.} \end{cases}$$

Here, ω_m is the modal frequency, which denotes the angular frequency at which the energy density reaches its maximum. The peak enhancement factor is γ. This factor may vary from 1 to 7, in the literature it is often assumed to be equal to 3.3, see e.g. Lewandowski (2004). Actually, the parameter α is a function of the mean wind speed measured at a height of 10m and the fetch of the wind, although, following (Lewandowski 2004), the parameter can be also approximated from the modal frequency ω_m and the significant wave height H_s:

$$\alpha \approx \frac{5}{16} \cdot \frac{H_s^2\,\omega_m^4}{g^2 \cdot (1+\eta)} \,, \qquad \text{with} \qquad \eta \approx \frac{1}{6}\,(\gamma - 1) \,. \tag{2.49}$$

The upper plot in Figure 2.6 shows a JONSWAP spectrum with a significant wave height $H_s = 0.1\,\mathrm{m}$ and a modal frequency $\omega_m = 1.25\,\mathrm{rad\,s^{-1}}$. The non-dimensional energy density S_ζ is plotted against the wave frequencies ω, which are divided by the modal frequency ω_m. Below the spectrum an exemplary wave record is shown, where the non-dimensional wave elevation ζ_w/H_w is plotted versus the non-dimensional time t/T_m, with T_m being the modal period. As the energy density spectrum does not contain any phase information of the included waves, the appearance of the resulting wave record varies depending on the distribution of the phases.

Nonlinear Waves

Linear wave theory is the simplest approximation of water waves. According to Clauss et al. (2014), in deep water linear wave theory is only valid up to a steepness $H_w/\lambda_w < 2\pi \cdot 10^{-3}$. For higher waves, non-linear wave theory should be applied, for example based on Stokes Theory, which can be derived from the non-linear boundary conditions in Eqs. (2.19) – (2.20). The theory is limited with respect to small water depths d, see

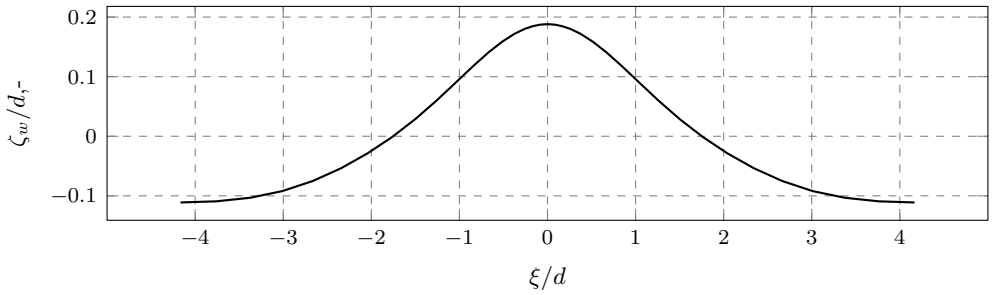

Figure 2.8.: Contour of 5th-order Stokes wave ($\lambda_w/d = 8.333$)

for example Hedges (1995), but shallow water effects are not in the focus of this work. Here, the equation published by Fenton (1985) for the 5th-order Stokes wave is used. Following this, the potential at the position ξ and at the time t can be written as:

$$\phi_{w,nl}(\xi,t) = -\,\bar{u}\,\bar{\xi} + C_0\sqrt{\frac{g}{k^3}} \cdot \sum_{i=1}^{5}\left(\frac{1}{2}\,kH_w\right)^i \sum_{j=1}^{i} A_{ij}\cosh\left(j\,k\,(\zeta+d)\right)\,\sin\left(j\,k\left(\bar{\xi}-c\,t\right)+\epsilon\right)\,. \tag{2.50}$$

where c is the wave celerity and ϵ defines the phase information. Furthermore, C_0 and A_{ij} are dimensionless coefficients which only depends on the non-dimensional water depth kd, $\bar{\xi}$ defines the position with respect to the wave direction $\xi_{w,p}$ and $\bar{u}$ denotes a mean horizontal fluid speed.

In Figure 2.7, the wave elevation per wave height is plotted against the non-dimensional position ξ/λ_w considering a finite water depth $d = 1 \cdot 10^{-2}\left(gT_w^2\right)$. The thick black lines follow the elevation computed by the 5th-order Stokes wave. Here, the dashed line represents a wave with a height $H_w/(g\,T_w^2) = 0.01$ and the solid line shows a wave with the double height. Both are compared with the contour of an Airy wave, which is shown by the thin curve. The contours demonstrate the known characteristic that the greater the wave height the steeper and narrower become the wave crests computed by 5th-order Stokes theory, and, in contrast to this, the wave troughs become flatter.

Furthermore, Figure 2.8 shows the wave contour for a 5th-order Stokes wave with the non-dimensional height $H_w/d = 0.3$ and the non-dimensional length $\lambda_w/d = 8.333$. Following Hedges (1995), the latter value is the maximum limit for application of the Stokes theory. Below this, in Figure 2.9 the wave velocity, acceleration and the time derivative of the wave potential are respectively plotted over the vertical profile from the sea bed at $\zeta/d = -1$ up to the actual surface elevation for three different phases.

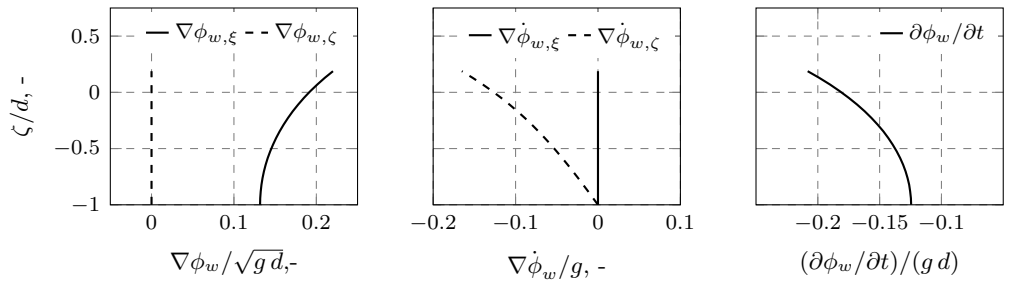

(a) Phase $\varphi = 2\,\pi$

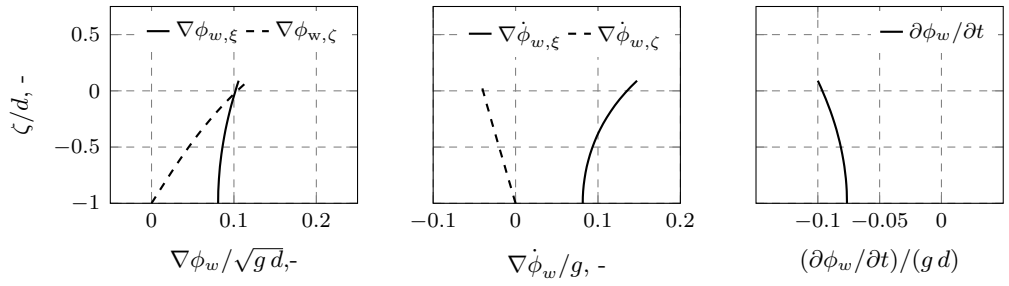

(b) Phase $\varphi = \frac{\pi}{4}$

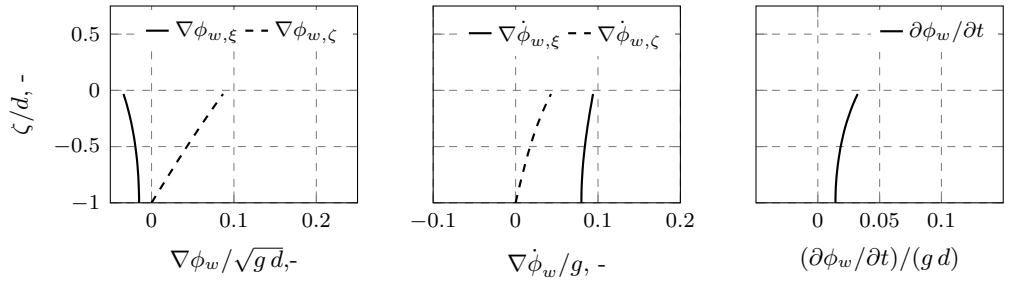

(c) Phase $\varphi = \frac{\pi}{2}$

Figure 2.9.: Vertical profiles of the wave velocity $\nabla\phi_w$, acceleration $\nabla\dot{\phi}_w$ and the time derivative of the potential $\partial\phi_w/\partial t$ for three different phases φ for a 5th-order Stokes wave ($\lambda_w/d = 8.333$) following Fenton (1985).

2.4.2. Hydrodynamic Forces

Beside of the hydrostatic part, the pressure in the fluid depends on the velocity field of the fluid $\nabla\Phi$ and the time variation of the velocity potential Φ. The pressure on a solid surface can be derived from Bernoulli's Eq. (2.51):

$$p = \rho \left(-g\,\zeta - \frac{1}{2}\nabla\Phi^2 - \frac{\partial\Phi}{\partial t} \right) + p_0\,, \tag{2.51}$$

with p_0 being the atmospheric pressure. The respective body experiences a hydrodynamic forces and moments which result from the hydrodynamic pressure distribution over the surface. These can be determined by the spatial integration of the pressure p over the body surface S, thus:

$$\mathbf{f} = \int_S p\,\mathbf{n}\,\mathrm{d}S\,, \tag{2.52}$$

$$\mathbf{m} = \int_S p\,(\mathbf{r}\times\mathbf{n})\,\mathrm{d}S\,. \tag{2.53}$$

The accuracy of the calculated pressure p and of the resulting force $\mathbf{f}$ and moment $\mathbf{m}$ strongly depend on the quality of the time derivative $\partial\Phi/\partial t$ computation. Here, the part from the external potential $\partial\phi_\mathrm{e}/\partial t$ can be derived by the time derivation of the analytic solution. The induced part $\partial\phi_\mathrm{i}/\partial t$ may be computed using a time difference scheme but such an approximation often is not accurate enough, in particular, when it is applied in association with time integration of the equation of motion to solve free motion problem like this is the case in the present work. A much more accurate solution of the time derivative $\partial\Phi/\partial t$ can be achieved by the definition of an acceleration potential as an supplementary boundary value problem. This latter approach will be discussed in the following.

2.4.3. Acceleration Potential

The present theory is partly based on the work by Sichermann (2008) in which the acceleration potential is derived for a two-dimensional domain. In this work, the theory is expanded to three dimensions. A similar method is published by Söding 2020 who presented a three-dimensional boundary element method for the simulation of seakeeping

problems. Here, an acceleration potential χ in the same fluid domain as described in Section 2.3 is assumed. It also satisfies the Laplace Eq. (2.9) and is defined as follows:

$$\chi = \frac{\partial \phi_\mathrm{i}}{\partial t} + \mathbf{u}\,\nabla\phi_\mathrm{i}\,. \tag{2.54}$$

Hence, the acceleration potential χ can be superposed using partial solutions χ_m. In this work, the first term χ_0 is independent of the body accelerations $\dot{\mathbf{u}}_b$ and $\dot{\omega}_b$ whilst each of the $m \in [1,6]$ further potentials is associated with the acceleration in one of the six degrees of motion, thus, the potential can be defined as follows:

$$\chi = \chi_0 + \sum_{m=1}^{6} \chi_m \ddot{\xi}_{u,m}\,, \tag{2.55}$$

where $\ddot{\xi}_{u,j}$ denotes the unit-acceleration in the respective motion direction. According to this, the induced velocities $\nabla\phi_\mathrm{i}$ have to be known before solving the acceleration potential. Although, the boundaries remain the same, other boundary conditions are applied for solving the respective acceleration potentials. The boundary conditions are discussed in the following.

Boundary Conditions

First, Dirichlet and Neumann boundary conditions are employed at the body surfaces and the seabed. The Dirichlet condition is derived using the time derivative of Eq. (2.13). Hence, the acceleration potentials from Eq. (2.55) have to fulfill the following condition at the solid boundaries:

$$\chi_m\left(\xi\right) = 0\,, \qquad \text{for} \quad m \in [1,6]\,,\ \xi \notin \mathcal{V}. \tag{2.56}$$

Furthermore, the Neumann condition further has to be considered at the solid boundaries of the body and the sea bed S_b and S_{sb}. Then, the following condition can achieved from the time derivative of the boundary condition in Eq. (2.15):

$$0 = \left(\frac{\mathrm{d}\nabla\Phi}{\mathrm{d}t} - \frac{\mathrm{d}\mathbf{u}}{\mathrm{d}t}\right)\cdot\mathbf{n} + \left(\nabla\Phi - \mathbf{u}\right)\cdot\frac{\mathrm{d}\mathbf{n}}{\mathrm{d}t}\,, \qquad \text{on} \quad S \in \{S_b, S_{sb}\}\,. \tag{2.57}$$

Here, $\mathbf{u}$ and $\mathbf{n}$ are the velocity and the normal vector of the panel, respectively. Considering the definition of the time derivative in Eq. (2.21), the derivative of the potential may be rewritten:

$$\frac{\mathrm{d}\nabla\Phi}{\mathrm{d}t} = \nabla\frac{\partial\Phi}{\partial t} + (\nabla\nabla\Phi)\,\mathbf{u}\,. \tag{2.58}$$

Then, including this time derivative into the Neumann boundary condition in Eq. (2.57) delivers:

$$0 = \left(\nabla\frac{\partial\Phi}{\partial t} + (\nabla\nabla\Phi)\,\mathbf{u} - \frac{\mathrm{d}\mathbf{u}}{\mathrm{d}t}\right)\cdot\mathbf{n} + (\nabla\Phi - \mathbf{u})\cdot\frac{\mathrm{d}\mathbf{n}}{\mathrm{d}t}\,. \tag{2.59}$$

Taking into account the decomposition of the potential Φ in Eq. (2.10) and the definition of the acceleration potential χ in Eq. (2.54), the Neumann condition for the solid boundaries becomes:

$$\nabla\chi\cdot\mathbf{n} = -\left(\nabla\frac{\partial\phi_\mathrm{e}}{\partial t} + (\nabla\nabla\phi_\mathrm{e})\,\mathbf{u}\right)\cdot\mathbf{n} + (\mathbf{u} - \nabla\phi_\mathrm{i} - \nabla\phi_\mathrm{e})\cdot\frac{\mathrm{d}\mathbf{n}}{\mathrm{d}t} + \frac{\mathrm{d}\mathbf{u}}{\mathrm{d}t}\cdot\mathbf{n}\,. \tag{2.60}$$

According to the subdivision of the acceleration potential in Eq. (2.55), the Neumann boundary condition is also subdivided into six terms which include the body accelerations and one remaining part which is independent of the body accelerations. Following Sichermann (2008), the Neumann condition for the six acceleration potentials χ_m can be described as follows:

$$\nabla\chi_m\,\mathbf{n} = \tilde{\mathbf{n}}\,, \qquad \text{for} \quad m\in[1,6]\,, \tag{2.61}$$

where

$$\tilde{\mathbf{n}} = \left(\mathbf{n}^T, (\mathbf{r}\times\mathbf{n})^T\right)^T\,. \tag{2.62}$$

The vector $\mathbf{r}$ denotes the surface position related to the center of rotation in global coordinates. Subdividing the acceleration parts χ_m under consideration of Eq. (2.3) from the boundary condition Eq. (2.60), the remaining part represents the Neumann boundary condition for χ_0:

$$\nabla\chi_0\,\mathbf{n} = -\nabla\frac{\partial\phi_\mathrm{e}}{\partial t}\,\mathbf{n} - \mathbf{n}\;(\nabla\nabla\phi_\mathrm{e})\,\mathbf{u} + (\mathbf{u} - \nabla\phi_\mathrm{i} - \nabla\phi_\mathrm{e})\cdot\frac{\mathrm{d}\mathbf{n}}{\mathrm{d}t} + (\omega\times(\omega\times\mathbf{r}))\,\mathbf{n}\,. \tag{2.63}$$

At the free water surface, the Dirichlet boundary condition in Eq. (2.56) has to be satisfied for the acceleration potentials $\chi_1, \ldots, \chi_6$ as well. In contrast to this, the boundary condition for the acceleration potential χ_0 is given by the dynamic boundary condition of the free water surface. Therefore, it is:

$$\chi_0 = \frac{\partial \phi_\mathrm{i}}{\partial t} + \mathbf{u}_\mathrm{fs} \nabla \phi_\mathrm{i} \,, \tag{2.64}$$

with $\mathbf{u}_\mathrm{fs}$ being the velocity vector of the free surface. Apart from this, also the far field condition can be derived from the time derivative of the equivalent condition of the velocity potential in Eq. (2.14). This means, the condition is:

$$\lim_{\xi \to \infty} \nabla \chi = 0 \,. \tag{2.65}$$

2.4.4. Equation of Motion

The free motion of a solid body which is floating or submerged in a fluid, in six degrees of freedom can be described by Newton's law. Hence, the equation of the translation motion $\mathbf{u}_b$ and of the rotational motion ω_b with respect to the center of gravity of the body can be written as:

$$\mathbf{f} = \frac{\mathrm{d}}{\mathrm{d}t} \left(m_b \, \mathbf{u}_b \right) \,, \tag{2.66}$$

$$\mathbf{m} = \frac{\mathrm{d}}{\mathrm{d}t} \left(\mathbf{J}_b \, \omega_b \right) \,. \tag{2.67}$$

Here, m_b is the mass of the body and $\mathbf{J}_b$ is the 3×3 matrix of the local mass moment of inertia. Both are assumed to be constant over the time. The rate of change of the angular momentum in Eq. (2.67) can be written as:

$$\frac{\mathrm{d}}{\mathrm{d}t} \left(\mathbf{J}_b \, \omega_b \right) = \mathbf{J}_b \, \dot{\omega}_b + \omega_b \times \left(\mathbf{J}_b \cdot \omega_b \right) \,. \tag{2.68}$$

Describing the motion with respect to the stationary frame in global coordinates, the equation of motions can be written as follows:

$$\mathbf{I}_b \begin{pmatrix} \dot{\mathbf{u}}_b \\ \dot{\omega}_b \end{pmatrix} = \begin{pmatrix} \mathbf{f} \\ \mathbf{m} - \omega_b \times \left(\mathbf{J}_b \cdot \omega_b \right) \end{pmatrix} \,, \quad \text{with} \quad \mathbf{I}_b = \begin{pmatrix} m_b \mathbf{E} & 0 \\ 0 & \mathbf{J}_b \end{pmatrix} \,, \tag{2.69}$$

where $\dot{\mathbf{u}}_b$ is the translatory acceleration vector and ω_b, $\dot{\omega}_b$ are the rotational velocity and acceleration of the body, respectively. Furthermore, $\mathbf{E}$ denotes the unit matrix. Hence, knowing the force and moment acting on the body and its rotational velocity ω_b the equation system can be solved for the accelerations. The time integration then delivers the velocities and the displacement.

Following Söding (2004), a major problem concerning the time integration of the equation of motion consists in the so-called added mass terms. These terms represent the parts of the hydrodynamic forces which are depending on the body accelerations that are still unknown for the actual time step. In order to overcome this problem, the added mass terms are separated from the hydrodynamic forces:

$$\begin{pmatrix} \mathbf{f} \\ \mathbf{m} \end{pmatrix} = \begin{pmatrix} \bar{\mathbf{f}} \\ \bar{\mathbf{m}} \end{pmatrix} - \mathbf{a} \begin{pmatrix} \dot{\mathbf{u}}_b \\ \dot{\omega}_b \end{pmatrix} , \tag{2.70}$$

where $\mathbf{a}$ defines the added mass matrix and $\bar{\mathbf{f}}$, $\bar{\mathbf{m}}$ respectively denote the force and moment which are independent of the body acceleration.

The coefficients for the 6×6 added mass matrix $\mathbf{a}$ of the body can be derived from the integration of the acceleration potentials χ_1, χ_2, …, χ_6 over the respective body surface S_b, thus:

$$a_{mn} = \rho \int_{S_b} \chi_m \, \tilde{n}_n \, \mathrm{d}S_b \qquad \text{for} \quad m,\, n \in [1, 6] \, . \tag{2.71}$$

Here, $\tilde{n}_n$ are the coefficients of the vector defined in Eq. (2.62). Considering Eq. (2.70), the equation of motion can be rewritten:

$$(\mathbf{I}_b + \mathbf{a}) \begin{pmatrix} \dot{\mathbf{u}}_b \\ \dot{\omega}_b \end{pmatrix} = \begin{pmatrix} \bar{\mathbf{f}} \\ \bar{\mathbf{m}} - \omega_b \times (\mathbf{J}_b \cdot \omega_b) \end{pmatrix} . \tag{2.72}$$

The force $\bar{\mathbf{f}}$ and the moment $\bar{\mathbf{m}}$ can be directly computed replacing the pressure p taken from Eq. (2.51) by an acceleration-independent pressure $\bar{p}$ for the computation of the hydrodynamic loads in Eqs. (2.52) – (2.53). The pressure $\bar{p}$ can be determined taking into account the definition of the acceleration potential χ_0, following Eqs. (2.54) – (2.55), and input it in the Bernoulli Eq. (2.8):

$$\bar{p} = \rho \left(-g\,\zeta - \frac{1}{2} \nabla \Phi^2 - \chi_0 - \mathbf{u} \nabla \phi_\mathrm{i} + \frac{\partial \phi_\mathrm{e}}{\partial t} \right) + p_0 \, . \tag{2.73}$$

The separation of the added mass stabilizes the time integration regarding the free motion of bodies in waves. Another advantage of separating the body acceleration terms, is that the body acceleration itself follows from the forces acting on the body and thus cannot be quantified before the hydrodynamic loads are known.

2.5. Fender Contact Forces

The topic of contact forces is not the focus of the developed method and is therefore not investigated comprehensively. Instead, some assumptions are made to simplify the problem of the interaction between the bow fender and the boat-landing structure in such a way, that the contact forces between vessel and offshore structure can be estimated in an appropriate manner focusing on the aim to predict the motion of the vessel and to forecast dangerous slip occurrences.

In general, fenders are made of high deformable PE-composit material and therefore much more deformable compared to steel constructions used for the monopile and the associated boat-landing structure. Taking this into account, the fender deformation and the resulting forces could be simplified using a linear spring-damper model to approximate the contact forces between monopile structure and moving catamaran. However, it must be kept in mind that contact forces go hand in hand with friction which often plays an important role concerning contact mechanics. Whilst in most engineering problems, the aim is to reduce the friction, for the boat-landing maneuver the friction is not only desirable but essential to reduce the relative motion of the vessel's bow with respect to the boat-landing of the offshore wind structure. Special aspects, which should be considered here, are the fact that the contact surface can be either dry or wet and that the fender not necessarily stays stick at the boat-landing structure but could start to slip.

In the following, the theory behind the fender model is introduced, starting with a brief description of friction. Based on this, the theory behind the simplified fender model, which takes the friction phenomenon into account and is able to distinguish between stick and slip situations, is explained.

2.5.1. Friction

Friction inevitably occurs everywhere where solid surfaces or fluid layers are in contact and are moving relatively to each other. Although, in many cases friction effects are relatively small, thus, they are neglected in many mathematical models, there are a lot of physical issues in which friction plays an important role. Concerning fluid dynamics, friction is for example important for the computation of ship resistance or for the energy losses in pipe flows. Furthermore, the friction is a fundamental issue of a lot of problems

related to contact mechanics, for example of brakes and hinges. Here, the friction characteristic, for example, can have an influence on the durability of the structure or can cause undesired noises. The physics of friction is an extensive research field. Therefore, the following description confines to the basic theory of friction effects which are related to the contact problem between fender and boat-landing structure. This means that certain phenomena like adhesion or capillary effects won't be considered.

Here, a brief description of the basic principles and qualitative friction models based on the book published by Popov (2010) are presented. According to this, the dry friction between two solid bodies follows Coloumb's law of friction. This yields that the frictional force is proportional to the normal force, and it is almost independent from the speed. Furthermore, in first-order approximation it is independent from the size of the contact area. Coloumb's law of friction provides two equations for the static and kinetic friction force f_{sf} and f_{kf}:

$$|f_{\mathrm{sf}}| = \mu_s \cdot |f_n| \ , \tag{2.74}$$

$$|f_{\mathrm{kf}}| = \mu_k \cdot |f_n| \ . \tag{2.75}$$

Here, μ_s, μ_k are called the static and kinetic friction coefficient, respectively. A rough approximation is to set both coefficients equal, but generally it is:

$$\mu_k \leq \mu_s \ . \tag{2.76}$$

According to the Eqs. (2.74) - (2.75), the friction force is proportional to the normal force. This is the case when effects in the contact zone remain of elastic nature and when the surfaces are not lubricated or wet (*dry friction*). Referring to the contact between fender and boat-landing, the respective contact surfaces cannot be assumed to be dry due to rain, waves or sea spray. Instead, in many cases the surfaces are wet, and the water can be seen as lubrication. This decreases not only the friction coefficients but also changes the friction behaviour significantly (*wet friction*). Following Popov (2010), the kinetic friction coefficient for two lubricated surfaces μ_{kl} depends on the sliding velocity v due to the viscous effects in the fluid, thus:

$$\mu_{\mathrm{kl}}(v) = \mu_k + k_v \cdot v \, , \tag{2.77}$$

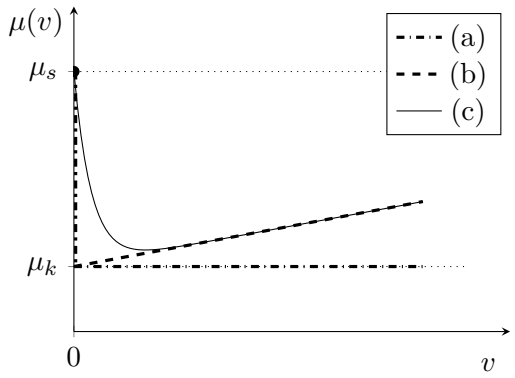

Figure 2.10.: Friction coefficients μ versus the motion velocity v according to different models: (a) Coloumb's law, (b) extended Coloumb's law, (c) Stribeck curve.

where k_v denotes a viscous constant. Due to the fact, that the water film can be assumed to be very thin with respect to the contact area, the roughness of interfacing surfaces still has an important influence, and the surface may not be regarded as fully lubricated by water. According to Popov (2010), this is called *mixed friction* and it can be described by the Stribeck curve:

$$\mu_{\mathrm{km}}(v) = \mu_k + (\mu_s - \mu_k)\, e^{\gamma} + k_v\, v\,. \tag{2.78}$$

with $\gamma = -(v/v_{\mathrm{ref}})^{\delta}$. Here, v_{ref} defines a reference velocity that influences the function minimum and δ denotes a coefficient in the range $\delta \in [0.5, 2.0]$.

In Figure 2.10 the change of the friction due to the motion is shown for three different models. First, description following the law of friction by Coloumb, second, Coloumb's law with an extension using a linear viscous term, and third, according to Stribeck's curve. First approach only delivers two discrete coefficients, one for the static and another for the kinetic case. Furthermore, the extended Coloumb's law adds a dependency of the friction coefficient considering the relative motion v between the contact surfaces. This dependency is also considered in Stribeck's curve but in contrast to the former models, it additionally delivers a continuous solution in the transition range from static to kinematic friction. This is particularly important when it is used in association with numerical methods.

2.5.2. Fender Friction Problem

Assuming a bow fender, which is in contact with the boat-landing or another superstructure, it will experience a pressure force in normal direction of the contact plane. This pressure force varies in dependence of the thrust force of the vessel propulsion system. Apart from this, tangential forces due to friction that in turn depend on the contact

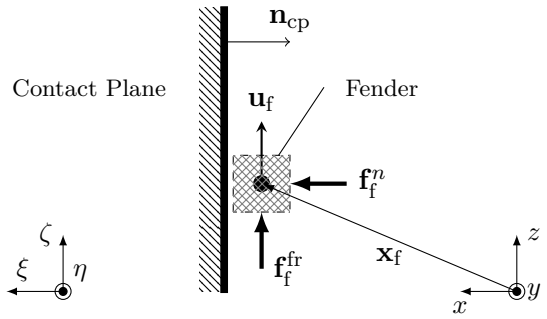

Figure 2.11.: Simplified fender contact model for a vertical contact plane

pressure are acting between fender and boat-landing structure. In Figure 2.11 a fender element at a contact plane which is assumed to be vertical is drawn with definitions related to the simplified fender model. Here, $(\xi, \eta, \zeta)^T$ and $(x, y, z)^T$ are the coordinates of the global and the vessel coordinate system, respectively. The fender position in local coordinates of the vessel is $\mathbf{x}_{\mathrm{f}}$ and its velocity along the contact surface is denoted as $\mathbf{u}_{\mathrm{f}} = (u_{\mathrm{f},\xi}, u_{\mathrm{f},\eta}, u_{\mathrm{f},\zeta})$. First, forces in the normal direction of the vertical contact plane $\mathbf{n}_{\mathrm{cp}} = (n_{\mathrm{cp},\xi}, n_{\mathrm{cp},\eta}, 0)^T$ are acting on the fender of the vessel:

$$\mathbf{f}_{\mathrm{f}}^{n} = f_{\mathrm{f}}^{n}\, \mathbf{n}_{\mathrm{cp}}\,. \tag{2.79}$$

Beside of the force in normal direction, also the friction force $\mathbf{f}_{\mathrm{f}}^{\mathrm{fr}}$, which is acting in tangential direction of the contact plane, has to be considered. According to Section 2.5.1, the relation between the normal and the tangential friction force is given by Coulomb's law of dry friction, see Eqs. (2.74)–(2.75). Concerning the boat-landing maneuver, in particular the friction force in vertical direction $f_{\mathrm{f},\zeta}^{\mathrm{fr}}$ is of interest. The relation for the vertical friction force can be mathematically described according to Eq. (2.76):

$$\left| f_{\mathrm{f},\zeta}^{\mathrm{fr}} \right| \leq \mu_{\mathrm{f}} \|\mathbf{f}_{\mathrm{f}}^{n}\|\,. \tag{2.80}$$

The friction coefficient μ_{f} depends on the properties of the compound of the two surfaces but also on the condition if the fender is moving along the surface or sticks, thus, it is depending on the velocity components tangential to the surface. In the present case, the horizontal parts of the velocity are neglected and only the vertical component $u_{\mathrm{f},\zeta}$ is considered:

$$\mu_{\mathrm{f}}\left(u_{\mathrm{f},\zeta}\right) = \begin{cases} \mu_s, & \text{if } \; u_{\mathrm{f},\zeta} = 0 \\ \mu_{\mathrm{km}} & \text{else.} \end{cases}, \tag{2.81}$$

Here, μ_s is representing the static friction coefficient and μ_{km} is the kinetic friction coefficient following the Stribeck curve in Eq. (2.78). According to the relation in Eq. (2.80), there exists a upper bound for the friction force $f_{\mathrm{f}}^{\mathrm{sl}} = \max(\left|f_{\mathrm{f}}^{\mathrm{fr}}\right|)$ which depends on the magnitude of the normal force $\|\mathbf{f}_{\mathrm{f}}^{n}\|$ and the friction coefficient $\mu_{\mathrm{f}}\left(u_{\mathrm{f},\zeta}\right)$, thus:

$$f_{\mathrm{f}}^{\mathrm{sl}} = \mu_{\mathrm{f}} \left\|\mathbf{f}_{\mathrm{f}}^{n}\right\| . \tag{2.82}$$

Beside of this, the friction force is always a reaction force, thus, it cannot be greater than the force $f_{\mathrm{f}}^{\mathrm{st}}$ that is needed to keep or achieve a stick condition. Otherwise, the friction force would accelerate the fender instead of slowing down its velocity. Hence, for the friction force $f_{\mathrm{f}}^{\mathrm{fr}}$ follows:

$$f_{\mathrm{f}}^{\mathrm{fr}} = \begin{cases} f_{\mathrm{f}}^{\mathrm{sl}}, & \text{if } \; f_{\mathrm{f}}^{\mathrm{st}} \geq f_{\mathrm{f}}^{\mathrm{sl}}, \\ f_{\mathrm{f}}^{\mathrm{st}} & \text{else.} \end{cases} \tag{2.83}$$

For the computation of the required friction force $\mathbf{f}_{\mathrm{f}}^{\mathrm{st}}$, the dynamics of the vessel have to be considered. Assuming that the friction force between the fender and the boat-landing structure is acting for the most part in vertical direction, thus $f_{\mathrm{f},\zeta}^{\mathrm{st}} \gg_{\mathrm{f},\xi}^{\mathrm{st}}$ and $f_{\mathrm{f},\zeta}^{\mathrm{st}} \gg_{\mathrm{f},\eta}^{\mathrm{st}}$, the friction force of the fender for the case that it keeps stick at its current position is simplified to

$$\mathbf{f}_{\mathrm{f}}^{\mathrm{st}} = \left(0,\, 0,\, f_{\mathrm{f},\zeta}^{\mathrm{st}}\right)^{T} .$$

In order to determine the required force to keep the fender in stick position, it is included into the equation of motion as an additional unknown, thus, Eq. (2.72) becomes:

$$\left(\mathbf{I}_b + \mathbf{a}\right) \begin{pmatrix} \dot{\mathbf{u}}_b \\ \dot{\omega}_b \end{pmatrix} - \begin{pmatrix} \mathbf{f}_{\mathrm{f}}^{\mathrm{st}} \\ \mathbf{x}_{\mathrm{f}} \times \mathbf{f}_{\mathrm{f}}^{\mathrm{st}} \end{pmatrix} = \begin{pmatrix} \bar{\mathbf{f}} \\ \bar{\mathbf{m}} - \omega_b \times \left(\mathbf{J}_b \cdot \omega_b\right) \end{pmatrix} + \begin{pmatrix} \mathbf{f}_a \\ \mathbf{m}_a \end{pmatrix} \tag{2.84}$$

The friction forces depend on the dynamics of the body and the other loads, which must be known prior for the determination of the friction force. Therefore, the friction force $\mathbf{f}_{\mathrm{f}}^{\mathrm{st}}$ is included as an additional unknown, beside of the axial and angular accelerations of the body, into the equation of motion. This means that an additional equation is needed, thus, the linear equation system can still be solved. This additional equation is given by the stick - condition. From the kinematic point of view, it means that the time integration of the vertical acceleration of the fender $\dot{u}_{\mathrm{f},\zeta}$ has to cancel out the current fender velocity $u_{\mathrm{f},\zeta}$. The vertical velocity component must become zero, thus:

$$
\begin{aligned}
0 &= u_{\mathrm{f},\zeta} + \int_{t_i}^{t_i+\Delta t} \dot{u}_{\mathrm{f},\zeta}\,\mathrm{d}t\,, \quad \text{with} \\
u_{\mathrm{f},\zeta} &= u_{b,\zeta} + \left(\omega_b \times \mathbf{x}_\mathrm{f}\right)_\zeta\,, \\
\dot{u}_{\mathrm{f},\zeta} &= \dot{u}_{b,\zeta} + \left(\omega_b \times \left(\omega_b \times \mathbf{x}_\mathrm{f}\right)\right)_\zeta + \left(\dot{\omega}_b \times \mathbf{x}_\mathrm{f}\right)_\zeta\,.
\end{aligned}
\tag{2.85}
$$

Moving the known velocities to the right-hand side and the unknown accelerations to the left, leads to the following boundary condition that the fender sticks at the contact surface:

$$
\left(\dot{u}_{b,\zeta} + \left(\dot{\omega}_b \times \mathbf{x}_\mathrm{f}\right)_\zeta\right)\,\Delta t = -u_{b,\zeta} - \left(\omega_b \times \mathbf{x}_\mathrm{f}\right)_\zeta - \left(\omega_b \times \left(\omega_b \times \mathbf{x}_\mathrm{f}\right)\right)_\zeta\,\Delta t\,. \tag{2.86}
$$

Considering this boundary condition, the equation of motion can still be solved as a linear equation system and the required friction force for keeping the fender fixed can be obtained. The calculated value can be compared with the maximum available friction force following Eq. (2.83) to determine the actual friction force and to check if the fender slips or keeps at its position.

3. Numerical Approach

This chapter contains a description of the numerical method for the simulation of the boat-landing maneuver. The numerical method follows the theories which are introduced in the previous Chapter 2. In the first part, the boundary element method *pan*MARE is briefly described focusing on the process of solving the velocity potential. Then, the numerical approach for the computation of the non-linear free surface using the mixed-Eulerian-Lagrangian method is introduced. Here, the time integration of the elevation velocity and the deformation of the free surface grid are explained. Furthermore, the handling of the intersection between free water surface and body grid as well as the treatment of the numerical instabilities which are associated with the free surface are discussed. Finally, in Section 3.4 the numerical model for the contact between fender and boat-landing structure is described.

3.1. Boundary Element Method

The present approach is based on a low-order boundary element method which follows the approach presented by Katz and Plotkin (2001). In this method, the geometrical approximation is first-order discretizing the body and the free surface using panels. These panels are mainly quadrilateral and planar. Each panel is associated with a source and doublet which are defined at the collocation point. The location of the collocation point is set almost at the center of the respective panel with a small shift outwards related to the fluid domain. The influence functions of the panels were firstly derived by Hess and Smith (1962). Further descriptions are given by Newman (1986) and Katz and Plotkin (2001). The description of the panel influence factors used in *pan*MARE are documented in Greve (2015), for example. Here, the singularities have a constant strength over one panel, so that the distribution of the potential over the discretized surface is a zero-order approximation.

Assuming a surface mesh consisting of N panels, the total potential Φ, see Eq. (2.10), can be computed by the sum of all influencing panels j. Considering also Eq. (2.12), leads to

$$\Phi(\xi) = \frac{1}{4\pi} \sum_{j}^{N} \left(\int_{S_j} \mu_j \frac{\partial}{\partial n_j} \frac{1}{r_j} \mathrm{d}S_j - \int_{S_j} \sigma_j \frac{1}{r_j} \mathrm{d}S_j \right) + \phi_\mathrm{e} \,, \tag{3.1}$$

where μ_j and σ_j denote the doublet and the source strength on the panel j, respectively.

Furthermore, following the Dirichlet boundary condition from Eq. (2.13), on the boundaries S the sum of all source and doublet strengths must be zero, hence:

$$0 = \frac{1}{4\pi} \sum_{j}^{N} \left(\int_{S_j} \mu_j \frac{\partial}{\partial n_j} \frac{1}{r_j} \mathrm{d}S_j - \int_{S_j} \sigma_j \frac{1}{r_j} \mathrm{d}S_j \right) , \quad \text{for} \quad \xi \in S \, . \tag{3.2}$$

The mathematical definitions of the influence factors of the panels are described in detail in Greve (2015). Here, they are introduced as matrix coefficients

$$A = \frac{1}{4\pi} \int_{S} \frac{\partial}{\partial n} \frac{1}{r} \, \mathrm{d}S \, , \tag{3.3}$$

$$B = -\frac{1}{4\pi} \int_{S} \frac{1}{r} \, \mathrm{d}S \, . \tag{3.4}$$

Using these coefficients, a linear equation system (LES) can be set up based on Eq. (3.2) considering the panels for the body (subscript b) and the free surface (subscript fs):

$$0 = \sum_{j=1}^{N_b} A_{ij} \mu_{b,j} + B_{ij} \sigma_{b,j} + \sum_{k=N_b+1}^{N_{fs}+N_b} A_{ik} \mu_{\mathrm{fs},k} + B_{ik} \sigma_{\mathrm{fs},k} \ , \tag{3.5}$$

where $\mu_{b,j}$ and $\sigma_{b,j}$ denote the doublet and source strengths on the body panel j whilst $\mu_{\mathrm{fs},k}$ and $\sigma_{\mathrm{fs},k}$ define the strength of the free surface panel k. The source strengths of the body panels are directly derived applying the Neumann condition following Eq. (2.16):

$$(\mathbf{u} - \nabla \phi_{\mathrm{e}}) \cdot \mathbf{n} = \sigma_b \, . \tag{3.6}$$

Assuming a hydrodynamic problem where the influence of the free surface is negligible, thus $\mu_{\mathrm{fs},k} = \sigma_{\mathrm{fs},k} = 0$, the doublet strengths of the body panels $\mu_{b,k}$ are the only unknowns and the equation system in Eq. (3.5) can be directly solved to determine the unknowns and, consequently, the velocity potential of the fluid. Otherwise, the linear equation system is undefined due to the additional unknowns at the free water surface. Nevertheless, the mixed-Eulerian-Lagrangian approach can be used to keep the equation system solvable even under consideration of the free surface problem. This method is discussed in the following section.

3.2. Mixed-Eulerian-Lagrangian Approach

Several known boundary element methods in the time domain use the Mixed-Eulerian–Lagrangian (MEL) or very similar methods to solve the non-linear problem at the water surface. This MEL method has been introduced by Longuet-Higgins and Cokelet (1976) for two-dimensional waves. One year later O. M. Faltinsen (1977) also presented a MEL method for the investigation of the two-dimensional, non-linear free surface outside and inside of oscillating bodies. After extending the method for axis-symmetric problems by Dommermuth and D. K. Yue (1987), it has also been successfully developed further to three dimensions by Isaacson (1982). The Mixed-Eulerian-Lagrangian method has already been applied in combination with a high-order boundary element method to compute the dynamics of steep three-dimensional waves and the fully nonlinear wave-body interaction, see Xue et al. (2001) and Liu et al. (2001), for example.

According to the Mixed-Eulerian-Lagrangian approach, the free surface problem is regarded as an initial value problem $\dot{y} = f(t, y)$, with the initial value $y(t_0) = y_0$. Briefly describing the MEL method to solve the free surface problem, it consists of two consecutive steps:

1. Solving the boundary value problem in the Eulerian frame to compute the induced potential ϕ_i and the induced velocities $\nabla\phi_\mathrm{i}$ at the free water surface,
2. Time integrating the kinematic and dynamic boundary conditions for a Lagrangian point on the free water surface.

At the initial time step $t_0 = 0$, the induced potential $\phi_\mathrm{i}(\xi, t_0)$ and the induced elevation $\zeta_\mathrm{i}(\xi, t_0)$ are assumed to be zero. This means that the doublet strength of the free surface panels $\mu_{b,k}$ are also zero in the first time step and the linear equation system following Eq. (3.5) can be solved to obtain the source strength which yield the induced velocities at the free surface.

The flow chart in Figure 3.1 shows how the computation of free surface is implemented into the general solving routine of the boundary element method *pan*MARE. Knowing the induced potential and the induced velocities at the free water surface for the instant of time t_n from solving the velocity potential, the time derivative of the elevation $\mathrm{d}\zeta_\mathrm{i}/\mathrm{d}t$ can be computed following the kinematic boundary condition in Eq. (2.27) and the time derivative of the induced potential $\mathrm{d}\phi_\mathrm{i}/\mathrm{d}t$ can be determined from the dynamic boundary condition in Eq. (2.28). After this, a fourth-order Runge-Kutta scheme is used to compute the new elevation ζ_i and the induced potential ϕ_i for the next time step $t_{n+1} = t_n + \Delta t$. The induced potential further delivers the doublet strength μ_{fs} at the free surface for the linear equation system, see Eq. (3.5).

Concerning the simulation of waves, from the physical point of view the most realistic approach is to introduce the waves using an inlet boundary condition that works similarly to a wave maker. However, in the present approach the waves are included by using the

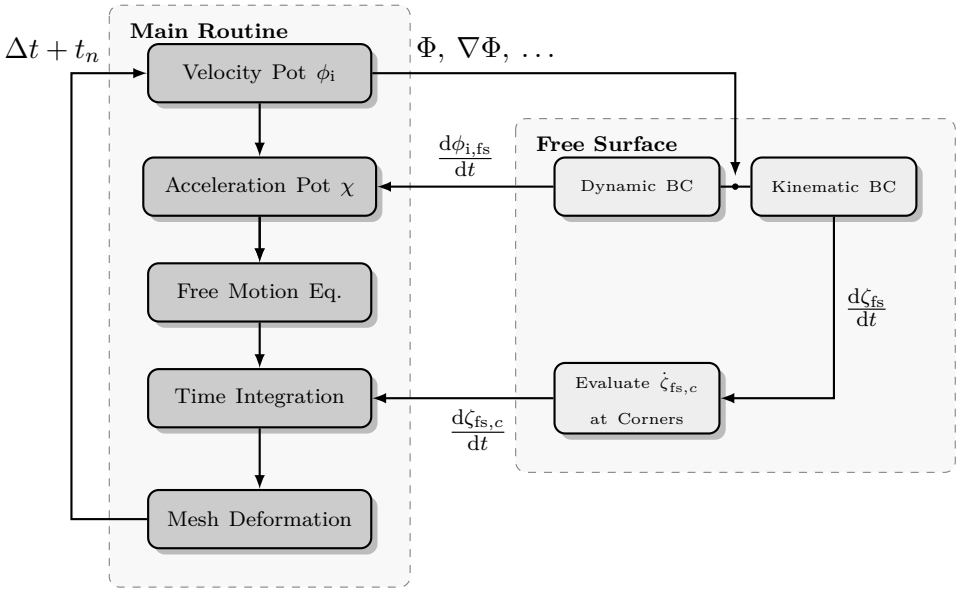

Figure 3.1.: Flow chart of the *pan*MARE solving routine and the interaction with the free surface model.

external potential ϕ_e, see Section 2.4.1, taking advantage of the linearity of Laplace's Eq. (2.9). In this meaning, also the free surface elevation is superposed by the wave elevation ζ_w and the induced elevation ζ_i, see Eq. (2.17). Here, it has to be mentioned that the boundary conditions at the free water surface are non-linear and therefore they have to be met at the instantaneous free surface position ζ_fs which may be outside the definition range of the external wave potential. Therefore, the respective values are expanded to the free surface position using a zero-order approximation which leads to acceptable results. Nevertheless, a higher-order approximation should be considered for future work. Söding (2020) employed a first-order Taylor expansion to evaluate the kinematic values of the wave at the actual free surface position, for example.

3.2.1. Time Integration and Displacement of Free Surface

The kinematic and dynamic boundary condition in Eqs. (2.27) – (2.28) deliver the time derivatives of the induced potential $\dot{\phi}_\mathrm{i} = \mathrm{d}\phi_i/\mathrm{d}t$ and the induced elevation $\dot{\zeta}_\mathrm{i} = \mathrm{d}\zeta_i/\mathrm{d}t$ on the free surface, respectively. The time integration of these derivatives is done using a fourth-order Runge-Kutta method. In accordance with this method, within one time step of the time integration, the boundary value problem is solved four times. In the following, the integration of the time derivatives is described by means of the elevation velocity $\dot{\zeta}_\mathrm{i}$. The time integration for the induced potential is treated in the same way.

Assuming a new time step to be $t_{m+1} = t_m + \Delta t$, the elevation can be computed as follows:

$$\zeta_{\mathrm{i},m+1} = \zeta_{\mathrm{i},\,m} + h \sum_{j=1}^{4} b_j \, k_j \tag{3.7}$$

where h refers to the time step between two successive points and b_j are coefficients taken from the so-called Butcher-tableau

$$b = \left[\frac{1}{6}, \, \frac{1}{3}, \, \frac{1}{3}, \, \frac{1}{6} \right] .$$

Further, k_j are intermediate solutions of the time integration of the elevation velocity. Assuming the elevation velocity to be a function depending on the time and the elevation, thus $\dot{\zeta}_\mathrm{i}\,(t_n,\, \zeta_{\mathrm{i},n})$, the coefficients become:

$$\begin{aligned}
k_1 &= \dot{\zeta}_\mathrm{i}\,(t_n,\, \zeta_{\mathrm{i},n})\,, & k_2 &= \dot{\zeta}_\mathrm{i}\left(t_n + \frac{1}{2}\,h,\, \zeta_{\mathrm{i},n} + \frac{1}{2}\,h\,k_1\right), \\
k_3 &= \dot{\zeta}_\mathrm{i}\left(t_n + \frac{1}{2}\,h,\, \zeta_{\mathrm{i},n} + \frac{1}{2}\,h\,k_2\right), & k_4 &= \dot{\zeta}_\mathrm{i}\,(t_n + h,\, \zeta_{\mathrm{i},n} + h\,k_3)\,.
\end{aligned}$$

According to Eq. (3.7), at the end of all four Runge-Kutta steps of the time integration, the induced elevation for the new time step $n+1$ can be determined as follows:

$$\zeta_{\mathrm{i},n+1} = \zeta_{\mathrm{i},n} + h\,\Delta\zeta_{\mathrm{i},n}\,, \qquad \text{with} \tag{3.8}$$

$$\Delta\zeta_{\mathrm{i},n} = \frac{1}{6}\,\left(k_1 + 2\,k_2 + 2\,k_3 + k_4\right)\,. \tag{3.9}$$

In every time step, the free surface mesh is updated by displacing the corners of the panels regarding the actual elevation ζ_fs, see Eq. (2.17). Whilst the external elevation ζ_e and its time derivative are defined at every position on the surface by the solution of the underlying potential, the change of the induced elevation $\Delta\zeta_\mathrm{i}$ and the resulting displacement according to Eqs. (3.8) – (3.9) are only known at the collocation point c of the respective panel. Therefore, the elevation velocity is transferred from the collocation point near the panel center to the respective panel corners p, see Fig. 3.2. Thus, the displacement at the panel corners $\Delta\zeta_\mathrm{fs}^\mathrm{p}$ is computed using a linear interpolation from the adjacent panels, as follows:

$$\Delta\zeta_\mathrm{fs}^\mathrm{p} = \frac{1}{n}\sum_{j=1}^{n}\left(\Delta\zeta_{\mathrm{i},j}^\mathrm{c} + \nabla\zeta_{\mathrm{i},j}^\mathrm{c}\,\tilde{\mathbf{x}}\right) + \Delta\zeta_\mathrm{e}^\mathrm{p}\,. \tag{3.10}$$

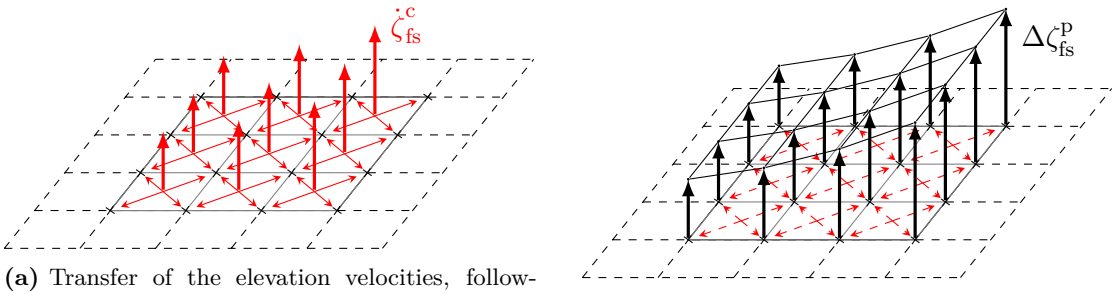

(a) Transfer of the elevation velocities, following the kinematic boundary condition, to the panel corners.

(b) Deformation of the grid by displacing the free surface panel corners, according to $\Delta\zeta^{p}_{fs}$.

Figure 3.2.: Evaluation of elevation velocity of the free surface panels for displacing the mesh of the free water surface.

Here, n is the number of panels, which are attached to the corner p, and $\tilde{\mathbf{x}} = \mathbf{x}^{p} - \mathbf{x}^{c}_{j}$ is the position vector of the corner related to the panel center. Furthermore, $\Delta\zeta^{c}_{i}$ is the induced elevation of the free surface following Eq. (3.9), which is determined at the collocation position, $\nabla\zeta^{c}_{i}$ denotes its spatial derivative in the three dimensions and ζ^{p}_{e} is the external part of the free surface displacement at the respective corner point.

3.2.2. Procedure for Intersection between Free Surface and Body

Concerning wave-body interactions of floating or other surface-piercing bodies, the calculation of the waterline between body and free surface is the most crucial part from the numerical point of view, because this is the location from where the induced waves spread and where the highest wave steepness is expected. Therefore, numerical solutions for hydrodynamic problems associated with surface-piercing bodies often need a special treatment of the waterline. This is particularly true for a low-order boundary element method like the one used in the present work because the solution of the boundary value equations does not directly provide a result for the velocity potential at the waterline. To overcome this problem the following two approaches can be applied to handle the intersection between body and free surface. Exemplary, the different treatments of the intersection are illustrated for the problem of a Wigley hull in waves, see Fig. 3.3.

1. **Direct Connection:** The knots along the waterline are connected to the free surface as well as to the body grid. According to Figure 3.3a, the body grid only describes the underwater part, in this case. However, the entire body surface is defined by frames, along which the intersection knots can slide up- or downwards. The free surface mesh is directly connected to the hull via these knots on each frame. As already mentioned, the knot is allowed to shift only along the curve, furthermore, a sub curve c_{sub} is defined between this knot at the free surface and the lower end point of the frame. Hence, the length of the sub curve in- or

decreases following the motion of the free surface point and the mesh points of the hull grid, which are distributed along the sub curves $c_{sub}(t_c)$ using the control variable $t_c \in [0, 1]$, shift accordingly. The elevation velocity at the waterline is computed by extrapolating the elevation velocity from neighboring panels centers to the intersection points.

2. **Free Surface Cut-out:** Instead of connecting the free surface directly with the body surface, the free surface is cut-out in a way, that a small gap between both panel groups is left. This gap which can be defined by its width d_g, see Fig. 3.4, ensures that the body and free surface panels do not intersect. In contrast to the first method, here, the body surface below and above the water surface is discretized, see Fig. 3.3b. The wetted surface of the hull (dark panels) is described for each time step using a *surface fraction* method which works similarly to the *volume fraction* method which is often used in finite volume methods for the description of multiphase flows. Here, the fraction of fluid at each body panel is determined by extrapolating the position of the free water surface towards the hull surface. If some corners of the panel are above the respective level of the free water surface, the fraction of fluid is computed and the influence of the panel is reduced accordingly, though, if all corners are above the water, the panel is deactivated for the current time step.

The main drawback of the first approach using a direct connection is that the motion direction of the intersection knot is defined by the local inclination of the hull frame, thus, the intersection knot may move also in horizontal direction following the contour of the frame. Then, this would violate the semi-Lagrangian formulation of the kinematic and dynamic boundary condition, which constrains the motion to the vertical direction. The error can be assumed to be small if the contour of the frame is almost vertical at the free surface level but, otherwise, it can be a crucial source for inaccuracies and for numerical instabilities. In comparison to this, the free surface cut-out promises a more stable solution from the numerical point of view. On the other hand, the free space between water surface and body surface results in an inaccuracy which increases the wider the gap is.

3.2.3. Treatment of Numerical Instabilities

There mainly exist two numerical problems associated with the MEL method, first the so-called *saw tooth* instability. This problem is known since the method has been developed and there have been several publications related to overcome it. The other numerical problem consists in undesired reflection from the outer boundaries of the free water surface. In the following, both problems and how they are treated will be discussed.

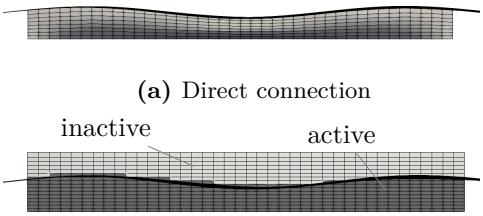

(a) Direct connection

(b) Free surface cut-out

Figure 3.3.: Side view on the mesh of the Wigley model using different treatments of free surface intersection.

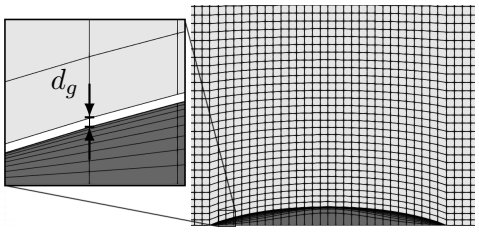

Figure 3.4.: Definition of gap size d_g between hull surface and grid of the free water surface.

Saw tooths

A chessboard pattern from the oscillation of successive points of the panel mesh may arise on the free surface during the simulation using the MEL approach. These oscillations, of which the wavelength is twice the grid spacing, generally grow over the time, lead to numerical errors, and may provoke that the mesh collapses. This numerical instability was firstly encountered by Longuet-Higgins and Cokelet (1976) who simulated two-dimensional water waves. They denoted these instabilities as *saw tooth* problem based on their appearance (for the two-dimensional case). According to Moore (1983), the instability is due to a resonance which is introduced by the discretization. Dommermuth and D. K. Yue (1987) recommend to use a small time step size Δt in order to avoid such *saw tooth* instability. The time step size should meet the following Courant condition:

$$\Delta t^2 \leq \frac{8}{\pi} \frac{\Delta x}{g} , \tag{3.11}$$

where Δx is the grid spacing and g the gravity constant.

Apart from this, the instability can be effectively removed by smoothing schemes which filter the short-wave modes having a length of $\lambda = 2\,\Delta x$ out. Most of the applied smoothing schemes in literature are based on polynomial functions using five or more adjacent and evenly spaced points (see Dold 1992; Sun 2007). For example, Longuet-Higgins and Cokelet (1976) use following five-point formulation:

$$\bar{f}_i = \frac{1}{16} \left(-f_{i-2} + 4\, f_{i-1} + 10\, f_i + 4\, f_{i+1} - f_{i+2} \right) , \tag{3.12}$$

in which f_i and $\bar{f}_i$ denote values of the points i before and after smoothing, respectively. The disadvantage of this formulation is that it is not valid for non-equally spaced points and that it requires neighboring values on both side of the regarded point. This means, that it is not usable for points at or nearby the intersection between body and free surface where the steepest waves generally occur and thereby the probability for numerical errors is high.

In the present work a formulation for non-equally spaced grids is applied which additionally include equations for start or end points (with missing neighbors). It is based on a Chebyshev five points smoothing scheme published by Koo and M.-H. Kim (2004).

Using the implemented scheme, the curve of N successive points i with the position x_i and the local grid spacing $\Delta x_k = x_k - x_i$ is smoothed by the following equations:

$$\bar{f}_i = \begin{cases} a_0, & \text{for } i = 0, \\ a_1, & \text{for } i = 1, \\ a_{N-2}, & \text{for } i = N-2, \\ a_{N-1}, & \text{for } i = N-1, \\ a_i, & \text{else,} \end{cases} \tag{3.13}$$

with

$$\begin{aligned}
a_0 &= \frac{1}{2}\left(\left(\frac{\Delta x_{i+1}^2}{\Delta x_{i+2}^2} + \frac{3}{2}\right) f_i + f_{i+1} - \left(\frac{\Delta x_{i+1}^2}{\Delta x_{i+2}^2} + \frac{1}{2}\right) f_{i+2}\right), \\
a_1 &= \frac{1}{2}\left(-\frac{2\,\Delta x_{i+1}}{\Delta x_{i-1} - \Delta x_{i+1}} f_{i-1} + \left(-\frac{2\,\Delta x_{i-1}\,\Delta x_{i+1} + 3\,\Delta x_{i+1}^2}{\Delta x_{i+2}^2} + 1\right) f_i \right. \\
&\quad \left. + \frac{\Delta x_{i-1} + \Delta x_{i+1}}{\Delta x_{i-1} - \Delta x_{i+1}} f_{i+1} + \frac{2\,\Delta x_{i-1}\,\Delta x_{i+1} + 3\,\Delta x_{i+1}^2}{\Delta x_{i+2}^2} f_{i+2}\right), \\
a_{N-2} &= \frac{1}{2}\left(\frac{2\,\Delta x_{i-1}\,\Delta x_{i+1} + 3\,\Delta x_{i-1}^2}{\Delta x_{i-2}^2} f_{i-2} - \frac{2\,\Delta x_{i-1}}{\Delta x_{i-1} - \Delta x_{i+1}} f_{i-1} \right. \\
&\quad \left. + \left(-\frac{2\,\Delta x_{i-1}\,\Delta x_{i+1} + 3\,\Delta x_{i+1}^2}{\Delta x_{i-2}^2} + 1\right) f_i + \frac{2\,\Delta x_{i-1}}{\Delta x_{i-1} - \Delta x_{i+1}} f_{i+1}\right), \\
a_{N-1} &= \frac{1}{2}\left(\left(\frac{\Delta x_{i-1}^2}{\Delta x_{i-2}^2} + \frac{3}{2}\right) f_i + f_{i-1} - \left(\frac{\Delta x_{i-1}^2}{\Delta x_{i-2}^2} + \frac{1}{2}\right) f_{i-2}\right), \\
a_i &= \frac{1}{2}\left(\frac{-\Delta x_{i-1}\,\Delta x_{i+1}}{\Delta x_{i-2}\,(\Delta x_{i+2} - \Delta x_{i-2})} f_{i-2} + \frac{-\Delta x_{i+1}}{(\Delta x_{i-1} - \Delta x_{i+1})} f_{i-1} \right. \\
&\quad + \frac{\Delta x_{i-1}\,\Delta x_{i+1}}{\Delta x_{i+2}\,(\Delta x_{i+2} - \Delta x_{i-2})} f_{i+2} + \frac{\Delta x_{i-1}}{(\Delta x_{i-1} - \Delta x_{i+1})} f_{i+1} \\
&\quad \left. + \left(\frac{\Delta x_{i-1}\,\Delta x_{i+1}}{\Delta x_{i-2}\,\Delta x_{i+2}} + 1\right) f_i\right).
\end{aligned}$$

In general, for a point on the free water surface the induced elevation ζ_i and the induced potential ϕ_i are smoothed. Here, the smoothed values are obtained by the average of the smoothing along the two horizontal directions. According to Sun (2007), the free surface has only to be smoothed in the near-body region as far away the induced elevations become small and therefore saw tooth instabilities are unlikely.

In Figure 3.5, the effect of the smoothing following Eq. (3.13) is shown. Here, a curve is smoothed which is affected by the *saw tooth* problem. The original curve is an arbitrary polynomial function $f(x)$ with the degree n and the *saw tooth* phenomena is introduced by alternately shifting the points lying on curve $f(x)$. This leads to the mathematical description for the *saw tooth* curve:

$$h(x) = f(x) + (-1)^j \left(b_0 + b_1\, x + \ldots + b_{n-1}\, x^{n-1}\right) , \tag{3.14}$$

where b are polynomial coefficients and $j = 1, 2, 3, \ldots$ is a consecutive counter for the points x_j. Here, the smoothing scheme following Eq. (3.13) (present) is compared with the formulation by Longuet-Higgins and Cokelet (LHC) for two different discretizations. In the upper graph, the points x_j are equally spaced whilst in the lower graph the distance between varies significantly. The original polynomial curve is denoted by the black dashed curves and the gray dash dotted curves denote the result affected by the *saw tooth* problem. Furthermore, the end of the discretized range is marked by the black rule at the right-hand side ($x = 1.0$). First, the comparison demonstrate that the present approach also delivers a smoothed solution for the points without or with less neighboring points at the end of the discretized domain. However, in both graphs a small error between the smoothed and the original curve exists. Concerning the inner points, both formulations deliver the same result if the knots are evenly distributed. Using the present approach this is also true for uneven distributed points whilst the smoothing by the formulation of Longuet-Higgins and Cokelet (1976) indicate an expected error as it is defined only for equally spaced grids.

Reflections

The second numerical instability is induced by the reflections from the borders of the free surface grid. The reflected waves interact with each other, increase with the simulation time, and may cause a significant error of the results. Most of the published works use an artificial damping scheme in which additional terms are added to the kinematic and dynamic boundary condition to get rid of the reflections. An overview on different methods is given by M. W. Kim et al. (2014) who varied the damping scheme for a three-dimensional numerical wave tank.

Following Ferrant et al. (2003), in this work a damping coefficient $\nu_d \in [0, 1]$ is defined and included into the kinematic and dynamic boundary condition in Eqs. (2.27) – (2.28) as follows:

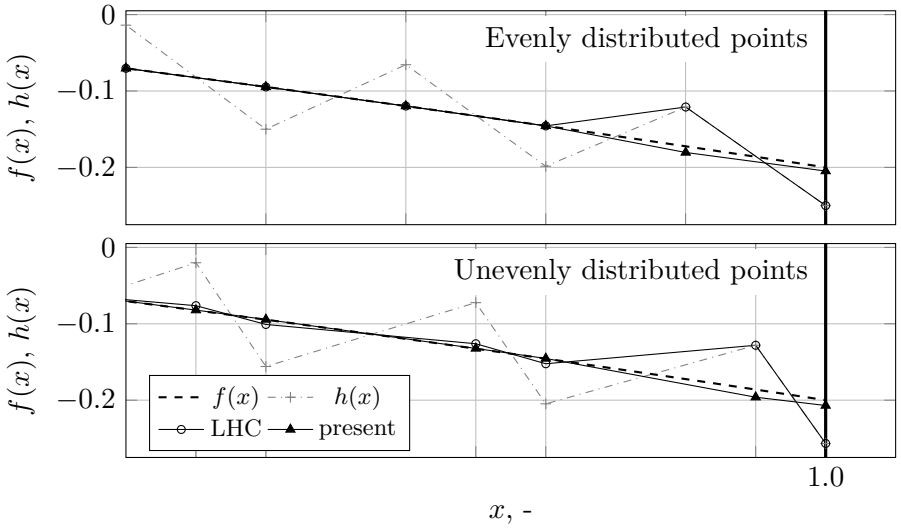

Figure 3.5.: Smoothing of an arbitrary polynomial curve $f(x)$ which is affected by an artificial saw tooth problem comparing the approach by Longuet-Higgins and Cokelet (1976) (LCH) and the present formulation.

$$\left(\frac{\mathrm{d}\zeta_\mathrm{i}}{\mathrm{d}t}\right)_d = \frac{\partial\phi_\mathrm{i}}{\partial\zeta} - \nabla\phi_\mathrm{i}\,\nabla\left(\zeta_\mathrm{i}+\zeta_\mathrm{e}\right) - (\nabla\phi_\mathrm{e}-\mathbf{u})\nabla\zeta_\mathrm{i} - \zeta_\mathrm{i}\,\nu_d\,, \tag{3.15}$$

$$\left(\frac{\mathrm{d}\phi_\mathrm{i}}{\mathrm{d}t}\right)_d = -g\,\zeta_\mathrm{i} - \frac{1}{2}\,\nabla\phi_\mathrm{i}^2 - \nabla\phi_\mathrm{i}\,\nabla\phi_\mathrm{e} + \mathbf{u}\cdot\nabla\phi_\mathrm{i} - \phi_\mathrm{i}\,\nu_d\,. \tag{3.16}$$

The damping coefficient ν_d is defined to be zero near the body which is in the focus of the numerical analysis. At the outer borders of the free surface mesh a damping zone is defined where the coefficients are increased by a ramp based on a $\cos(\xi)$ function. This method works very well for simulations of bodies in waves.

Apart from this, it must be ensured that the panels at the outer border do not remain permanently displaced, e. g. by a stationary wave field, otherwise the surface will start to oscillate. Then low-frequency waves will travel through the whole simulation domain and cause an error. It is presumed that the reason for this is that the domain will not be closed any more if the panels at the outline of the surface are shifted vertically, so that the definition of the potential is not fulfilled.

Therefore, an absorption factor $\nu_a \in [0,1]$ is defined and distributed in the absorption regions near the borders of the free water surface like the scheme for the damping. The aim is to avoid that a stationary wave field arises at one of the outer boundaries of the free surface mesh, which is particularly important when a steady wave is considered as a

resistance problem. Hence, the time derivatives from Eqs. (3.15) – (3.16) are multiplied by a term including the absorption factor ν_a as follows:

$$\left(\frac{\mathrm{d}\zeta_\mathrm{i}}{\mathrm{d}t}\right)_{d,a} = (1-\nu_a)\cdot\left(\frac{\mathrm{d}\zeta_\mathrm{i}}{\mathrm{d}t}\right)_{d}, \tag{3.17}$$

$$\left(\frac{\mathrm{d}\phi_\mathrm{i}}{\mathrm{d}t}\right)_{d,a} = (1-\nu_a)\cdot\left(\frac{\mathrm{d}\phi_\mathrm{i}}{\mathrm{d}t}\right)_{d}. \tag{3.18}$$

3.3. Acceleration Potential and Free Motion

After solving the velocity potential according to the linear equation system in Eq. (3.2), the induced potential ϕ_i and the induced velocities $\nabla\phi_\mathrm{i}$ are known on the body and the free surface. Hence, the acceleration potential χ following Eq. (2.54) can be solved. As the geometrical properties and the panel distribution remain the same, the influence factors A and B from Eqs. (3.3) – (3.4) can be reused and the coefficient matrices applied for the linear equation system in Eq. (3.5) do not have to be recomputed. Following Eq. (2.55), seven linear equation systems are solved to compute the acceleration potentials χ_m, with $m \in [0,6]$. The equation systems for the acceleration potential putting the unknowns on the left hand-side can be written as:

$$\sum_{j=1}^{N_b} A_{ij}\,\chi_{b,mj} + \sum_{k=N_b+1}^{N_\mathrm{fs}+N_b} B_{ik}\,\nabla\chi_{\mathrm{fs},mk} = -\sum_{j=1}^{N_b} B_{ij}\,\nabla\chi_{b,mj} - \sum_{k=N_b+1}^{N_\mathrm{fs}+N_b} A_{ik}\chi_{\mathrm{fs},mk}\,, \tag{3.19}$$

with $m \in [0,6]$.

Within the equation system, the unknowns are the acceleration potential χ_b on the body and the derivative of the potential $\nabla\chi_\mathrm{fs}$ on the free water surface. The values on the right hand in Eq. (3.19) are given by the boundary conditions introduced in Section 2.4.3. Here, for the acceleration potential χ_0 which is independent from the body accelerations, the values $\nabla\chi_{b,0j}$ on the body are defined by Eq. (2.63) and the values $\nabla\chi_{\mathrm{fs},0j}$ follow the dynamic boundary condition, see Eq. (2.64). The boundary conditions for the six further acceleration potentials are listed in Table 3.1.

The latter acceleration potentials $\chi_1, \chi_2, \ldots, \chi_6$ are used for the computation of the added mass matrix $\mathbf{a}$ following Eq. (2.71). According to Section 2.4.4, the added mass matrix $\mathbf{a}$ is used to remove the hydrodynamic forces $\mathbf{f}$ and moments $\mathbf{m}$ from the parts that are depending on the body acceleration. Apart from the hydrodynamic loads also additional forces $\mathbf{f}_a$ and moments $\mathbf{m}_a$, which are not included in the solution of the velocity potential like the propeller thrust or fender forces, may be considered. Extending

Table 3.1.: Boundary conditions on body and free surface for the determination of acceleration potential and its derivative.

m	$\nabla\chi_{b,m}$	$\chi_{\mathrm{fs},m}$
1-2	$\mathbf{n}^T$	0
4-6	$(\mathbf{r}\times\mathbf{n})^T$	0

the equation of motion according to Eq. (2.72) by the additional loads, the accelerations of the body can be solved as follows:

$$\begin{bmatrix}\dot{\mathbf{u}}_b\\ \dot{\omega}_b\end{bmatrix} = [\mathbf{I}_b+\mathbf{a}]^{-1}\begin{bmatrix}\bar{\mathbf{f}}+\mathbf{f}_a\\ \bar{\mathbf{m}}-\omega_b\times(\mathbf{J}_b\cdot\omega_b)+\mathbf{m}_a\end{bmatrix}. \tag{3.20}$$

After solving the equation system, the accelerations are known and the fourth-order Runge-Kutta method that has been introduced in Section 3.2.1 is used for the time integration of the kinematic values in order to obtain the velocity and further the displacement of the body.

3.4. Fender Contact Model

Figure 3.6 shows a sketch of the catamaran that is in contact with the monopile structure during the boat-landing maneuver. Beside of the hydrodynamic part consisting of the interacting effects of incoming waves, the cylinder diffraction and radiation the present method can be applied to determine the contact forces between catamaran and monopile structure, and to compute the resulting motions of the vessel. Here, the fender contact model is closely coupled with the free motion model of *pan*MARE. In the general solution of the boundary element method, after solving the boundary integral equation, the hydrodynamic forces on the body are handed over to the free motion model, which further collects additional forces, which are not provided by the solution of the velocity potential. These forces can be hydrodynamic forces introduced by thrust or the steering system of the ship but also external forces due to wind, for example. Following this,

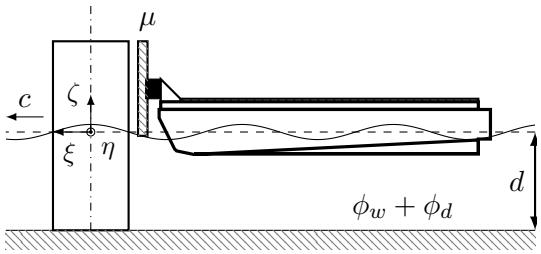

Figure 3.6.: Sideview on boat-landing maneuver of a catamaran at a monopile.

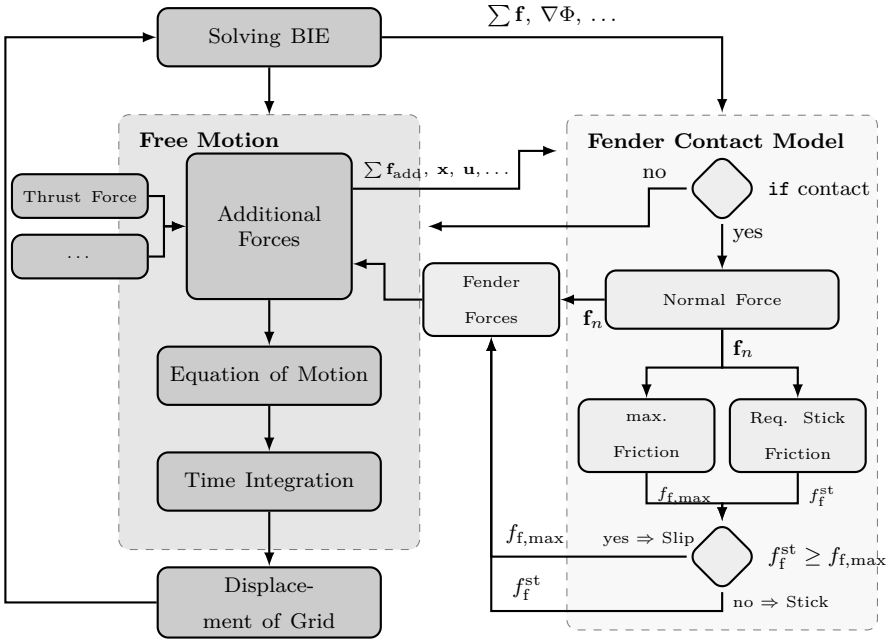

Figure 3.7.: Flow chart of fender contact model within the solving routing of the free motion model.

the Fender contact model solves the contact problem. In Figure 3.7 the flow chart of the contact model is illustrated beside of the model for the free motion calculation. The computation of the fender force starts when all other additional forces are determined. The fender force is introduced as additional force as well.

The contact model firstly checks if the fender is in contact with the boat landing structure or not. If the fender is not in contact, the fender model finishes and returns a zero force vector. Otherwise, in the next step the fender force due to its deformation, see Eq. (2.79), is computed. Here, the pressure force of the fender is modelled using a simple spring damper configuration defined by the spring and damping constant c_f and d_f, thus, the normal force follows:

$$f_\mathrm{f}^n = c_\mathrm{f}\,\Delta x + d_\mathrm{f}\,\dot{x}\,, \tag{3.21}$$

where Δx is the deformation of the fender and $\dot{x}$ is the penetration velocity. Then, the model computes the maximum friction force $f_\mathrm{f}^\mathrm{sl} = f_\mathrm{f,max}$, that can be provided by the connection of the surfaces according to Eq. (2.82). Beside of this, the friction force f_f^st that is required to keep the fender fixed is determined.

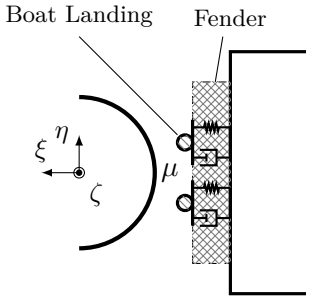

Figure 3.8.: Sketch of contact model between bow fender the two boat-landing struts.

This is done by solving the equation of motion with the force f_f^st as additional unknown following Section 2.5.2. Here, the struts of the boat-landing structure are assumed to be vertical, thus, also the friction acts in the vertical direction $\mathbf{n}_\mathrm{f} = (0,\, 0,\, 1)^T$. Further, the lever of the friction force with respect to the center of the body fixed coordinate system $\mathbf{l}_\mathrm{f} = (\mathbf{n}_\mathrm{f} \times \mathbf{x}_\mathrm{f})^T$, with $\mathbf{x}_\mathrm{f}$ being the local position of the fender.

Then, the 6×6 equation system for solving the accelerations according to Eq. (2.72) can be extended by an additional equation as follows:

$$\left[\begin{array}{ccc|c} m_b\mathbf{E} & 0 & & -\mathbf{n}_\mathrm{f} \\ 0 & \mathbf{J}_b & & -\mathbf{l}_\mathrm{f} \\ \hline \mathbf{n}_\mathrm{f} & \mathbf{l}_\mathrm{f} & & 0 \end{array}\right] \left[\begin{array}{c} \dot{\mathbf{u}}_b \\ \dot{\omega}_b \\ f_\mathrm{f}^\mathrm{st} \end{array}\right] = \left[\begin{array}{c} \mathbf{f} + \mathbf{f}_a \\ \mathbf{m} - \omega_b \times (\mathbf{J}_b \cdot \omega_b) + \mathbf{m}_a \\ \dot{u}_\mathrm{f}' \end{array}\right] . \tag{3.22}$$

Here, $\dot{u}_\mathrm{f}'$ on the right-hand side of the equation system denotes the acceleration that is required to slow down the fender velocity to zero with respect to the time step size Δt. If the fender is already in a stick position, then the acceleration $\dot{u}_\mathrm{f}'$ is zero, otherwise, it follows from Eq. (2.86), thus

$$\dot{u}_\mathrm{f}' = -\frac{1}{\Delta t} \left[u_b + (\omega_b \times \mathbf{x}_\mathrm{f})\right]_\zeta - \left[\omega_b \times (\omega_b \times \mathbf{x}_\mathrm{f})\right]_\zeta . \tag{3.23}$$

According to the relation of both forces in Eq. (2.83), the fender either sticks ($f_\mathrm{f}^\mathrm{st} \leq f_\mathrm{f}^\mathrm{sl}$) or slips ($f_\mathrm{f}^\mathrm{st} > f_\mathrm{f}^\mathrm{sl}$). After determining if the fender slips or not, the contact model returns the respective friction force to the free motion model as additional one. Here, the accelerations are computed and integrated over the time for the next time step.

Two Fender Contacts

So far, only one contact between fender and boat-landing structure is considered. However, in general, the bow fender is pushed against two vertical struts as it is indicated in the sketch in Figure 3.8. Therefore, also the friction forces according to Eq. (2.83) must be computed at two contact positions. Here, the available friction $f_{\mathrm{f}}^{\mathrm{sl}}$ following Eq. (2.82) can be computed independently from each other, but for the computation of the necessary friction $f_{\mathrm{f}}^{\mathrm{st}}$, both fender contacts must be included in the linear equation system in Eq. (3.22). Hence, the equation system of two fender contacts becomes:

$$\left[\begin{array}{cc|cc} m_b\mathbf{E} & 0 & -\mathbf{n}_{\mathrm{f},1} & -\mathbf{n}_{\mathrm{f},2} \\ 0 & \mathbf{J}_b & -\mathbf{l}_{\mathrm{f},1} & -\mathbf{l}_{\mathrm{f},2} \\ \hline \mathbf{n}_{\mathrm{f},1} & \mathbf{l}_{\mathrm{f},1} & 0 & 0 \\ \mathbf{n}_{\mathrm{f},2} & \mathbf{l}_{\mathrm{f},2} & 0 & 0 \end{array}\right] \left[\begin{array}{c} \dot{\mathbf{u}}_b \\ \dot{\omega}_b \\ f_{\mathrm{f},1}^{\mathrm{st}} \\ f_{\mathrm{f},2}^{\mathrm{st}} \end{array}\right] = \left[\begin{array}{c} \mathbf{f} + \mathbf{f}_a \\ \mathbf{m} - \omega_b \times (\mathbf{J}_b \cdot \omega_b) + \mathbf{m}_a \\ \dot{u}'_{\mathrm{f},1} \\ \dot{u}'_{\mathrm{f},2} \end{array}\right] . \tag{3.24}$$

Following the solution of the linear equation system, the resulting friction forces $f_{\mathrm{f},1}^{\mathrm{st}}$, $f_{\mathrm{f},2}^{\mathrm{st}}$ are compared with the available friction forces $f_{\mathrm{f},1}^{\mathrm{sl}}$, $f_{\mathrm{f},2}^{\mathrm{sl}}$, respectively. According to this, three different situations have to be distinguished:

- **Fender sticks at both contact points**: In this case, the determined forces $f_{\mathrm{f},1}^{\mathrm{st}}$, $f_{\mathrm{f},2}^{\mathrm{st}}$ are directly transferred as additional forces to the free motion model to proceed with the solving process of the equation of motion.
- **Slipping at one contact point**: Here, a second iteration has to be considered in which the linear equation system is solved again. However, in contrast to the first pass, the friction force of the fender contact, at which the slipping was detected is assumed to be known and input on the right-hand side of the equation system. Hence, only the friction force $f_{\mathrm{f}}^{\mathrm{st}}$ at the sticking fender contact is recomputed considering the slipping of the other contact. After solving the equation system for the second time, it is checked if the stick condition is still valid or not. According to this result, the respective friction force is hand over to the free motion model for continuing the solution process.
- **Slipping at both contact points**: If the slip-condition is detected for both contact points, the respective difference between available and required friction force $\Delta f_{\mathrm{f}} = |f_{\mathrm{f}}^{\mathrm{st}} - f_{\mathrm{f}}^{\mathrm{sl}}|$ is computed for both contacts, in order to determine the fender that is closer to stick. Then, the friction force of this contact is recomputed, following the actions for the case that only contact point slips.

4. Experimental Investigation

In this chapter the experimental investigations related to the boat landing maneuver of a catamaran vessel are focused on. The major objective of the tests is to provide validation data for the developed numerical method. Furthermore, the experiments are essential to gain more insight into the hydrodynamic interaction between monopile and the maneuvering crew transfer vessel. First, before discussing the experiments and the results, the wave tank and the measurement devices are introduced. In the first test setup, the focus of the experiments lies on the hydrodynamic influence of the monopile and the resulting diffraction of the wave field. Therefore, the elevation of the water surface is measured at several positions in the circumstance of the cylinder in regular waves. The second test setup is addressed to boat landing maneuver itself. Here, the catamaran motion is investigated during the boat landing in regular and irregular sea ways. Apart from the vessel's motion also the forces at the fender which is in contact with the cylinder and either sticks or slips are measured.

4.1. Wave Tank and Measurement Devices

The experimental tests are carried out in the wave tank of the Hamburg University of Technology which is located at the Hamburg Ship Model Basin (HSVA). The dimensions of the tank are shown in the sketch in Figure 4.1. The tank is 80 m long, 5 m wide and has 2.3 m of depth. At one end, the basin is equipped with a wave maker. In a distance

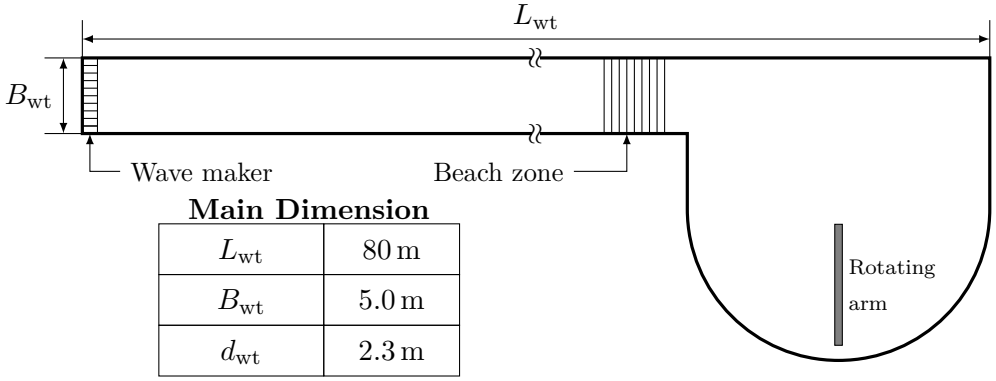

Main Dimension

L_{wt}	80 m
B_{wt}	5.0 m
d_{wt}	2.3 m

Figure 4.1.: Sketch of the towing tank of Hamburg University of Technology (TUHH)

Figure 4.2.: Wave maker of the towing tank of Hamburg University of Technology (TUHH)

of approximately 60 m from the wave maker, an artificial beach is installed to absorb the generated waves. Behind the beach, that optionally can be removed in order to lengthening the distance of measurement, follows the maneuvering basin ($R = 12.5\,\mathrm{m}$) which is equipped with a rotating arm machine for maneuvering tests.

The wave generator implies ten pivot-mounted segments, each with a width of $b_{\mathrm{wg}} = 0.495\,\mathrm{m}$, thus, the total width is $B_{\mathrm{wg}} = 4.94\,\mathrm{m}$. Figure 4.2 shows the wave generator in different views. It can generate different spectra, e.g. JONSWAP or Pierson-Moskowitz. The maximum wave height for regular waves is $\hat{H}_{\mathrm{reg}} = 0.40\,\mathrm{m}$ (at a wave period $T = 3.0\,\mathrm{s}$) and for irregular waves it is $\hat{H}_{\mathrm{irreg}} = 0.27\,\mathrm{m}$.

Measurement devices

The measurement equipment consists of an optical system for the measurement of the vessel motion and, further, of ultra-sonic sensors to record the wave elevation. The optical system includes three infra-red cameras of the company ©Vicon Motion Systems Ltd.[1]. The infra-red camera system belongs to the optical, passive method where markers reflect the infra-red impulses of the camera. The cameras measure the displacement of the reflecting marker probes over the time. According to the displacement the system computes the motion of the marker frame attached to the body in six degrees of freedom. Exemplary, a setup of two cameras which fix a capture volume, in which the system captures the motion of the reflecting markers, and the additional hardware is shown in Figure 4.3.

The infra-red cameras are equipped with multi high velocity processors for an image processing in real time. The motion capturing and analysis of the body as well as the transformation of the data is carried out offline with software provided by ©Vicon Motion Systems Ltd. For further processing the frame rate frequency can be adjusted. The motion of the markers is captured with a frame rate of 50 Hz.

[1] `http://bdml.stanford.edu/twiki/pub/Haptics/MotionDisplayKAUST/ViconHardwareReference.pdf`

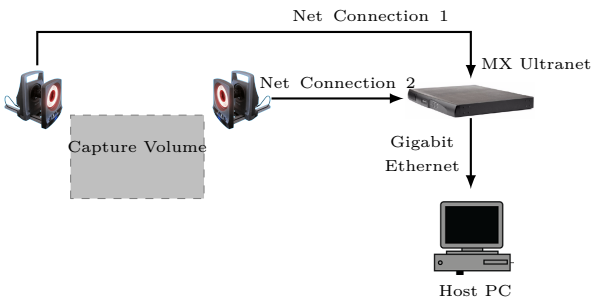

Figure 4.3.: Hardware arrangement of optical infra-red system with two cameras.

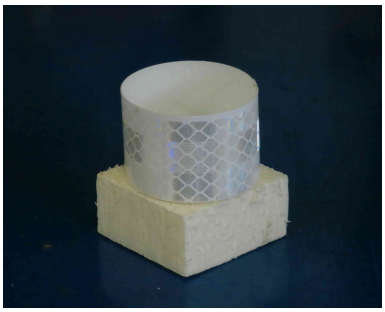

Figure 4.4.: Wave probe with reflecting marker.

Apart from measuring the vessels motion, the system is also used to measure the wave elevation within the experimental investigation of the hydrodynamic influence of the cylinder and its diffraction effects. Here, the measurements of the wave elevation around the cylinder are done by using a number of 48 reflecting marker which are applied as wave probes. They are distributed around the cylinder on the water surface. Details are introduced in the following Section 4.2.

During the experimental investigation of the boat landing maneuver the time dependent elevation of the water surface is measured by ultra-sonic sensors (USS). One of the USS is installed at some distance in front of the cylinder and the catamaran to measure the incoming wave without disturbance. The devices work with an ultrasonsic-impulse-echo-technique. Here, each sensor emits an acoustic impulse which is reflected at the object to be received again at the sensor as an echo. The distance between sensor and object can be minimal 200 mm and maximal 1200 mm. The sampling rate is 50 Hz, the technical resolution is 0.36 mm and the accuracy is ± 1 mm.

4.2. Monopile in Waves

During the landing maneuver, the crew transfer vessel is in contact with monopile via its fender and the boat-landing structure. Apart from this physical contact, the cylinder also effects the vessel motion by means of the hydrodynamic influence. It changes the flow field due to its presence which leads to a diffraction of the incoming waves. The strength of this diffraction depends on the relation between wavelength and cylinder diameter λ_w/D. The influence decreases with increasing wavelength (Chakrabarti 1987, e.g.), and for relatively long waves the cylinder does not have a significant effect, thus it can be regarded as transparent. In the following, the hydrodynamic influence of the cylinder is experimentally investigated by measuring the diffraction effects on the water surface for regular waves using the infra-red camera system and various wave probes which are distributed in the circumstance of the cylinder on the water surface.

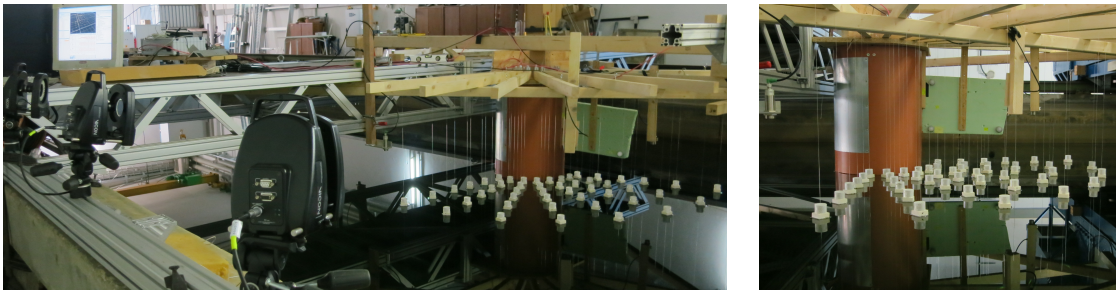

(a) Overview **(b)** Side view

Figure 4.5.: Test setup for measurements of the diffraction caused by a cylinder

The monopile is modelled using a PVC tube with a diameter of $d_{\mathrm{mp}} = 0.5\,\mathrm{m}$ which is installed in the towing tank. Assuming a model scale factor of $\lambda = 1:10$, it corresponds to a pile with 5 m of diameter. The frequency of the tested regular waves is varied between $\omega_w = 1.65\,\mathrm{rad\,s^{-1}}$ to $5.0\,\mathrm{rad\,s^{-1}}$. Following the model scale, this meets the wave periods $T_{w,fs} = 4\,\mathrm{s}$ to 12 s in full-scale. In the following, the experimentally investigated waves will be distinguished by its wave frequency ω_w and the non-dimensional wavelength λ_w/D.

Test Setup

The experimental setup includes the monopile model in the wave tank and the surrounding wave probes for measuring the wave elevation. The monopile ($l_{\mathrm{mp}} = 3.0\,\mathrm{m}$) stands on the bottom of the tank and is kept fixed by attaching the top part of the cylinder to the transverse bridge of the tank.

Four ultrasonic wave probes provide accurate data of the water elevation at discrete positions. Furthermore, 48 marker probes are used to measure the wave elevation to cover the regarded water surface in a sufficiently manner, so that the impact due to the presence of the cylinder can be shown. Figure 4.4 exemplary presents a reflecting marker. Each of those probes consists of a rectangle Styrofoam plate and a circular band made of reflecting material.

The reflecting markers are floating on the water surface, and they only are allowed to move along vertical nylon threads which avoid that the horizontal positions of the probes shift during the tests. Therefore, the threads are connected to a wooden frame above the water surface and to weights under the water holding them tight. The weights hang just above the tank bottom and are hardly influenced by the waves due to tension and their horizontal displacement during the trials is very small ($\pm 5\,\mathrm{mm}$), so the error for the measured amplitudes due to the horizontal displacement can be neglected. The wooden frame consists of eight beams radially distributed (15° spacing) from $-15°$ to 90° with respect to the x-axis. At each beam six nylon threads including the wave probes are

connected. The radial distances of the wave probes from the center of the cylinder (or the origin of the coordinate system) vary as follows: $r_{\mathrm{wp}} = 0.35\,\mathrm{m}$, $0.50\,\mathrm{m}$, $0.65\,\mathrm{m}$, $0.80\,\mathrm{m}$, $1.00\,\mathrm{m}$ and $1.25\,\mathrm{m}$. The photos and the sketch in Figures 4.5a - 4.5b give an overview of the monopile, the wooden frame with the probes in the vicinity of the cylinder and the infra-red cameras, which are attached to the tank walls.

The horizontal position of the USS and the 48 markers are shown in the graph in Figure 4.6. Here, c denotes the direction of the incoming waves. Referring to polar coordinates, the ultrasonic sensors USS2, USS3 and USS4 are located at angles $\beta \approx 90°$, 45° and 0° around the monopile. The wave probe USS1 is used as reference to measure the incoming wave without influence of the cylinder. Therefore, it is located far before the cylinder and therefore not illustrated in Figure 4.6.

The mass of each probe approximately is $m_{\mathrm{wp}} \approx 0.003\,\mathrm{kg}$ and the waterline area of the Styrofoam plate is $A_{wl,\mathrm{wp}} = 0.04\,\mathrm{m} \times 0.04\,\mathrm{m}$. Assuming the added mass to be $a_{\mathrm{wp}} = m_{\mathrm{wp}}$, the first eigenfrequency for the heave motion of the probe is $\omega_{0,\mathrm{wp}} = 48.6\,\mathrm{rad\,s^{-1}}$. The wave frequencies investigated in the tests are much smaller, thus, the motion of the Styrofoam plates is dominated by hydrostatic effects and the relation between the amplitude of the probes and the wave amplitude $|\zeta_{\mathrm{wp}}| \,/\, |\zeta_w|$ can be assumed to equal one. Possible errors of the measurement can occur due to the inertia of the probes, due to friction between the nylon thread a Styrofoam plate. Therefore, in the following the measurements of an exemplary probe are compared with data provided by an ultrasonic probe.

Test of Wave Maker Performance

First, the waves which are generated by the wave maker are tested. Here, the amplitude measured by the ultra-sonic sensor USS1, which is installed at some distance in front of the cylinder, is compared with the desired wave amplitude for the different angular frequencies to verify that the wave generator delivers the target waves. In Table 4.1 the measured wave amplitudes for the different frequencies or wavelengths per diameter

Table 4.1.: Comparison of target and actual wave amplitudes generated by the wave maker.

Input Wave		Mean Amplitude	Std. Deviation	Mean Error
$\omega, \mathrm{rad\,s^{-1}}$	λ_w/D	$\hat{\zeta}_{\mathrm{uss1}}, \mathrm{mm}$	σ, mm	$\Delta\hat{\zeta}, \%$
1.65	35.565	45.635	0.007	8.729
2.50	18.994	49.092	0.014	1.816
3.00	13.591	46.510	0.162	6.980
3.50	10.063	49.612	0.334	0.777
4.00	7.705	47.113	0.231	5.774
4.50	6.088	50.357	0.168	0.715
5.00	4.931	47.994	0.061	4.011
Mean Values		48.045	0.140	4.115

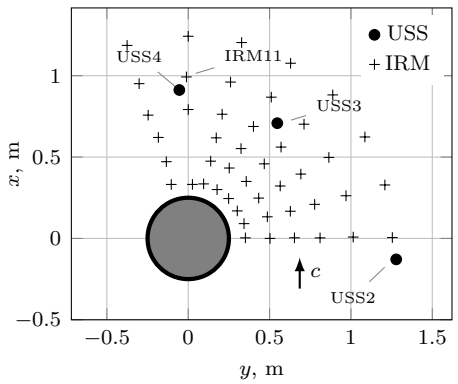

Figure 4.6.: Position of the four ultrasonic sensors (USS) and the 48 infra-red markers (IRM).

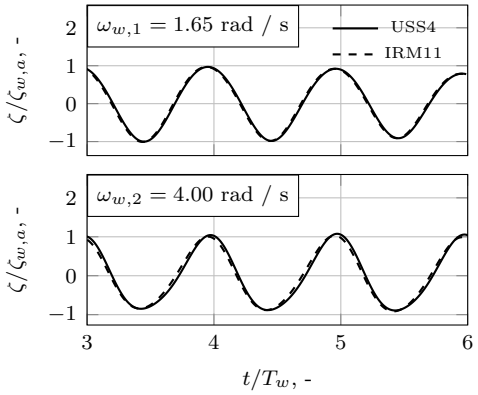

Figure 4.7.: Comparison of measured water elevation for two different wave frequencies using USS and IRM, respectively.

λ_w/D are listed. Here, the target wave amplitude is $\hat{\zeta}_{\text{target}}$ =0.05 m. Three to four test runs are carried out for each wave frequency and the mean value over the repeated test runs are computed. Further, the standard deviation σ and the mean relative deviation $\Delta\hat{\zeta}$ from the target value ζ_{target} is presented. First of all, the results show that the maximum relative deviation $\Delta\zeta$ for all regarded wave frequency is below 9 % and the mean error is 4.1 %. Further, the accuracy of the generated wave amplitudes strongly differs for the respective wave frequencies. On the one hand, regarding the wave frequencies $\omega = 2.50\,\text{rad}\,\text{s}^{-1}$, $3.50\,\text{rad}\,\text{s}^{-1}$ and $4.50\,\text{rad}\,\text{s}^{-1}$ the respective error is $\Delta\zeta \leq 2\,\%$, on the other hand the deviation for the frequencies ω =$1.65\,\text{rad}\,\text{s}^{-1}$, $3.00\,\text{rad}\,\text{s}^{-1}$, $4.00\,\text{rad}\,\text{s}^{-1}$ and $5.0\,\text{rad}\,\text{s}^{-1}$ is in the domain $\Delta\zeta$ = 4.0 % to 8.75 %. The standard deviations of the test runs demonstrate that the measured wave amplitudes hardly differ. This indicates that it is not a random error causing the deviation, but it depends either on the characteristic of the wave maker or on the measurement position of USS1 which could be situated too close to the wave maker where the waves are not yet fully developed.

Validation of Measurement System

The introduced method to measure the water elevation around the monopile by an optical infra-red system is innovative and still not well validated. As already mentioned, errors can for example occur due to the inertia of the wave probe or due to the friction at the nylon thread. First, the measurement of the infra-red system is compared with the more accurate results of the ultrasonic sensor to to proof if the system is suitable for the supposed trials. Here, the measured data from the infra-red marker probe IRM11, see Figure 4.6, are compared with the measurement of the ultrasonic sensor USS4 for the two wave frequencies ($\omega_{w,1} = 1.65\,\text{rad}\,\text{s}^{-1}$, $\omega_{w,2} = 4.0\,\text{rad}\,\text{s}^{-1}$). In Figure 4.7 the measured wave elevations are plotted over the time. The plots generally show a good agreement of the results of the two measurement methods. Slight differences can be observed for the

wave frequency $\omega_{w,2} = 4.0\,\mathrm{rad\,s^{-1}}$, but the small error seems acceptable, in particular, as the main objective of the waterplane measurements is to show the relative property change of the wave due to the presence of the monopile.

Cylinder Diffraction

In the experiments, the diffraction due to the presence of the monopile is investigated in regular waves with different angular frequencies. The results of the surface measurements in regular waves are shown for the four angular frequencies: $3.0\,\mathrm{rad\,s^{-1}}$, $4.0\,\mathrm{rad\,s^{-1}}$, $4.5\,\mathrm{rad\,s^{-1}}$ and $5.0\,\mathrm{rad\,s^{-1}}$, in Figures A.1a - A.1d in the Appendix A.1. Here, the elevation of the water surface in circumstance of the cylinder is plotted for each frequency in four graphs which denote the four phases $\varphi = 1/2\,\pi, \pi, 3/2\,\pi$ and 2π of the harmonic oscillation. The experiments meet the expectation that the influence increases with increasing wave frequency. Therefore, waves with frequencies lower than $\omega_w = 3.0\,\mathrm{rad\,s^{-1}}$ for which the hydrodynamic influence of the cylinder almost vanishes and does not have any recognizable effect on the water surface are not documented.

In contrast to this, the influence of the cylinder is significant for the highest tested wave frequency $\omega_w = 5.0\,\mathrm{rad\,s^{-1}}$ as shown in Figure 4.8. Here, the water elevation in the circumstance of the cylinder in regular waves is shown for the four-time instances represented by the discrete phases $\varphi = 1/2\,\pi, \pi, 3/2\,\pi$ and 2π of the oscillating elevation, respectively. The phases π and 2π denote the moment when the wave trough and the wave crest respectively cross the transverse center line of the cylinder. The graphs on the left-hand side in Figure 4.8 plot the water elevation which follows from the measurements during the experiments. Regarding this, a significant influence of the cylinder on the elevation can be observed. To show the influence more clearly it is separated from the incoming wave by computing the difference between the undisturbed water wave and the actual measured wave: $\zeta_d = \zeta - \zeta_w$. The results are plotted in the graphs on the right hand side.

Following the two graphs in Figure 4.8a for the phase $\varphi = 1/2\pi$, when the wave crest has already crossed the cylinder, the maximum elevation directly behind the cylinder is increased and the cylinder diffraction induces a wave trough beside of the cylinder. It radiates outwards and increases at some distance from the cylinder the trough of the incoming wave as it can be seen in Figure 4.8b. At the same time, the trough near the cylinder is reduced by the locally induced wave crest which then is also radiating outwards, see Figure 4.8c. At $\varphi = 2\pi$ the crest of the incoming wave travels alongside of the cylinder. The plot further demonstrates that behind the cylinder, the wave trough due to the diffraction partly eliminates the increased elevation.

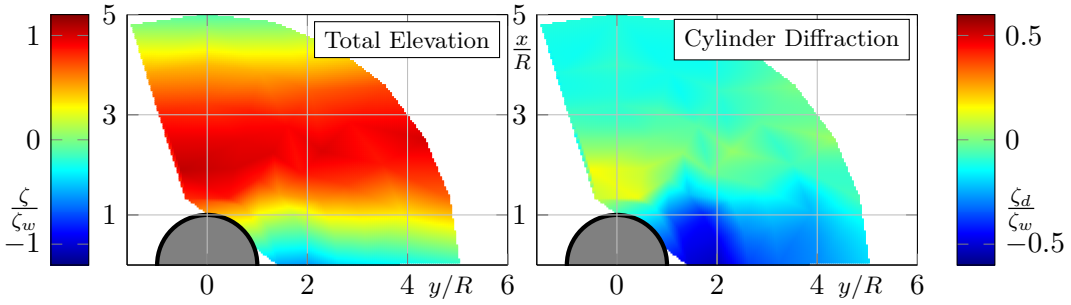

(a) $\varphi = \frac{1}{2}\pi$

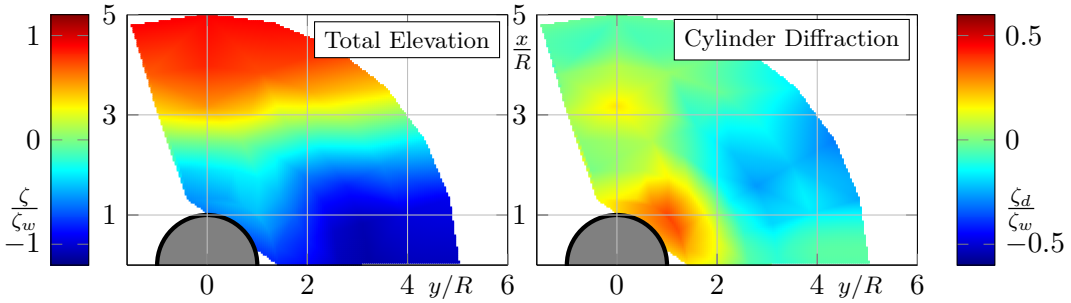

(b) $\varphi = \pi$

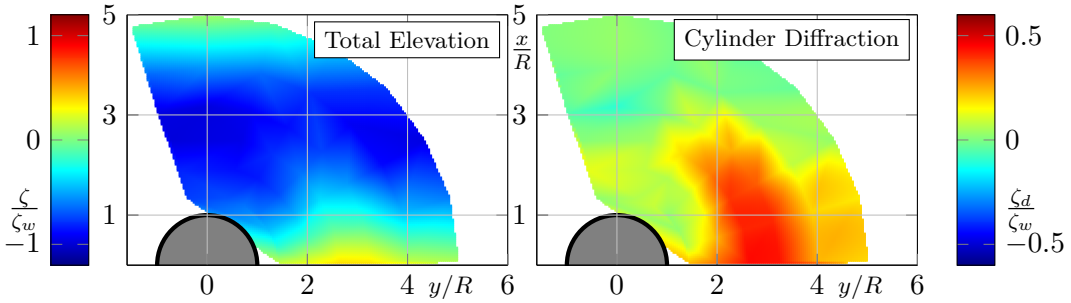

(c) $\varphi = \frac{3}{2}\pi$

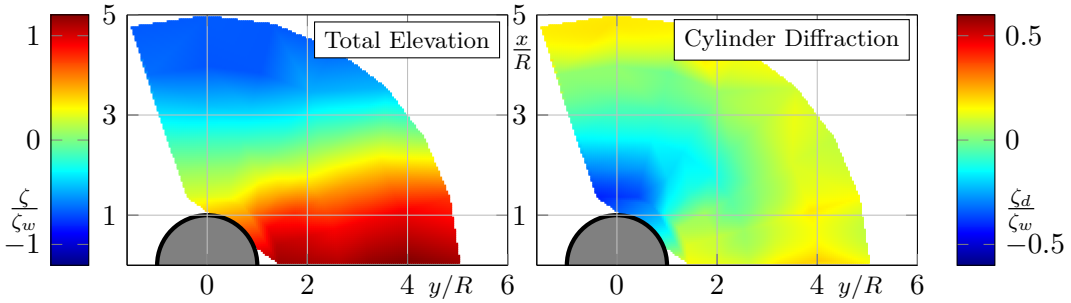

(d) $\varphi = 2\pi$

Figure 4.8.: The total water elevation and the elevation due to the cylinder diffraction in circumstance of the cylinder in regular waves ($H_w = 0.1\,\mathrm{m}$, $\omega_w = 5.0\,\mathrm{rad\,s^{-1}}$).

4.3. Landing Maneuver

The experimental investigation regarding the landing maneuver of a crew transfer vessel at an offshore foundation are conducted with the aim to analyze the hydrodynamic interaction between the moving vessel and the monopile and to provide validation data for the numerical method. Within the experimental investigations, two different catamaran models as crew transfer vessels are tested. Both are remotely controlled and move freely during the landing maneuvers tests which are carried out in regular as well as in irregular waves.

4.3.1. Catamaran Models

In the following, the two catamaran models are considered in the experimental study referred to as *Model 1* and *Model 2*. In Table 4.2 the main dimensions of the catamarans and their mass information are listed. Assuming a model scale of approximately $\lambda_{\text{geo}} \approx 1:10$, the models would represent crew transfer vessels of approximately 22 m length. Figure 4.9 shows the manufactured catamaran of *Model 1*. For each of the two catamaran models, both hulls are provided with a propulsion system which respectively consists of a propeller, a gear, an electric motor and batteries. The propulsion and maneuvering systems of the models can be controlled independently via the remote control during the tests. Comparing the two models, the propulsion systems differ as follows: *Model 1* is equipped with two Z-drives, each of them has a four-bladed propeller with a diameter of $D_p = 0.09\,\text{m}$, see Fig. 4.10a. In contrast to this, the two hulls of the catamaran *Model 2* are respectively equipped with a fixed pitch propeller (FPP) with five blades and a spade rudder, see Fig. 4.10b.

A bow fender is attached at each bow of the catamaran models. *Model 1* is equipped with a generic D-profile rubber fender which was experimentally analyzed before the hydrodynamic tests by the Institute for Ship Structural Design and Analysis, see König et al. (2017). In this case, the fender geometry is not scaled related to the model scale of the catamaran. Instead, the same fender geometry is used as for the structural tests to avoid scale effects related to the structural properties of the fender. Consequently, the fender geometry does not correspond to the fender of a full-scale vessel. The fender is attached via two pairs of load cells at starboard and port side of the catamaran to the

Table 4.2.: Main dimensions and inertia properties of models.

Main dimension			*Model 1*	*Model 2*	Inertia		*Model 1*	*Model 2*
Length	L_{oa}	m	2.2	2.13	m_b	t	0.079	0.060
Draft	T	m	0.12	0.15	z_{cg}	m	0.174	0.23
Breadth	B	m	0.8	0.79	I_{xx}	kg m^2	11.32	3.50
					I_{yy}	kg m^2	34.86	24.50

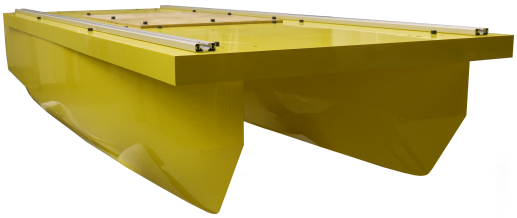

Figure 4.9.: Catamaran *Model 1* for landing maneuver experiments.

(a) *Model 1* **(b)** *Model 2*

Figure 4.10.: Propulsion systems of tested catamaran models.

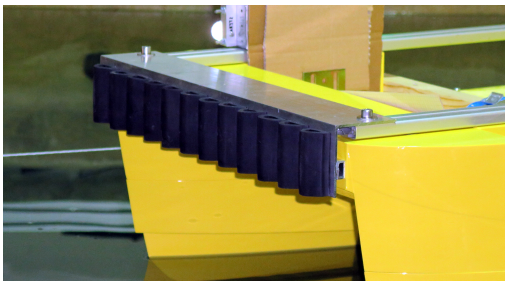

Figure 4.11.: Bow fender of catamaran *Model 2*.

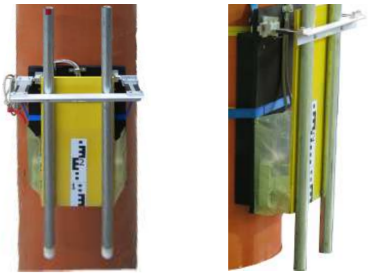

Figure 4.12.: Boat landing structure at monopile model.

bow of the vessel. These load cells measure the contact forces in axial and tangential direction. Further, they have a sampling rate of 50 Hz and an accuracy of 99.9 %. The measuring range of the load cells for the axial forces and the tangential force is 500 N and 200 N, respectively.

In contrast to the first model, the catamaran *Model 2* is equipped with a rubber fender which is scaled regarding the model scale λ_{geo}. The bow fender is shown in Figure 4.11. Similar to the setup of *Model 1*, two pairs of load cells are applied for the measurement of the contact forces. Although, in this case, they are not installed directly at the fender attachment but at the boat-landing structure, which is demonstrated in Figure 4.12. Speaking more precisely, the load cells are installed between the two vertical struts of the boat-landing structure and the monopile model.

4.3.2. Test Setup

An overview of the test setup for the boat landing maneuver experiments is sketched in Figure 4.13. Here, a cylinder which is installed on the tank bottom is used for the model of the monopile. It has the diameter $d_{\text{cyl}} = 0.5\,\text{m}$ and corresponds to the model which has been applied for the experimental investigation related to the cylinder diffraction, see Sec. 4.2. The water elevation is measured during the tests at least at two locations by ultrasonic sensors (USS) with a sampling rate of 50 Hz. The motion of the vessel is

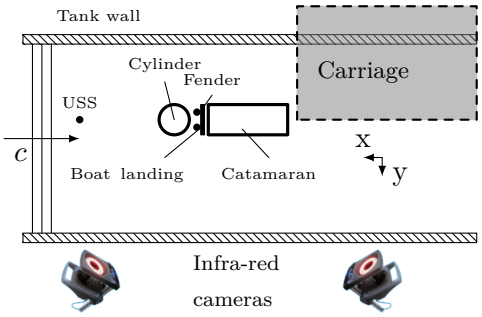

Figure 4.13.: Overview of setup of landing maneuver experiments.

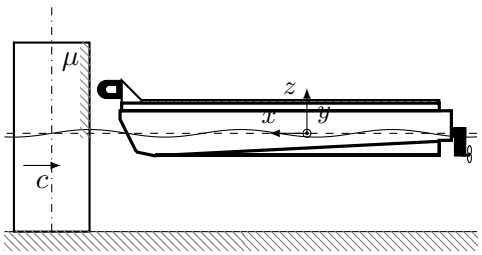

Figure 4.14.: Side view of *Model 1* with D-profile bow fender.

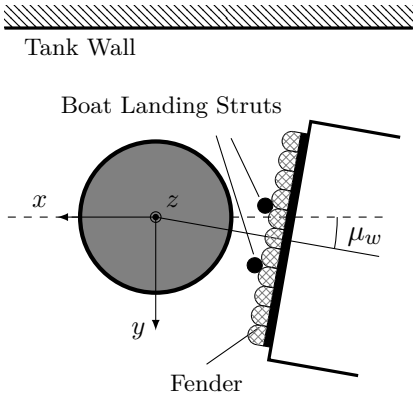

Figure 4.15.: Sketch of fender pushing against boat-landing struts and definition of the wave encounter angle μ_w.

recorded by the optical system with two infra-red cameras capturing the reflections of a four-marker cross which is attached to the bow of the catamaran near of the fender. The infra-red system's sampling rate is 100 Hz.

For the first landing maneuvers tests, in which the catamaran *Model 1* is tested, the boat-landing struts are omitted, Instead, the bow fender of the model is pushing directly against a steel sheet on the cylinder surface, see also Fig. 4.14. The intention thereby is to stress the bow fender in a same manner as stressed in the structural tests by the Institute for Ship Structural Design and Analysis, so that the structural behavior of the fender is comparable.

The setup is modified for the catamaran *Model 2*. Here, the boat-landing structure, see Fig. 4.12, is added to the monopile. As already mentioned, it consists of two stiff tubes ($d_{tu} = 34\,\text{mm}$) which are installed with 0.368 m distance referring to the cylinder center. The distance between the two tubes is $\Delta y_{tu} = 0.18\,\text{m}$ and it is chosen regarding the widths of the single fender parts of the model so that the vessel does not tend to yaw by pushing against the boat-landing structure. In this setup, the force sensors are not at

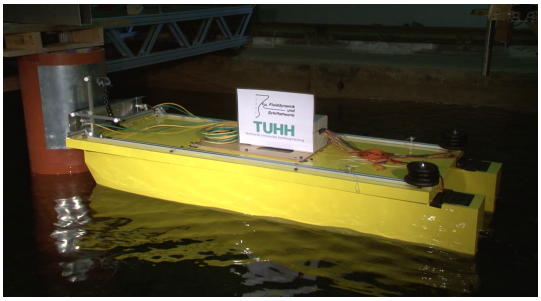

(a) Catamaran *Model 1*

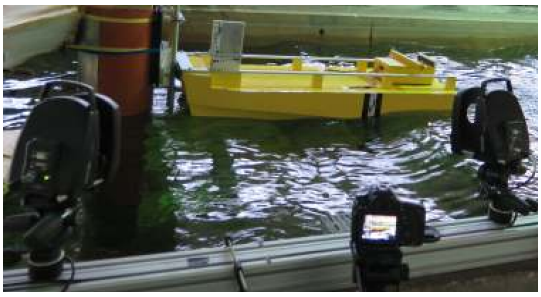

(b) Catamaran *Model 2*

Figure 4.16.: Catamaran models during boat-landing maneuver tests.

the connection between fender and vessel, instead, sensors for the force measurements are connected between the boat-landing struts and the cylinder. Furthermore, the setup with the boat-landing struts allows to vary the encounter angles of the waves μ_w by rotating the struts position around the cylinder center as illustrated in Figure 4.15.

4.3.3. Experimental Results

In the following, the results of the experimental investigation of the landing maneuver are summarized. During the tests the propulsion system of the catamaran is controlled remotely. Between the trials, the surface of the fender as well as of the monopile steel sheet are sprinkled with water to keep them wet. Before the wave generator starts to work, the catamaran already pushes with its bow fender against the boat-landing structure.

Figure 4.16 exemplary shows photos of both catamaran models during the boat-landing maneuver tests in the wave tank. As already mentioned, a boat-landing structure is omitted for the tests conducted with *Model 1*. The tests are carried out in regular and irregular waves. During the tests waves radiates from the cylinder and the moving catamaran away and are reflected by the tank walls. Due to the relatively limited tank width, it is expected that the error caused by the wave reflection increases over the time. Therefore, the time window for the measurements must be limited. Some of the measured results are discussed in the following.

Regular Waves

First, the catamaran *Model 1* is tested in regular waves. The lengths and heights differ as follows: $\lambda_w = 1.75 - 13.0$ m, $H_w = 0.04 - 0.08$ m. During the tests the catamaran pushes with its fender against the cylinder. Here, the thrust of the propulsion system is set high enough that the fender remains fixed at the cylinder surface and does not start to slip.

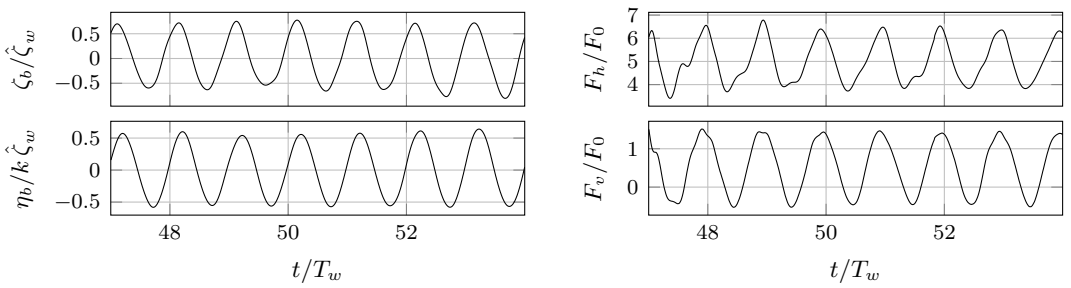

(a) Heave and pitch motion

(b) Horizontal and vertical fender force

Figure 4.17.: Time records of the non-dimensional heave and pitch motion and the fender forces for the catamaran *Model 1* in regular waves ($H = 0.6\,\mathrm{m}$, $\lambda_w/L = 2.27$). The time is made dimensionless by the wave period T_w, the motion by the wave amplitude $\hat{\zeta}_w$ and the wave steepness $k\hat{\zeta}_w$, and the forces by $F_0 = \rho\, g\, \hat{\zeta}_w^2\, L$.

In Figure 4.17a the non-dimensional heave and pitch motion are plotted against the non-dimensional time t/T_w for the case that the catamaran is in contact with the cylinder in regular waves with a dimensionless length $\lambda_w/L = 2.27$. The graphs demonstrate that the heave and pitch motion of the catamaran in this case are oscillating harmonically. The plots in Figure 4.17b show the time records of the measured contact forces at the fender in horizontal and vertical direction. The forces are made dimensionless with a wave amplitude depending reference force $F_0 = \rho\, g\, \hat{\zeta}_w^2\, L$. According to the plots, the forces harmonically oscillate, and the frequency coincides with the exciting frequency of the waves. Further, the plotted forces over the time indicate non-linear effects, in particular, for the horizontal part F_h which may be introduced by the propeller wave interaction or the non-linear behavior of the fender.

The response amplitude operators for the heave and pitch motion of the catamaran are plotted against the non-dimensional wavelength in Figure 4.18. Apart from the RAO for the catamaran during the boat-landing (contact), also the RAOs for the case that the fender is not in contact with the cylinder and the catamaran can freely move in the circumstance of the cylinder (free) are presented. Here, the circles denote the amplitudes for the freely moving model and the crosses represents the values for the case that the bow fender of the model is in contact with the monopile. According to the plots, the contact with the monopile significantly changes the RAO of the catamaran in heave and pitch. In general, the contact with the structure leads to smaller motion amplitudes in heave and pitch. Due to the contact, the fender is constrained and forced to keep fixed instead of sliding up- and downwards along the cylinder surface. This means the contact can be seen as a hinge which then consequently is also the center of rotation related to the pitch motion. Therefore, in contrast to the RAO for the freely moving catamaran, for the contact condition the response amplitudes of the pitch motion do not converge to 1.0 with increasing wavelength. As the center of rotation is shifted to the contact position, also the evaluated heave motion which is generally defined at the center of

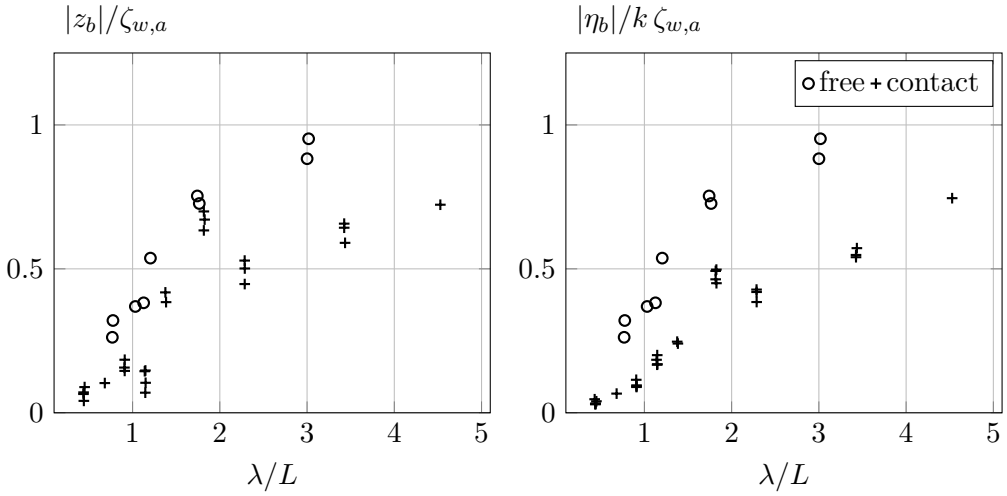

Figure 4.18.: Response amplitude operators for the heave and pitch motion of the catamaran *Model 1* for the two cases: 1. the model is freely moving in the circumstance of the cylinder (free); 2. the fender of the catamaran is in contact with the monopile model (contact).

gravity becomes dependent from the pitch motion. Therefore, the local maximum of the pitch motion at a non-dimensional wavelength $\lambda_w/L \approx 1.82$ also leads to a peak at the heave motion.

Irregular Waves

In this section, the experimental investigation regarding the behavior of the catamaran vessels during the boat-landing maneuver in irregular waves is described. The sea states which are produced by the wave generator are based on JONSWAP spectra. Within the test series, sea states with different significant wave heights $H_s = 0.100\,\mathrm{m}$, $0.125\,\mathrm{m}$ and $0.150\,\mathrm{m}$ and associated peak frequencies $\omega_p = \pi/(2\sqrt{H_s})$ are applied. In addition to the cases, in which the encounter angle of the waves is zero degree (head waves), here, two further encounter angles ($\mu_w = 10°$, $15°$) are considered. This is realized by rotating the boat-landing structure around the cylinder as already described in Section 4.5. Again, the catamaran starts to push the fender against the boat-landing structure before it is encountered by the waves and the propeller speed is kept constant during the tests, as before. Although, between separate tests, the propeller thrust is varied by in- or decreasing the speed of the propellers, thus, the bow fender is forced to slip or to keep stick. The photos in Figure 4.19 exemplary illustrate the strong motion of the catamaran in the instance of time when the fender accidentally slips.

In the following, the measured data of a two boat-landing maneuvers in irregular waves (JONSWAP: $H_s = 0.1\,\mathrm{m}$, $\omega_p = 4.97\,\mathrm{rad\,s^{-1}}$, $\mu_w = 0°$) are plotted, see Fig. 4.20. On

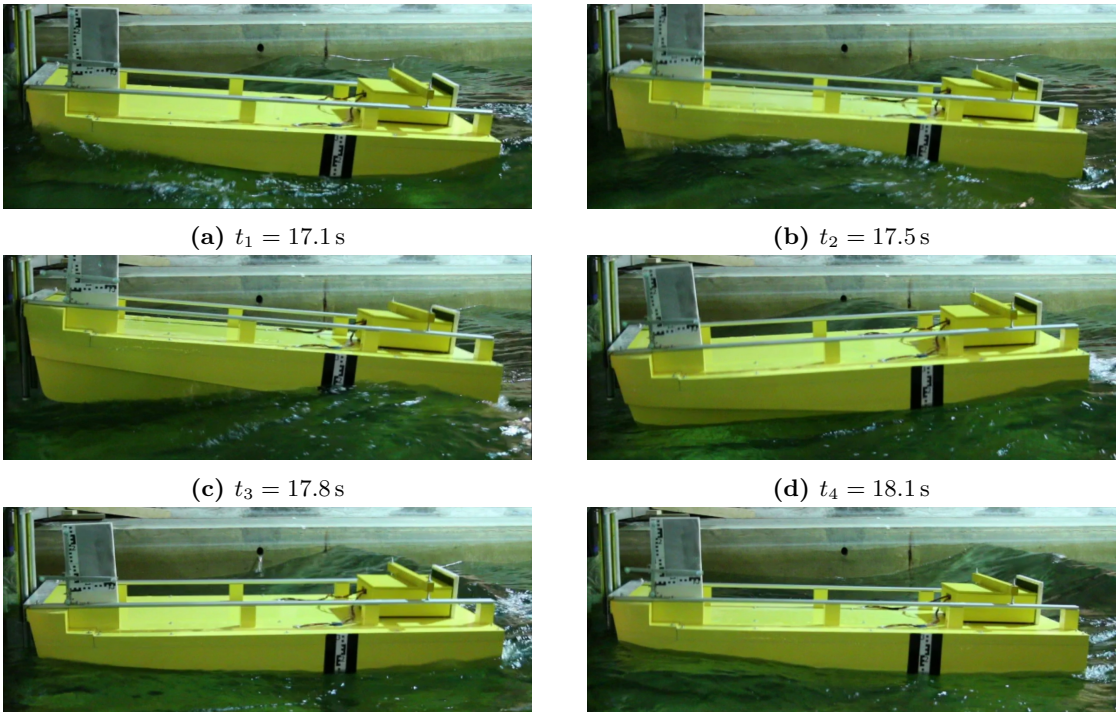

(a) $t_1 = 17.1\,\mathrm{s}$ **(b)** $t_2 = 17.5\,\mathrm{s}$

(c) $t_3 = 17.8\,\mathrm{s}$ **(d)** $t_4 = 18.1\,\mathrm{s}$

(e) $t_5 = 18.4\,\mathrm{s}$ **(f)** $t_6 = 18.8\,\mathrm{s}$

Figure 4.19.: Occurrence of slip of bow fender during landing maneuver test of catamaran *Model 2* (JONSWAP: $H_s = 0.125\,\mathrm{m}$, $\omega_p = 4.44\,\mathrm{rad\,s^{-1}}$, $\mu_w = 10°$).

the left-hand side, the wave elevation ζ_w, the heave and pitch motion of the center of gravity ζ_b, η_b are plotted over the time t. Here, the wave elevation and the heave motion are made dimensionless using the significant wave height H_s of the sea state and the pitch by $\eta_s = 1/2\, H_s\, \omega_p^2/g$. The wave elevation is measured by the USS that is located 8 m in front of the cylinder. On the right-hand side, the vertical force at the fender F_v, the heave displacement and velocity of the fender $\Delta\zeta_\mathrm{f}$, $\dot{\zeta}_\mathrm{f}$ are plotted against the time t. The force is made dimensionless using the product of the gravitational acceleration g and the catamaran mass m_b.

The two presented cases in the plots differ regarding the thrust force with which the fender of the catamaran *Model 2* is pushed against the boat-landing structure. Here, the thrust of the vessel $T_{\mathrm{prop},1}$, which is applied in the first case, is more than the double compared to the thrust $T_{\mathrm{prop},2}$ in the second case. Hence, in the first case the fender is kept stick at the boat-landing whilst in the second case the thrust force is not high enough to keep the fender fixed at one position, thus, at an instance of time slip occurs. According to the measurements the time records of the wave elevation the waves which encounter the catamaran in both cases are the almost same. Also, the heave and pitch motion in both cases coincides until the fender of the catamaran in the second test case suddenly starts to slip. This slip occurrence at the time $t_s \approx 16$ s can clearly be seen following the plot of the displacement of the fender Δ_f. According to this, after a sudden movement upwards the fender slides again downwards but stays fixed at a higher position than before. In contrast to this, the black curve demonstrates that in the first case, the fender remains fixed. In addition to this, the plots of the heave and pitch motion indicate that both shift towards an equilibrium position due to the higher rest position of the fender. Similar can be stated regarding the vertical Force F_v which oscillates around a positive mean value after the fender of the catamaran moved upwards.

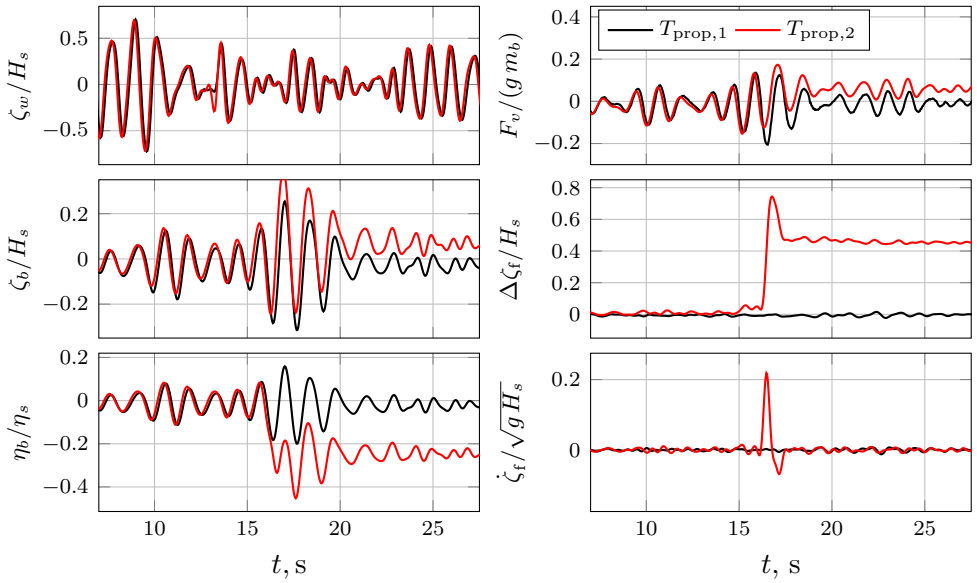

Figure 4.20.: Boat-landing maneuvers of catamaran *Model 2* in irregular waves (JONSWAP: $H_s = 0.1\,\text{m}$, $\omega_p = 4.97\,\text{rad}\,\text{s}^{-1}$, $\mu_w = 0°$) under consideration of different propeller thrust forces: $T_{\text{prop},1} = 123.84\,\text{N}$, $T_{\text{prop},2} = 52N$).

5. Numerical Simulation of the Boat-landing Maneuver

This chapter deals with the validation of the developed models which have been implemented into the boundary element method *pan*MARE and the numerical simulation of the boat-landing maneuver. First, the free surface simulation model is validated by comparing the numerical results of wave-body interaction problems with those of other publications. Further, the tank test results of the cylinder diffraction are compared with the results obtained by *pan*MARE. In addition to this, the behavior of contact model is verified. At the end, the boat-landing maneuver of a catamaran crew transfer vessel is compared with the experiments discussed in Section 4.3.

5.1. Validation of Free Surface Model

In this section, the validation of the developed free surface model is presented. First, the intersection waterline between body and free water surface, which is a problematic numerical issue, is avoided by focusing on hydrodynamic problems of ellipsoids below the free surface. After this, wave-body problems in which a waterline must be considered are addressed by simulating the standing cylinder (zero speed) in waves and Wigley hulls with forward speed in waves. Concerning the cylinder test case, the hydrodynamic forces are computed and validated using published data. Furthermore, the wave diffraction in the circumstance of a cylinder is compared with the results from the tank tests, see Section 4.2. Further regarding the test cases of the Wigley hulls, two different geometries are considered and the hydrodynamic forces as well as the free motion are computed and compared with experimental results presented by Kashiwagi 2013.

5.1.1. Hydrodynamic Loads on Submerged Bodies

First, the validation of the free surface model focuses on hydrodynamic problems of submerged bodies. Here, the cases address the steady resistance problem of a spheroid below the free surface and the diffraction and radiation of an underwater sphere in waves. The results of the present simulations are compared with published data from other potential flow methods.

Wave Resistance of a Sphere below the Free Surface

In the following, the wave resistance of a prolate spheroid travelling forward beneath the water surface is calculated. The spheroid has the length $L = 12\text{m}$. It is defined by the two radii a and b, see Fig. 5.1, and its draft is d. The focus is denoted by $c = \sqrt{a^2 - b^2}$. The center of the coordinate system is assumed to be on the undisturbed free surface. The position of the spheroid referred to the free surface is defined by its center $\xi_{\text{cog}} = (0, 0, -d)^T$ and its motion velocity by the vector $\mathbf{u} = (u,\, 0,\, 0)^T$.

Although, the computation of the resistance is a stationary problem, here, it is treated as instationary. It is assumed that at the begin of the simulation ($t_0 = 0\,\text{s}$), the free surface is undisturbed and the induced potential and the induced velocities in the computational domain are zero. Directly starting the simulation with the forward speed u would result in a sudden increase of the induced values. Hence, this would invoke strong oscillating forces which converges slowly. Therefore, the initial velocity of the body $u_0 = u(t = 0)$ is almost zero at the first time step and then increased over the time by a temporal ramp:

$$u_t = u - (u - u_0)\, \cos\left(\frac{\pi\, t}{2\Delta t_{\text{r}}}\right)^2 , \tag{5.1}$$

where Δt_{r} is the time range of the ramp.

Figure 5.2 shows a mesh of the spheroid below the free surface for the Froude number $F_n = 0.6$. Taking advantage of the plane symmetry at the longitudinal center line of the spheroid, only the half surfaces of the body and the free surface are modeled. The body is discretized by $70 \times 20 = 1400$ panels whilst the undisturbed free surface plane is modeled by 45×91 panels. In this case, a high resolution of the body discretization is necessary to compute the resistance in an accurate manner. This is particularly important for small Froude numbers as the wavelength, which can be approximated by Eq. (5.2), becomes small. The free surface is described by an orthogonal grid. The length of the free surface domain l_{fs} is chosen according to the Froude number, thus, the distance $l_{fs,1}$ between the stern of the spheroid and the end of the free surface domain is approximately three wavelengths. Here, the length is approximated by the equation for a trochoidal wave:

$$\lambda_w \approx 2\,\pi\, F_n^2\, L\,. \tag{5.2}$$

The breadth of the domain is set considering that the propagation of the induced waves is depending on the Froude number and the Kelvin angle κ. Therefore, the breadth should be at least equal or greater than $b_{fs,\min} = l_{fs,1}\, \tan(\kappa)$, where $\kappa \approx 19.5$ denotes the Kelvin angle. The panel size in longitudinal direction δ_ξ is defined, according to number of panels per wavelength $n_{\xi,\lambda} = 25$ and the number of wavelengths $N_\lambda = 2$.

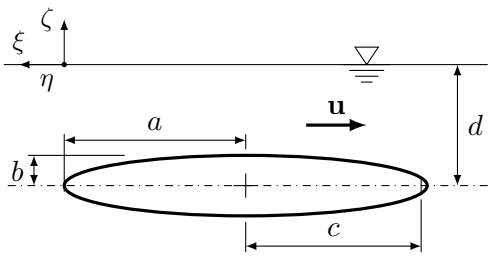

Figure 5.1.: Sketch of spheroid travelling under the free water surface.

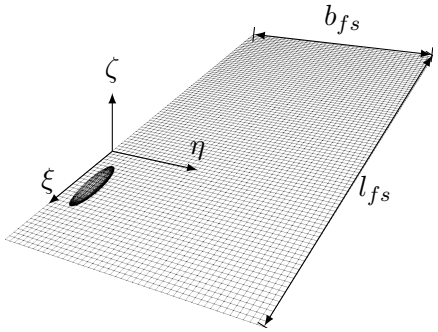

Figure 5.2.: Mesh for simulation of spheroid below the free water surface ($F_n = 0.6$).

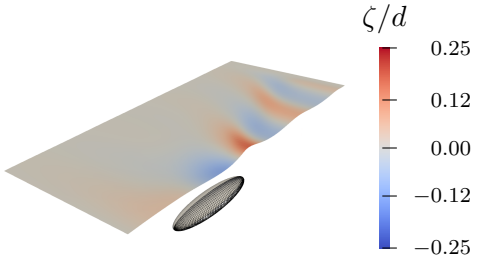

(a) $F_n = 0.4$

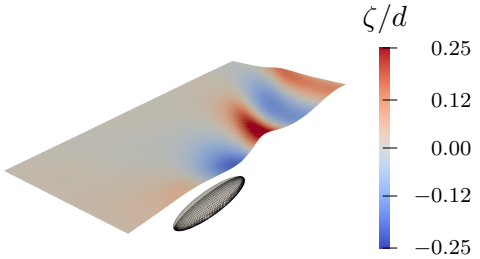

(b) $F_n = 0.5$

Figure 5.3.: Wave pattern due to a spheroid ($a/b = 4.5$, $d/c = 0.5$) travelling with forward speed under the free water surface considering two different Froude numbers F_n.

At the borders of the free surface domain the induced elevation and the induced potential are forced to be zero by the absorption factor ν_a, according to Section 3.2.3. Therefore, at each side of the mesh a spatial ramp is defined which increases the absorption factor from zero to one towards the border.

The resistance of the spheroid is determined by the integration of the hydrodynamic pressure which follows from Eq. (2.51). In Figure 5.3 the wave pattern produced by the traveling spheroid under the water surface for two different Froude numbers are shown. Here, the spheroid has the aspect ratio $a/b = 4.5$ and the immersion rate is $d/c = 0.5$. The induced waves for the two Froude numbers differ significantly. As expected, the induced waves at $F_n = 0.5$ are longer than in the case for $F_n = 0.4$. Furthermore, the wave amplitudes ζ for $F_n = 0.5$ are significantly increased which leads to a higher resistance, as shown in Figure 5.4.

Here, the computed resistance coefficient c_w is plotted against the Froude number for three different spheroid which vary regarding their aspect ratio a/b. A small aspect ratio stands for a relatively blunt spheroid whilst a high aspect ratio results in a slender geometry. The immersion rate is $d/c = 0.5$. The results of the present method are

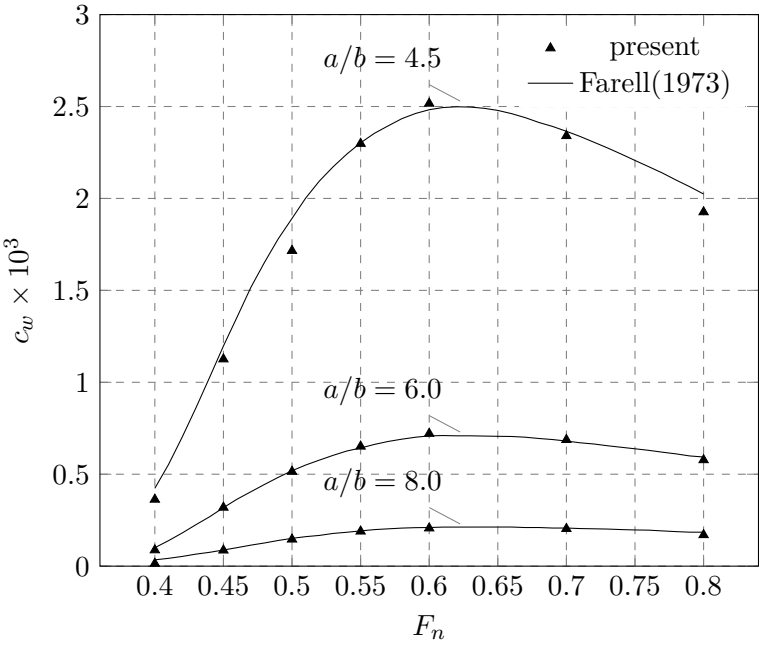

Figure 5.4.: Wave resistance coefficient c_w against the Froude number F_n for the immersion rate $d/c = 0.5$ and for different aspect ratios a/b.

compared with the results published by Farell (1973), who used a boundary element method with a source distribution on the body surface and with a linearized free surface boundary condition. The comparison shows that the results match very well for the slender geometries. Although, the resistance coefficient for the blunt spheroid ($a/b = 4.5$) differs for some Froude numbers as, for example, for $F_n = 0.5$. This difference could be related to the linearized free-surface condition used by Farell as it is only valid for very small wave amplitudes or steepness.

Diffraction and Radiation of Underwater Sphere

In the following, the hydrodynamic problem of an underwater sphere in waves is computed and the forces are validated. Here, the problem is subdivided into the diffraction and the radiation part which are investigated separately. The definition and the coordinate system are shown by the sketch in Figure 5.5. The radius of the sphere below the free surface is $a = 1$m and the immersion rate is $a/d = 1.5$. The phase velocity of the waves is denoted by c.

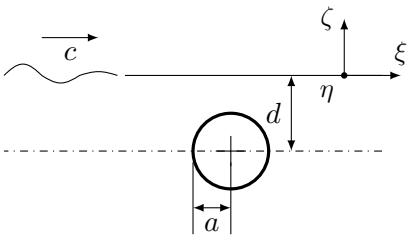

Figure 5.5.: Definition of the sphere under the free water surface excited by waves.

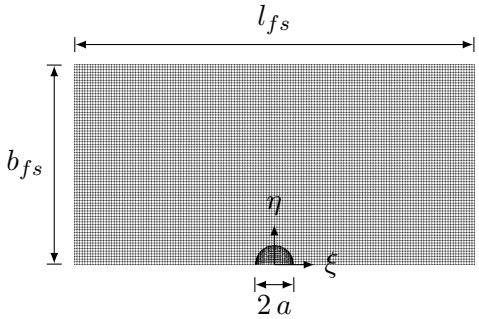

Figure 5.6.: Fine free surface grid for simulation of sphere below the free water surface.

Again, the symmetry condition is applied to reduce the total number of panels, see Fig. 5.6. Here, the grid of a half sphere is drawn below a fine free surface mesh. The discretization of the free surface grid is defined depending on the considered wavelength $\lambda_w = 2\,\pi/k$. A relatively high number of body panels ($N_b = 2500$) for the half of the sphere is applied to be able to describe the pressure distribution on the sphere accurate enough. Whilst the same grid resolution for the sphere is used for the simulation of the respective wave numbers, the free surface grid is adapted concerning the respective wavelengths, thus, each wavelength is discretized by at least 20 panels. Further, the size of the free surface grid is defined in the way, that it covers three wavelengths. A ramp is used to avoid wave reflections. Within this ramp the damping factor ν_d, see Eqs. (3.15) - (3.16), is increased from zero to one radiating outwards.

In contrast to the wave resistance problem, in this case the hydrodynamic loads on the sphere are unsteady. Instead, they are oscillating harmonically with the same frequency as the exciting waves. Concerning the simulation of the different wave numbers ka, the respective amplitude ζ_w is set in that way that the wave steepness is constant $H_w/\lambda = 0.04$ for the different cases. For each wave number ka five time periods T_w are simulated and the time step size is defined depending on the period as follows: $\Delta t = T_w/200$.

The results are compared with the results published by Lui et al. (2012). In the publication, Lui et al. used a higher-order boundary element method (HOBEM) developed by Teng and Taylor (1995). In this method a linear assumption for the free surface condition is applied, thus, the free water surface is not discretized by panels. Instead, the free surface condition is considered by a special formulation of Green's function, similarly used by frequency domain approaches. As mentioned, the problem is subdivided into two problems. First, the wave diffraction forces (f_x, f_z) are computed. The amplitudes of the oscillating forces are determined by a FFT and plotted in Figure 5.7 against the non-dimensional wave number ka. Here, the force amplitudes are divided by the wave amplitude ζ_w and the gravitational force $f_g = m_s\,g$, where $m_s = 4/3\,\pi\,\rho\,a^3$ is the mass

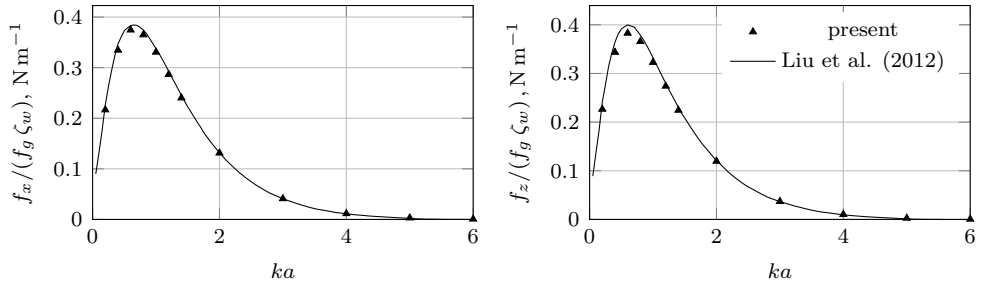

Figure 5.7.: Comparison of wave exciting forces on a sphere ($a/d = 1.5$) under the free water surface.

of the sphere. The comparison demonstrates that the results agree well with the results presented by Lui et al.

Furthermore, the hydrodynamic forces on the sphere due to its motion (radiation) are computed. Here, the sphere is forced to oscillate in horizontal and vertical direction. The two directions are simulated separately and the velocity u and acceleration a, which both are depending on the time, are respectively defined as follows:

$$u(t) = -\omega_m\,\zeta_m\,\cos(\omega_m\,t)\;, \tag{5.3}$$

$$a(t) = \;\omega_m^2\,\zeta_m\,\sin(\omega_m\,t)\;, \tag{5.4}$$

where ζ_m is the oscillation amplitude and $\omega_m = \sqrt{k\,g}$ denotes the oscillation frequency, in this case. The added mass and damping coefficients for surge (a_{11}, b_{11}) and heave (a_{33}, b_{33}) motion are determined from the time records of the computed forces. The added mass and the radiation damping terms can be distinguished by the phase information of the force as the two parts have a 90° phase shift relative to each other. The phase information is computed in a similar way as the force amplitude by the FFT. The added mass and damping terms are plotted against the non-dimensional wave number ka, see Fig. 5.8. Here, the coefficients are made dimensionless with the mass of the sphere m_s and the angular frequency of the oscillation ω_m. The plots show a very good agreement between the present method and the HOBEM regarding the added mass terms. Differences can be observed concerning the damping terms. The biggest differences are in the region of the peak of the respective curves. In fact, the damping terms are very sensible depending on the grid of the free water surface. The differences may also arise from the post processing as small errors in the evaluation of the phase information can lead to significant variation of the damping terms. Overall, the accordance is fairly good.

5.1.2. Monopile in Regular Waves

One major aspect in the simulation of the boat landing maneuver is the description of the hydrodynamic flow field around the monopile, where the catamaran is located.

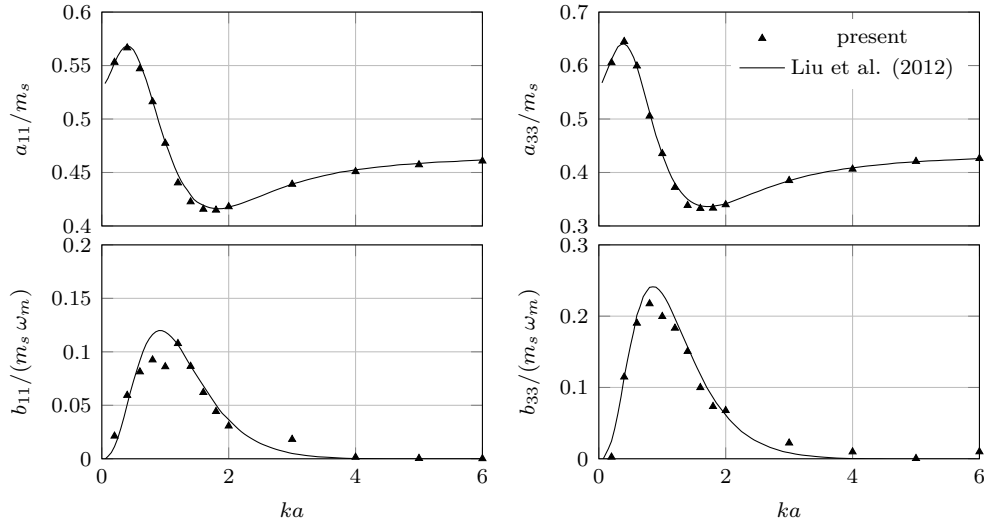

Figure 5.8.: Added mass and damping terms of a sphere under the free water surface for an immersion rate $d/a = 1.5$

Thus, to validate the developed numerical approach, the hydrodynamic problem of a surface-piercing cylinder in waves is simulated. First, the cylindrical foundation of an offshore structure is simulated in non-linear waves computing the hydrodynamic forces on the structure. This foundation has been experimentally tested already, see Krogstad and Stansberg (1995), and computed in several publication, e.g. Liu et al. (2001).

Here, the radius of the model scale cylinder is $R = 0.3125\,\mathrm{m}$ and the draft is $d = 3\,R$. The water depth is assumed to be infinite, and a fifth-order Stokes wave is introduced into the simulation by the wave potential which follows Eq. (2.50). As shown in Figure 5.9a, the panels of the free water surface are radially distributed around the foundation taking advantage of the symmetry condition. The mesh consists of $19 \times 15 = 931$ panels and covers a radius of $R_{\mathrm{fs}} \approx 15.5\,R$. The mesh of the cylinder is shown in Figure 5.9b. It is subdivided into a fixed bottom and an upper section. Latter part of the mesh deforms following the actual shape of the water line (WL) due to the waves. Here, the grid is spanned between vertical frames on the radius which has the initial height z_m in calm water. The bottom point of each frame is attached to the fixed grid whilst the top point of each frame is connected with a corner point of the adjacent free surface panels, thus it changes it length according to the free surface elevation at it position. The corner points of the body panels are distributed to these vertical frames and their vertical position according to the varying frame length.

A relatively small time step size is set according to the boundary that 800 steps per wave period T_w are considered. In Figure 5.10 the time history of the non-dimensional horizontal force $f_x/\rho g R^3$ on the cylinder for the non-dimensional wave number $kR = 0.22$ and a non-dimensional wave amplitude $kA = 0.133$ is plotted over the number of periods t/T compared with a MEL approach (HMEL) by Liu et al. (2001), which uses higher-

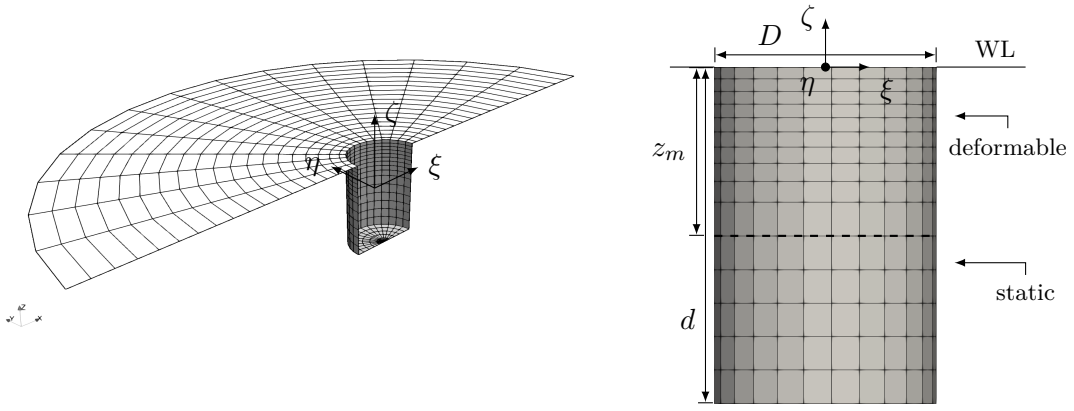

(a) Free surface grid **(b)** Cylinder grid

Figure 5.9.: Mesh of free water surface and of the standing cylinder in waves.

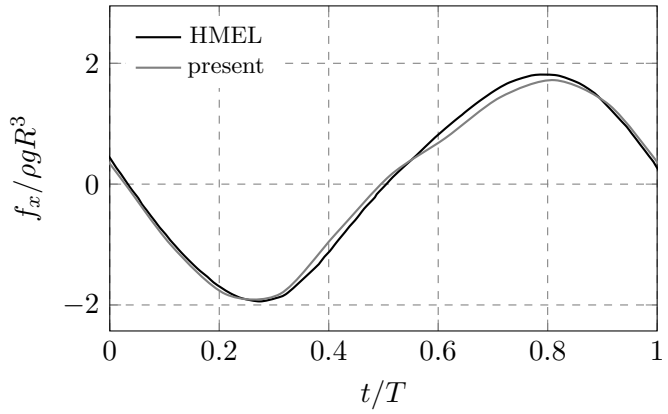

Figure 5.10.: Comparison of the horizontal force f_x plotted with respect to the time t over one encounter period T for the case $kR = 0.22$, $kA = 0.133$.

order panels. In general, the present results match fairly with the HMEL method, but the comparison of the curves indicates differences regarding the higher harmonics of the forces.

A better insight is provided by the comparison of the amplitudes of the harmonics which can be determined using a FFT. In this case, the first, second and third harmonic amplitudes $|f_x^{(1)}|$, $|f_x^{(2)}|$ and $|f_x^{(3)}|$ for the non-dimensional wave number $kR = 0.22$ and a wave amplitude $kA = 0.133$ are computed and documented in Table 5.1. Apart from this, the tank test results (Exp) by Krogstad and Stansberg (1995) are listed, furthermore, the results of three other numerical methods are given for validation. Here, the present results are compared with the higher-order panel method (HMEL) used in Liu et al. (2001), a second-order frequency-domain method for axis-symmetric problems (KY),

Table 5.1.: Validation of first, second and third harmonic amplitudes $|f_x^{(1)}|$, $|f_x^{(2)}|$ and $|f_x^{(3)}|$ of horizontal force on the cylinder for the non-dimensional wave number $kR = 0.22$ comparing the results with experimental measurements (Exp) and other numerical methods.

	$\lvert f^{(1)}\rvert / \left(\rho\, g\, R^3\right)$	$\lvert f^{(2)}\rvert / \left(\rho\, g\, R^3\right)$	$\lvert f^{(3)}\rvert k^3 / \left(\rho\, g\right))$
present	13.77	12.54	0.48
Exp	13.64	10.85	0.27
HMEL	13.41	12.97	0.33
KY	13.28	14.86	-
FNV	13.93	11.31	0.33

see M.-H. Kim and D. K. P. Yue (1989), and a small-body asymptotic theory in the frequency domain by O. Faltinsen et al. (1995).

According to the results in Table 5.1, the computed forces computed by present approach match well with the experiments and the other methods regarding the first harmonic amplitude $|f^{(1)}|$. In contrast to this, the second harmonic force amplitude $|f^{(2)}|$ varies from the experiments but also the results of the other methods differ, and they are in the same range of the result delivered by the developed method. However, the third harmonic force amplitude computed by the present approach is significantly overestimated compared with the other methods. The inaccuracy regarding to the third harmonic force amplitude may be due to the low-order characteristic of the used free surface panels. Probably, a better solution would be the use of higher-order panels like done by Liu et al. (2001). Then, the potential and the induced velocities would be known directly from the solution of the boundary value problem and the higher-order effects could be determined more precisely.

In general, the results indicate that the developed free surface model in *pan*MARE is suitable to compute the hydrodynamic forces on a cylinder in waves with a fair accuracy. Although, concerning the boat landing maneuver of the catamaran, much more important than the forces on the monopile is the determination of its influence on the fluid field due to the diffraction effects. Therefore, the cylinder in regular waves is simulated focusing on the surface elevation in the circumstance of the cylinder and comparing the output with the experimental results which were presented in Section 4.2. Figure 5.11 shows the surface plots of the simulated water elevation in comparison with the tank tests (Exp) for a regular wave ($H_w = 0.05\,\mathrm{m}$, $\omega_w = 5\,\mathrm{rad\,s^{-1}}$) which travels in positive x direction and passes the cylinder $R = 0.25\,\mathrm{m}$. Here, four different instances of time defined by the phase φ are considered. In each subfigure, the experimental results are plotted on the left-hand side. In the middle graph, the water surface which follows from the cylinder diffraction potential defined by Eq. (2.38) is plotted and on the right-hand side the water surface computed by the non-linear free surface model (BEM) is illustrated. Although, the outcome of both approaches is similar and seems to be suitable

to describe the diffraction around a cylinder, the comparison indicate that the solution of the free surface model delivers a more precise description of the wave field than the linear solution of the cylinder diffraction compared with the experiments.

5.1.3. Wigley Hull in Waves

In the following, two Wigley models with forward speed are simulated and the numerical results are compared with tank tests by Kashiwagi (2013). The shapes of the two models are described by the following equation:

$$y = \left(1 - z^2\right)\left(1 - x^2\right)\left(c_0 + c_2\, x^2 + c_4\, x^4\right) + z^2\,\left(1 - z^8\right)\left(1 - x^2\right)^4\,, \tag{5.5}$$

where $x = \xi/\left(L/2\right)$, $y = \eta/\left(B/2\right)$ and $z = \zeta/d$. Here, L is the ship length and B denotes the breadth. Further, c_0, c_2 and c_4 are geometry parameters which are different for the two ship geometries. The hulls vary regarding their main dimensions and their block coefficient c_b. Therefore, in the following, the two hulls are denoted as *blunt* and *slender* model, respectively. The main dimensions are listed in Table 5.2 as well as the respective coefficients c_0, c_2 and c_4 for Eq. (5.5).

The same setup is used for creating the mesh of the two different models and the associated free surface grids. Here, the knots of the hull mesh are distributed on the hull frames which are located at discrete x_l-positions. Following to the procedure for the treatment of the intersection line between body and free surface grid in Section 3.2.2, the frames are described by curves which are defined by Eq. (5.5), where $x = x_l$, thus: $y_l(z) = y(x = x_l, z)$. In Figure 5.12, an example mesh for the simulation of the *blunt* Wigley model is illustrated. Here, the hull is meshed by $47 \times 10 = 470$ panels whilst the free surface is composed of $143 \times 30 = 4290$ panels.

Table 5.2.: Main dimensions and coefficients for surface description of Wigley models applied in tank tests by Kashiwagi (2013).

Model Type			*slender*	*blunt*		*slender*	*blunt*
Length	L	m	2.0	2.5	Coefficients		
Breadth	B	m	0.3	0.5	related to Eq. (5.5)		
Draft	d	m	0.125	0.175	c_0	1.0	1.0
Displacement	∇	m^3	0.04205	0.13877	c_2	0.6	0.2
Waterline area	A_{wl}	m^2	0.416	1.005	c_4	1.0	0.0
Radius of gyration	$k_{\eta\eta}$	m	0.496	0.590			
Vertical position of cog	ζ_{cog}	m	-0.0404	-0.03			

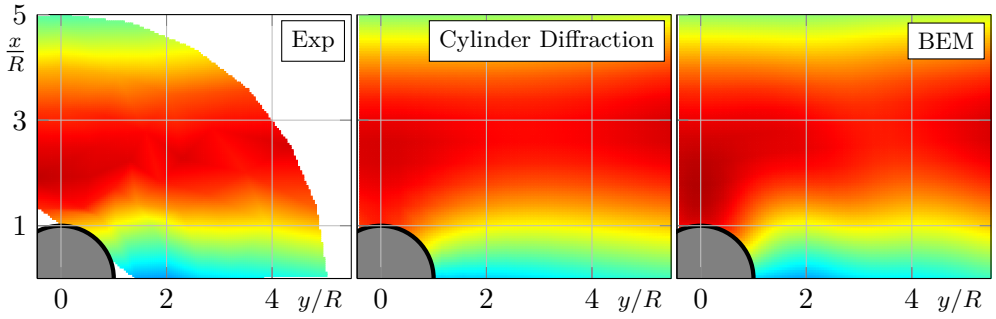

(a) $\varphi = \frac{1}{2}\,\pi$

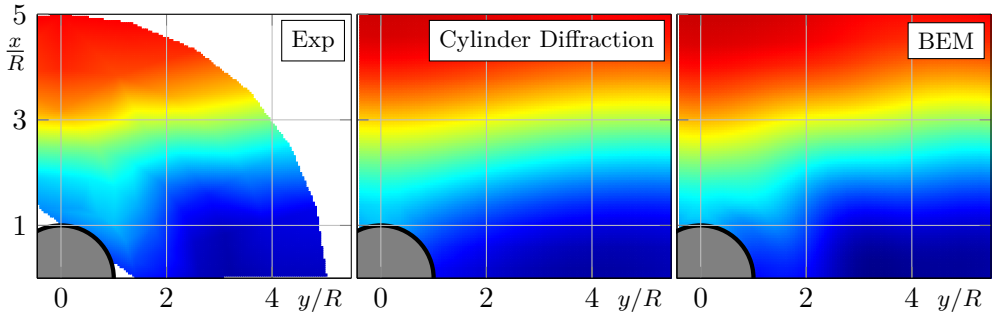

(b) $\varphi = \pi$

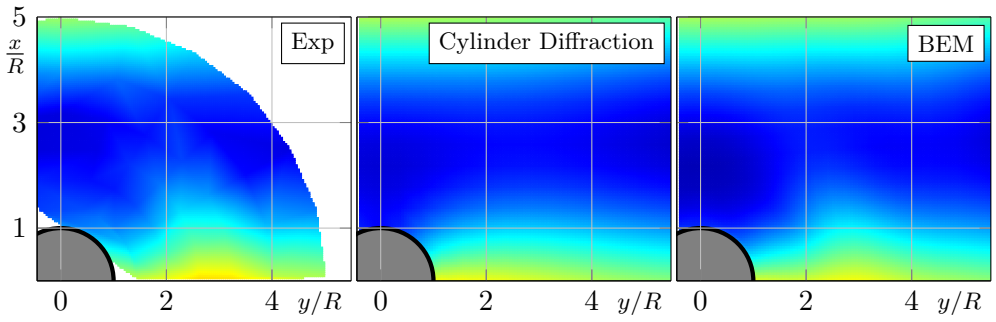

(c) $\varphi = \frac{3}{2}\,\pi$

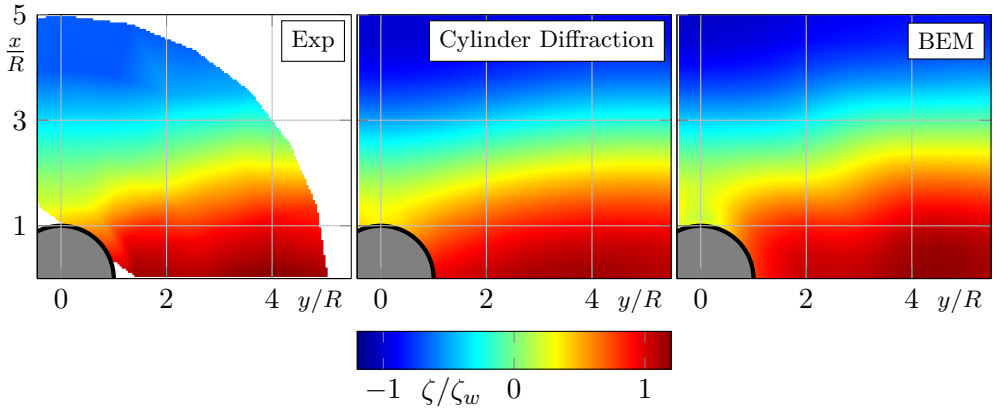

(d) $\varphi = 2\,\pi$

Figure 5.11.: Comparison of simulated water surface elevation in the circumstance of the cylinder in regular waves ($H_w = 0.05\,\mathrm{m}$, $\omega_w = 5\,\mathrm{rad\,s^{-1}}$) with results from the experiments for four different phases.

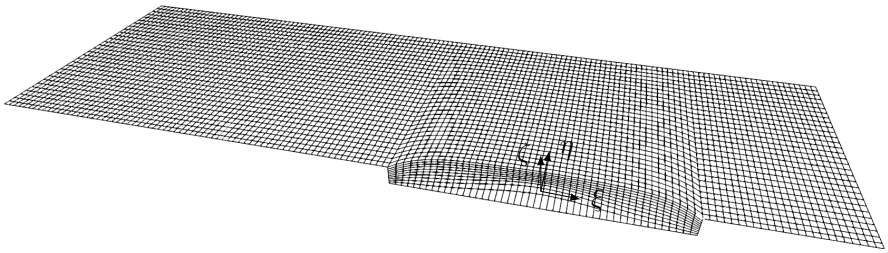

Figure 5.12.: Mesh of the free surface and the blunt Wigley hull for a wavelength $\lambda/L = 0.8$.

In the simulations, the Wigley models are moving forward with a constant Froude number $F_n = 0.2$. In the first stage, the models are constrained to stay fix in the other degrees of motion, in order to initially focus on the excitation forces of the waves and the diffraction without taking into account the radiation due to free ship motion. The length of the waves which are encountering the models from ahead ($\mu = \pi$) is varied between 1 m to 5 m. Here, the linear wave potential according to Eq. (2.30) is applied to describe the hydrodynamic properties of the wave. Related to this, the distance $\bar{\xi}$ from Eq. (2.31) is updated in every time step, so that it is considered that the vessel is moving forward. Following the experiments by Kashiwagi (2013), the considered wave heights are $H_{w,\mathrm{bl}} = 0.06\,\mathrm{m}$ for the *blunt* model and $H_{w,\mathrm{sl}} = 0.05\,\mathrm{m}$ for the *slender* hull. However, for both hulls the wave height is decreased for short wavelengths to satisfy the relation $H_w/\lambda \leq 1/30$, thus, steep waves are avoided. At the beginning of each simulation, the incoming waves are omitted until the wave pattern due to the forward speed of the ship are fully developed and the hydrodynamic forces are converged. Then, the waves are introduced by a time ramp which increases the wave height H_w from zero to the target value.

In Figure 5.14, the response amplitude operators of the forces in surge and heave direction and for the pitch moment are plotted against the non-dimensional wavelength λ/L for both models. Furthermore, the corresponding phase information of the respective forces and of the moment are plotted in the lower graphs. The forces and the moment are made non-dimensional by the water density ρ, the gravity constant g, the wave amplitude ζ_w, the breadth B, and the length L of the respective Wigley hull. Within the graphs, the triangles (present) denote the numerical results, they are compared with the experimental data (Exp) published by Kashiwagi (2013), which are represented by the black circles. The comparison shows for both models and over the whole range of considered wavelengths a very good agreement. It indicates that the method is able to compute the hydrodynamic forces of a body which is traveling through a wave field in an accurate manner. The good agreement regarding the phase information further demonstrates that beside of the Froude-Krylov forces also the diffraction part of the hydrodynamic loads is computed accurately.

In Figure 5.13, the hydrodynamic heave force and pitch moment are plotted against the number of encounter periods t/T_e for two different non-dimensional wavelengths λ_w/L

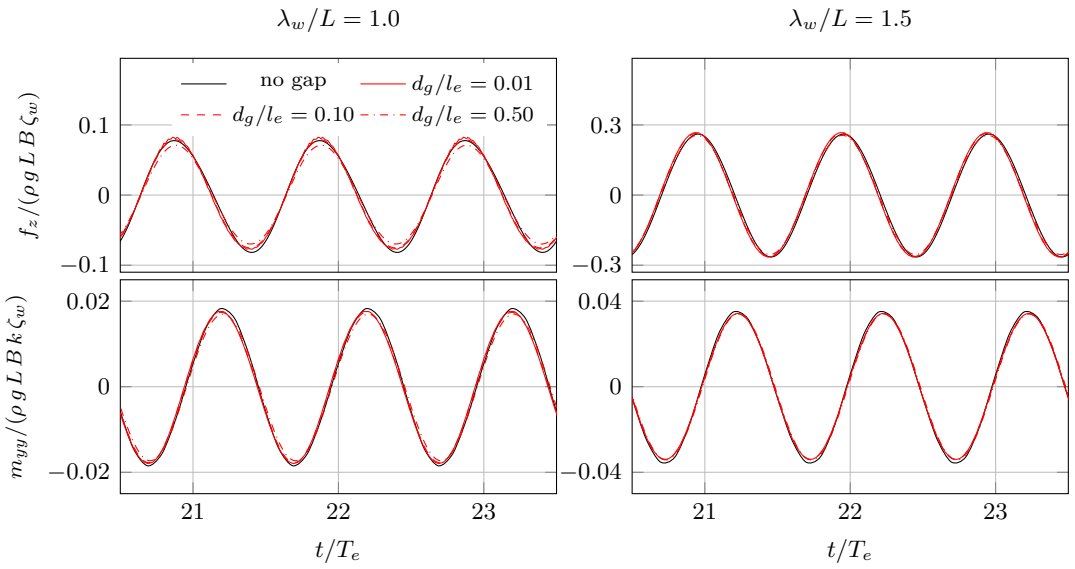

Figure 5.13.: Comparison of hydrodynamic heave force and pitch moment of a Wigley hull with forward speed in waves applying different gap size between free surface and body grid.

comparing the two different numerical treatments of the body-free surface intersection in Section 3.2.2. Here, the solid black line (no gap) denotes the simulation results applying a direct connection between free surface and body mesh. Beside of this, the gray lines define simulation results using instead a cut-out of the free surface. Following the procedure described in Section 3.2.2, a small gap is left between free surface and body mesh. Here, the gap width d_g is made non-dimensional using the edge length l_e of the adjacent panel. The plots demonstrate that for both regarded wavelengths the results obtained using different gap sizes $d_g/l_e \leq 0.1$ almost equal to the procedure with the direct connection (no gap). Bigger gaps lead to higher differences, in particular, concerning the heave motion for the wavelength $\lambda_w/L = 1.0$.

Free Motion in Head Waves

In the next step, the *slender* Wigley model is numerically analyzed considering the free motion in waves. Again, the model is moving forward with constant speed ($F_n = 0.2$) but in this case the model is allowed to freely move in heave and pitch direction. In contrast to the experiments, the surge motion is still constrained. According to the results of the experimental study in Kashiwagi (2013), the surge motion is small, therefore it is expected that the error due to the constraint does not influence the motion in the degrees of freedom heave and pitch significantly. In the numerical simulation, an artificial damping is included to correct the error due to the missing viscous effects, which have an influence on the motion behavior but are not covered by potential theory. The additional

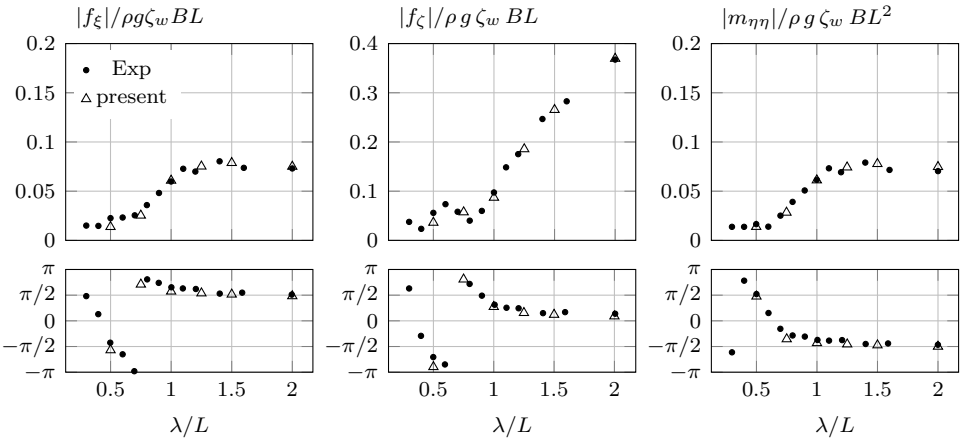

(a) *Slender* model

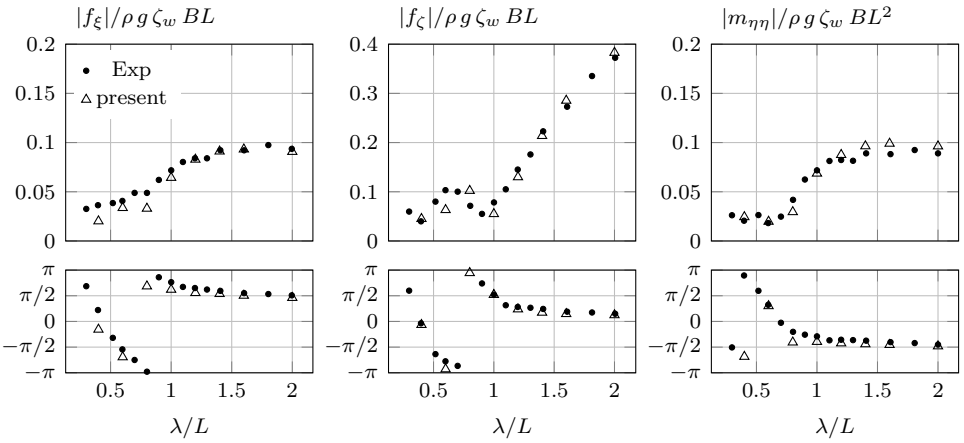

(b) *Blunt* model

Figure 5.14.: Comparison of the response amplitude operators of the forces in surge and heave direction and the pitch moment of Wigley models in head waves ($F_n = 0.2, \mu = \pi$) with experiments published by Kashiwagi (2013).

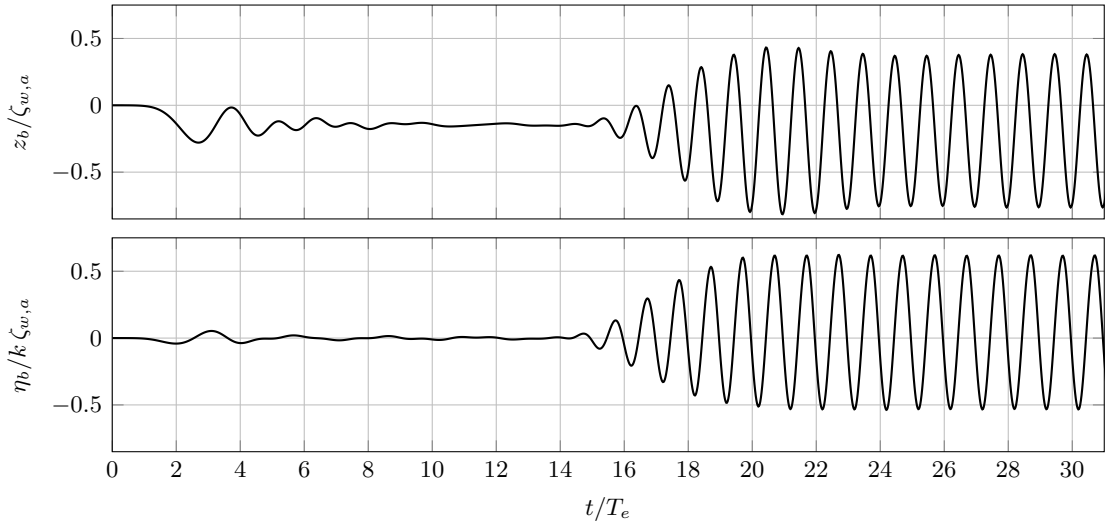

Figure 5.15.: Time record of the heave and pitch motion of the *slender* Wigley hull with forward speed in head waves ($F_n = 0.2$, $H_w = 0.05\,\mathrm{m}$, $\lambda/L = 1$).

damping is included using linear terms and constant damping coefficients d_ζ and d_η for the heave and pitch motion, respectively. The damping coefficients are approximately estimated to be 5 % of the respective critical damping.

In Figure 5.15, the non-dimensional heave $z_b/\zeta_{w,a}$ and pitch $\eta_b/k\zeta_{w,a}$ of the *slender* Wigley hull are plotted against the number of encounter periods t/T_e. Following the procedure of the simulations with the fixed models, the incoming waves are not considered at the beginning of the simulation but are introduced after the hydrodynamic forces converged and the hull found an equilibrium position. Regarding the plots, the Wigley hull acquire dynamic sinkage whilst the trim almost stays at zero degree. Furthermore, the plots indicate that the model achieves a new equilibrium position after approximately $t/T_e = 10$. The ramp which introduces the head waves starts at $t/T_e = 15$ and increases the wave height until it is fully developed ($t/T_e = 20$). According to the plots, the heave and pitch motion converge fast to harmonic oscillations after the total wave height H_w is reached.

In Figure 5.16, the response amplitude operators for the heave and pitch motion of the *slender* Wigley model z_b and η_b are plotted against the non-dimensional wavelength λ/L. Again, the numerical results are denoted by the triangles (present) whilst the experimental data from Kashiwagi (2013) are marked by the black circles (Exp). The comparison shows a good agreement, except of the heave motion in the circumstance of the resonance $1.0 \leq \lambda/L \leq 1.5$ where the numerical results overestimate the amplitudes in comparison of the validation data. Concerning the pitch motion, it can be stated that the results from the simulation match fairly well the validation data, but at the resonance the results differ slightly. With regard of the very good agreement concerning the response amplitude operators for the fixed models, the validation indicates that

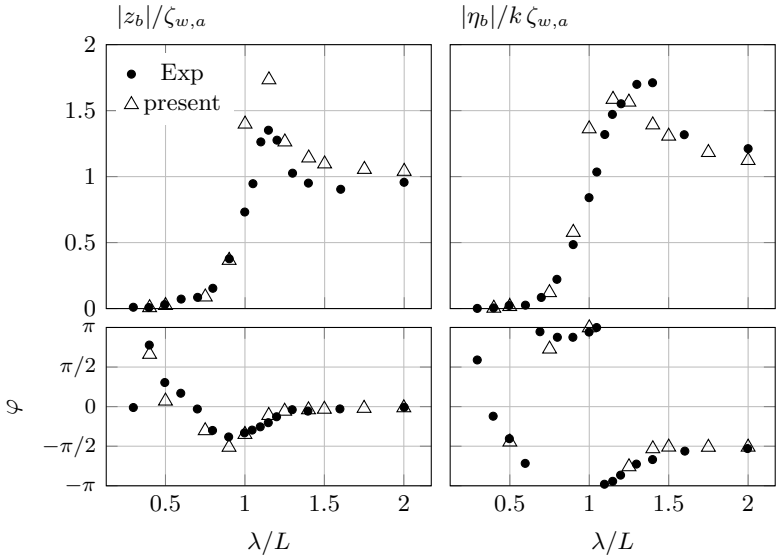

Figure 5.16.: Comparison of motion response amplitude operator of *slender* Wigley model in head waves ($F_n = 0.2, \mu = \pi$) with experiments published by Kashiwagi Kashiwagi 2013.

the differences near the resonance may be caused by an inaccurate description of the radiation damping. Considering, that the hydrodynamic loads due to radiation are significantly influenced by the radiating waves, which arise at the ship hull, it can be assumed, that the inaccuracy probably is caused by the approximated solution of the potential at the intersection line between free surface and hull. It is expected that the results could be improved by solving the velocity potential directly at the intersection between free surface and body. This would be possible by using higher-order panels, for example.

5.2. Boat-Landing Maneuver

This section deals with the simulation of the boat-landing maneuver in regular and irregular waves. The numerical boat-landing maneuvers are carried out considering the contact model which is introduced in Section 3.4 and the free surface model described in Section 3.2. Here, the behavior of the two catamaran models related to the experimental investigation, see Section 4.3.3, are analyzed. First, the catamaran *Model 1* is tested in regular waves comparing the response amplitude operators with the tank test results. Then, the boat-landing maneuver of catamaran *Model 2* is simulated in regular and irregular waves, to further verify and validate the developed method regarding the computed vessel motion and the prediction of situations in which the fender slips.

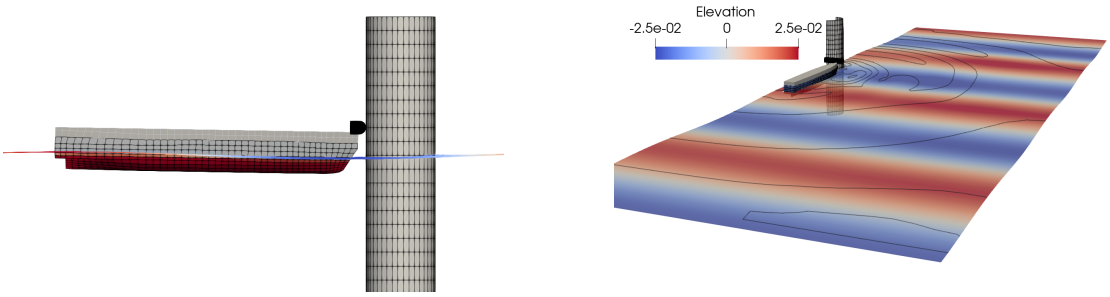

Figure 5.17.: Simulation of boat-landing maneuver of catamaran *Model 1* in regular waves ($H_w = 0.05\,\mathrm{m}$, $\lambda/L = 4$).

5.2.1. Catamaran Motion in Regular Waves

First, the motion behavior of the catamaran *Model 1* is numerically investigated in regular waves. The main dimensions of the model follow the data from the experiments, see Table 4.2. With respect to the experimental investigation, see Section 4.3, here, the motion of catamaran is analyzed for the case the vessel either is pushing against the monopile or freely moving. Only one catamaran hull is discretized because the problem is symmetrical. The free surface grid spans an area of $5\,\mathrm{m} \times 14\,\mathrm{m} = 70\,\mathrm{m}^2$ and consists of $N_{\mathrm{fs}} = 4325$ panels. For the catamaran hull $N_{\mathrm{cat}} = 1070$ panels are used. The grid of the catamaran is not connected with the free surface, instead, it is moving within a cut-out of the free surface grid, as introduced in Section 3.2.2. Furthermore, the grids for the free surface and the catamaran are derived using an external mesh tool and then imported into *pan*MARE whilst the cylinder is generated by the implemented meshing tool.

On the left-hand side, Figure 5.17 shows the mesh of the catamaran *Model 1* and the monopile. On the right-hand side, the free surface elevation is shown during the simulation of the boat-landing in regular waves. In the case that the catamaran is in contact with the monopile, the fender is constraint, thus, it stays fixed and no slip occurs. The time step size is set depending on the wavelength, computing 100 steps per wave period.

In Figure 5.18, the resulting response amplitude operators of the catamaran, which is either in contact or freely moving (present), are plotted against the non-dimensional wavelength λ/L, and compared with the experimental results (Exp) for the heave and the pitch motion. The comparison indicates that the numerical results match the experiments well concerning the motion without contact. Slight differences can be observed regarding the heave motion in short waves. In the case that the catamaran is in contact with the monopile, the simulation overestimates the heave motion in the range $\lambda/L = 2to4$ whilst the pitch motion match slightly better. Furthermore, regarding the experimental results a local maximum $\lambda/L = 1.82$ can be observed, which is not reproduced in the simulation.

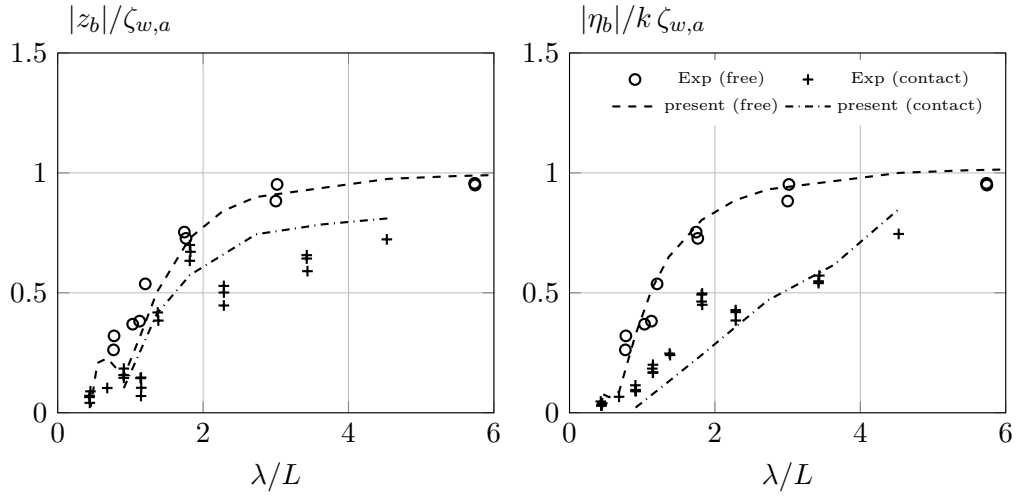

Figure 5.18.: Response amplitude operators of heave and pitch motion of catamaran *Model 1*, which is either freely moving (free) or in contact with the monopile (contact), compared with experimental results (Exp).

5.2.2. Verification of Fender Behavior During Boat-Landing Maneuver in Regular Waves

So far, concerning the catamaran in contact with the monopile, the fender was constrained to stay fixed at the boat-landing structure, thus, it could not start to slip along the monopile surface. In the following case, the catamaran is simulated during it is pushing against the monopile again, but, in contrast to the previous computations, here, the fender is allowed to slip. The following results are used to verify the developed contact model considering the ability to distinguish between stick- and slip-condition and to handle the non-linear behavior of the friction forces.

Here, a comparison of the forces and the vertical displacement of the fender at the boat-landing structure for two different wavelengths is shown in Figure 5.19. Here, the top graphs denote the time ranges in which the fender stays fixed (stick-condition) or displaces (slip-condition). In the graphs below the stick-condition is further indicated by the gray shaded domains. On the left-hand side, the plots show the results of a catamaran in waves for the non-dimensional wavelength $\lambda_w/L = 0.682$ and on the right-hand side it is $\lambda_w/L = 1.818$.

According to the plots on the left-hand side for the short wavelength $\lambda_w/L = 0.682$, after a short period of time, in which the catamaran starts to push the fender against the structure, the fender stays stick over the remaining time range of the simulation ($\dot{z}_\mathrm{f} = 0$). Due to this, the fender forces in normal direction f_f^n and the friction force f_f^fr harmonically oscillate with the encounter period T_e. In contrast to this, following the plots on the right-hand side, in the second case ($\lambda_w/L = 0.682$) the fender starts to slip

after one encounter period and permanently varies its vertical position. According to the vertical displacement Δz_f, each time the fender reaches the lowest position it rests at this position for a moment before it starts to slip upwards again. The plot of the friction force f_f^fr indicates a strong non-linear behavior which also applies on the vertical acceleration $\ddot{z}_\mathrm{cp}$. The comparison shows reasonable results of the fender behavior during the boat-landing maneuver. It demonstrates that the contact model can describe handle not only situation in which the fender is sticking at the boat-landing surface but also during the occurrence of slip.

5.2.3. Landing Maneuver in Irregular Waves

In the following, the boat-landing maneuver of the catamaran *Model 2* is simulated in irregular waves and validated by comparing the simulation results with the tank test measurements presented in Section 4.3.3. The main dimensions of the catamaran are according to the data of the experimental model, see Tab. 4.2. Here, the maneuver is simulated in three different sea ways which are all defined by a JONSWAP spectra but with different parameters. They are listed in Table 5.3.

In general, natural seaways are assumed to be stochastic processes and, therefore, also sea keeping problems in irregular waves are often investigated applying stochastic analyses. In order to compute statistical properties like the significant amplitudes and probabilities, long-term data series would be needed for the thorough validation of the numerical method. In fact, this means a high amount of computational effort on the numerical side but as well the time-series of the experimental data for the validation need to be long enough.

However, instead of compute long-time series for the prediction of probabilities, the simulation of the boat-landing maneuver can be validated by directly comparing the time records. For this purpose, the waves measured in the experiments must be reproduced in the simulation. Here, a fast Fourier-transformation is applied on the time record of the wave measurements. As a result, the elevation over the time is separated into linear waves of different amplitudes, lengths, and phases. Based on this data, a finite number of linear Airy waves are input into the simulation environment to describe the same wave conditions as in the experiments. In this certain case, the validation by comparing the results in the time domain has the advantage, that not only the probability of slip occurrence is validated but also the ability to forecast the instance of time when the fender potentially starts to slip.

The simulation of the landing maneuver in irregular waves are computed in the same model scale as the experiments. The same computational mesh is applied for the different sea states. According to the previous simulations, the grid for the free surface spans an area of $14\,\mathrm{m} \times 5\,\mathrm{m} = 70\,\mathrm{m}^2$ and is generated by using an external mesh tool. The grid is displayed on the left-hand side in Figure 5.20. On the right-hand side, the grid for the catamaran and the cylinder are shown from the side view. Within the simulations, for

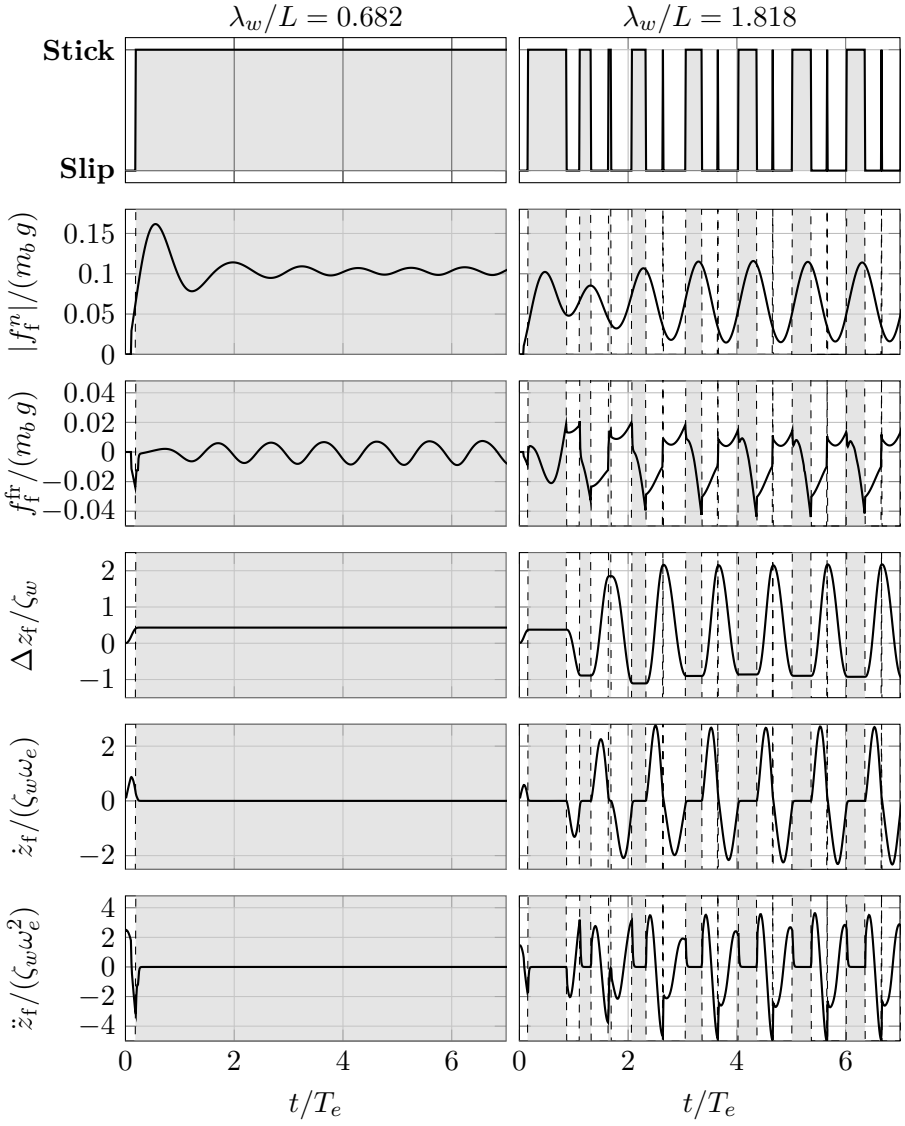

Figure 5.19.: Comparison of the behavior of the fender contact in regular waves ($H_w = 0.05\,\mathrm{m}$). Plotted within the graphs (from top to bottom): Stick-Slip Condition, the normal and friction force at the fender f_f^n and f_f^fr, the vertical displacement Δz_f and the vertical velocity and acceleration of the fender $\dot{z}_\mathrm{f}$ and $\ddot{z}_\mathrm{f}$.

Table 5.3.: Parameters of JONSWAP wave spectra which are considered for the simulation of boat-landing maneuvers in irregular waves.

No.	Peak freq. ω_p, rad s^{-1}	Sign. height H_s, m	Encounter angle ν, °
J01	3.31	0.125	0.0
J02	4.44	0.125	0.0
J03	4.97	0.100	0.0
J04	4.97	0.100	15.0

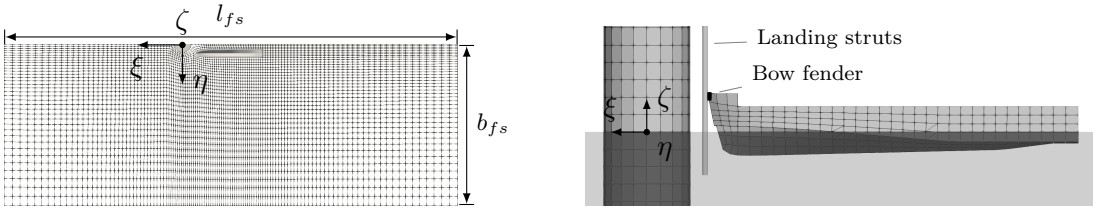

(a) Mesh of free water surface from top view. **(b)** Side view on body meshes.

Figure 5.20.: Computational meshes for boat-landing maneuver simulation.

the free surface $N_{\text{fs}} = 4405$ panels are used. The number of panels for the catamaran and for the cylinder are $N_{\text{cat}} = 463$ and $N_{\text{cyl}} = 500$, respectively.

In Table 5.4 the properties of the fender model are summarized which have been tested to be appropriate for the boat-landing maneuver that are presented in the following. The time step size Δt in the simulations is set depending on the peak period T_p of the respective JONSWAP spectrum as follows: $\Delta t = T_p/100$. Figure 5.21 illustrates the simulation of the catamaran during the boat-landing maneuver in irregular waves. On the left-hand side the encountering waves are shown. Here, the encounter angle is $\nu = 15°$. As the problem in this case is asymmetric the whole domain is discretized.

Exemplary, the results of the boat-landing simulation in two different sea states are shown and discussed in the following. Further results are documented in Appendix A.2. First, the catamaran is simulated in irregular waves which are defined by the sea state J03 from Table 5.3 ($H_s = 0.10\,\text{m}$, $\omega_p = 4.97\,\text{rad s}^{-1}$, $\nu_w = 0°$), are presented in Figure 5.22.

Table 5.4.: Properties of the fender model used within the boat-landing maneuver simulation.

Friction coeff.				Stribeck parameter			
kinematic	μ_k	-	0.7	Viscousity const.	k_v	-	0.2
static	μ_s	-	0.9	Exponential coeff.	δ	-	1.5
Spring-damper				Reference vel.	v_{ref}	m s^{-1}	0.2
Spring constant	c_{f}	kN m^{-1}	0.5				
Damper constant	d_{f}	kN s m^{-1}	0.25				

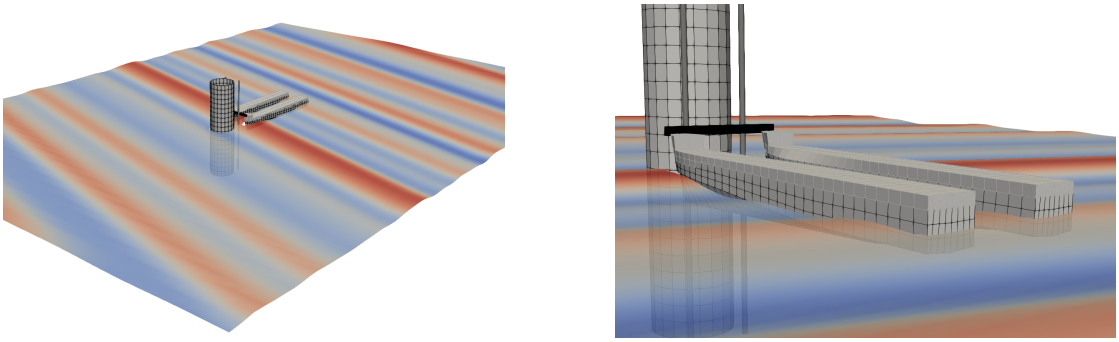

Figure 5.21.: Simulation of the boat-landing maneuver of the catamaran *Model 2* in irregular waves ($H_s = 0.125\,\mathrm{m}, \omega = 4.44\,\mathrm{rad\,s^{-1}}$, $\nu = 15°$).

The computations (present) are compared with the experiments (Exp), which are referred to Section 4.3.3.

The top graph in Figure 5.22a shows the wave elevation ζ_w. The reference point, where the waves are defined within the simulation, is at the same position as the wave gauge in the experiments, see Fig. 4.13. Here, the graphs demonstrates that the change of the surface elevation over the time computed in the simulation (present) match well the measurements from the tank tests. As already mentioned, the waves from the experiments are described in the simulation by a sum of linear waves of different lengths. The parameters of the linear waves are derived by a FFT from the experimental data. Nevertheless, according to the plot, the elevation curve slightly differs from the experimental results because not the complete data from the FFT but a finite number of waves are introduced. Instead, only the twenty most dominating wave parts from the FFT are considered in the simulation to reduce the computational effort. It is expected that the error for the catamaran motion due to the slight differences regarding the description of waves is relatively small.

The two bottom graphs in Figure 5.22a respectively show the computed heave and pitch motion of the catamaran ζ_b, η_b over the time t in comparison with the results from the tank tests. In general, the plots indicate a fair agreement but, concerning the pitch motion η_b, after the time $t \approx 15\,\mathrm{s}$ a difference between computation and experiments, which is almost constant over the time, can be observed. This offset is related to the slip motion of the fender and its elevated rest position which the fender takes after its displacement.

In Figure 5.22b, the two top graphs show the vertical fender displacement and the velocity, the two bottom graphs compare the horizontal and vertical fender forces F_h and F_v, respectively. According to the top graph, in which the elevation of the fender is plotted, the elevated position, at which the fender sticks after the displacement, differs between simulation and experimental results. Although, the comparison of the vertical motion of the fender shows that in both, the experiments and the simulation, the fender

slip occurs at the same instant of time and the fender behaves very similar during the slipping. First, it starts to displace upward, and it moves downwards again after reaching a maximum. The comparison shows that the computed maximum displacement is underestimated in comparison with the experiments.

In the second presented validation case, the boat-landing maneuver of the catamaran *Model 2* is simulated for the sea state J04. Here, the irregular waves ($H_s = 0.1\,\mathrm{m}$, $\omega_w = 4.97\,\mathrm{rad\,s^{-1}}$) are encountering the monopile and the catamaran under the angle $\nu_w = 15°$. The simulated motion of the catamaran is shown in Figure 5.23a. Here, the elevation ζ_b, the roll motion φ_b, and the pitch motion η_b are compared with the corresponding measurement data. In contrast to the previous symmetrical cases, here, the vessel is additionally free to roll. However, the roll motions are constraint by the friction of the fender at the two boat-landing struts. Here, the time record of the simulated roll motion differs from the experiments in which small roll motions can be observed during the whole measurement. Probably, this is due to the low stiffness of the fender material in the experiments which slightly deform and thus allow the catamaran to roll even if the fender stick at the struts.

Furthermore, the simulation results of the test cases J01 and J02 are presented in the Appendix A.2, see Fig. A.2 – Fig. A.3. The comparisons with the tank tests show a fair agreement. Although, the vertical displacement of the fender is not represented exactly in the simulation, the validation proves that the approach can forecast the dangerous situations when the fender starts to slip. Thus, it can be concluded that the developed numerical approach is able to simulate the boat-landing maneuver in an appropriate manner. The greatest possibility of improvements could be related to the propeller thrust and its hydrodynamic interaction effects with the hull and the incoming waves.

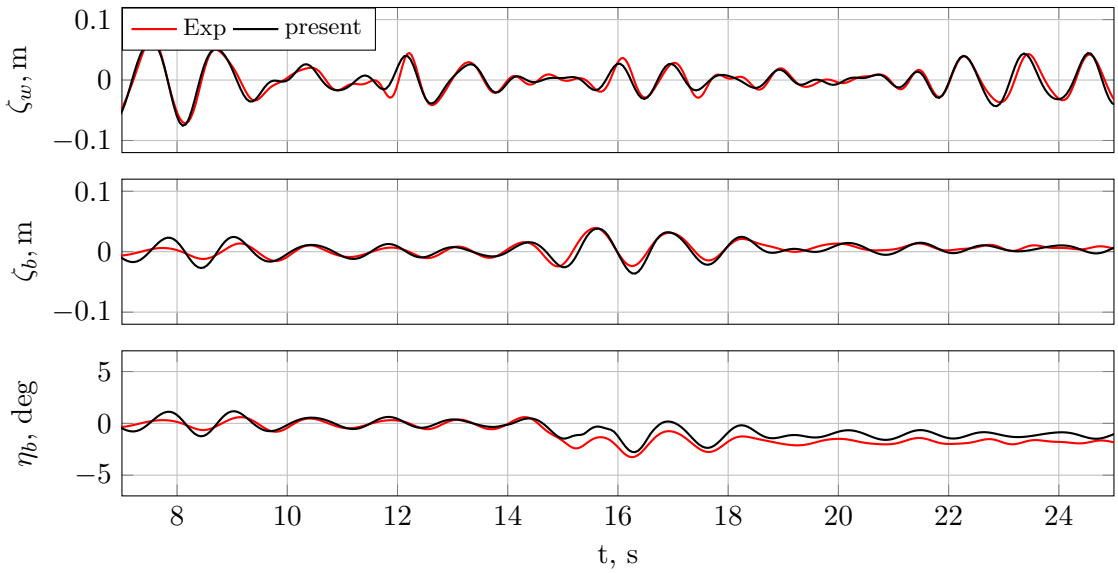

(a) Wave elevation ζ_w, heave motion ζ_b and pitch motion η_b of the catamaran model.

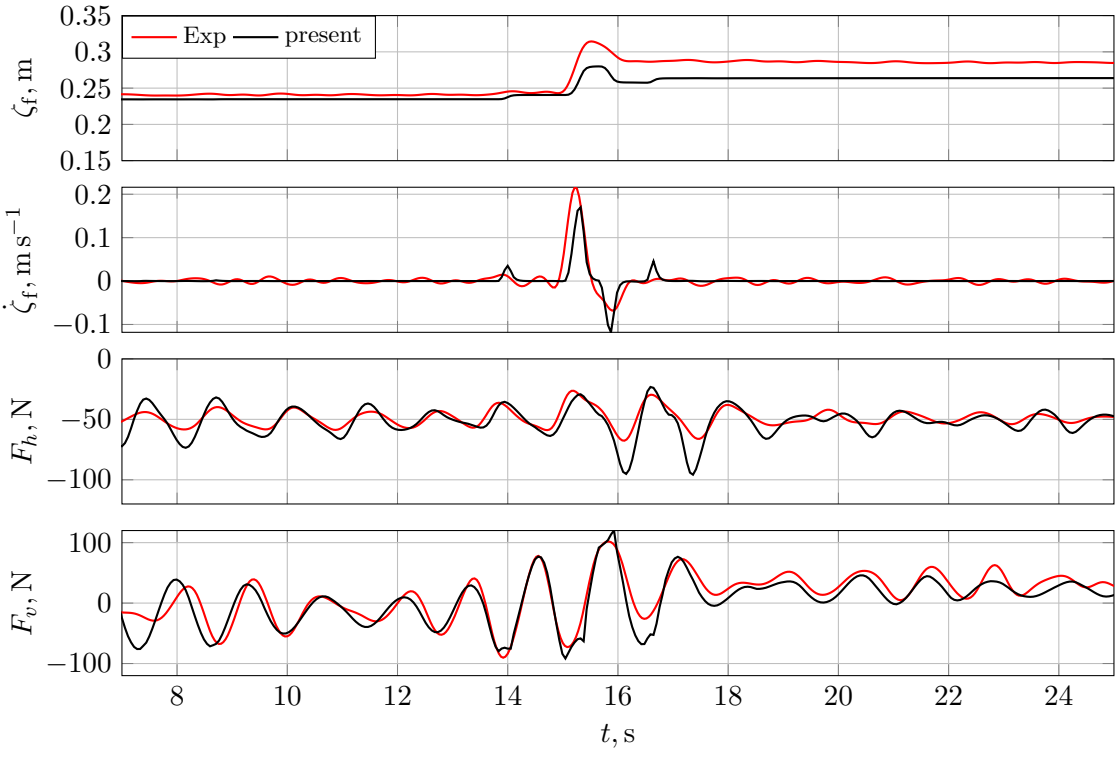

(b) Vertical fender displacement ζ_f and velocity $\dot{\zeta}_f$, horizontal F_h and vertical force F_v at fender.

Figure 5.22.: Comparison of the boat-landing maneuver simulation (present) of the catamaran *Model 2* in irregular waves (J03: $H_s = 0.10\,\mathrm{m}$, $\omega_p = 4.97\,\mathrm{rad\,s^{-1}}$, $\nu_w = 0°$) with experiments (Exp).

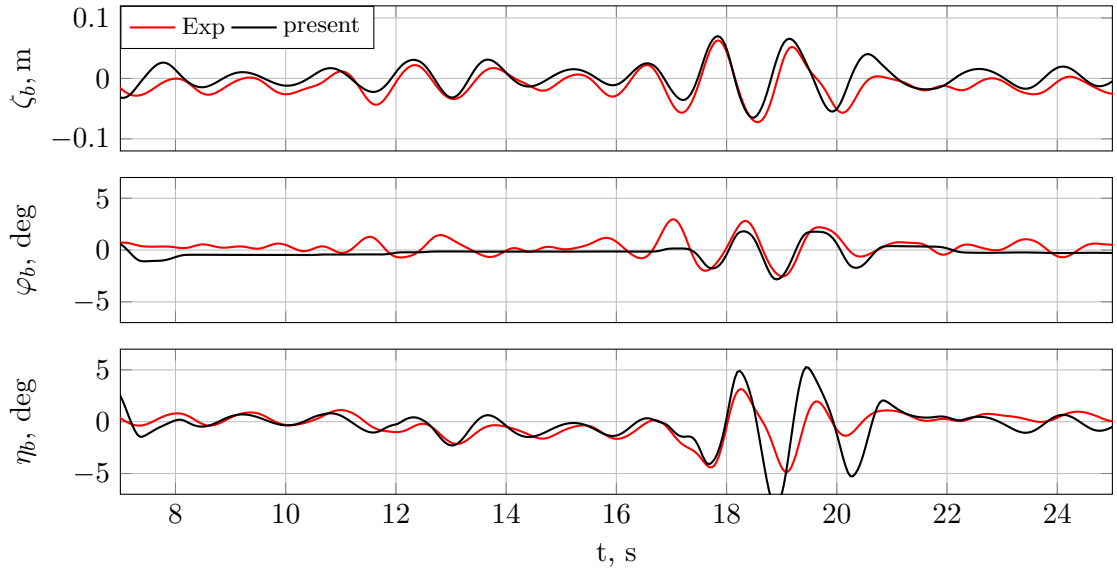

(a) Motion of the catamaran model in heave ζ_b, roll φ_b and pitch η_b.

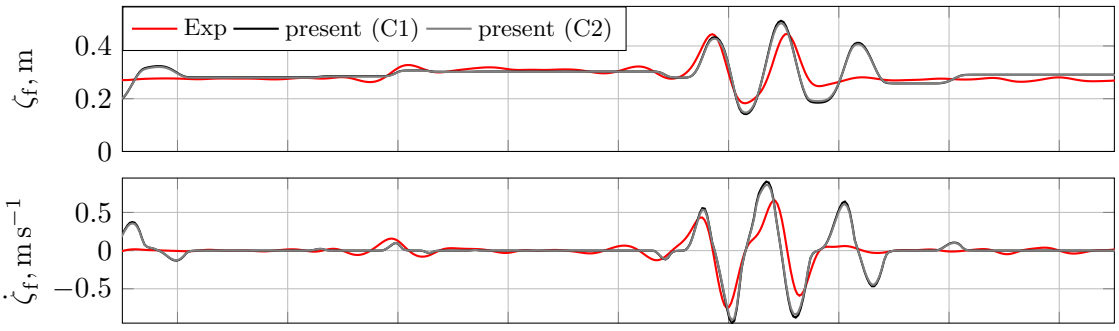

(b) Vertical fender displacement ζ_f and velocity $\dot{\zeta}_f$.

Figure 5.23.: Comparison of the boat-landing maneuver simulation (present) of catamaran *Model 2* in irregular waves (JONSWAP: $H_s = 0.125\,\mathrm{m}$, $\omega_p = 4.4\,\mathrm{rad\,s^{-1}}$, $\nu_w = 15°$) with experiments (Exp).

6. Conclusion and Outlook

In the present work, a numerical method for the simulation of a boat-landing maneuver at offshore platforms has been presented. Common numerical approaches for the simulation of boat-landing maneuvers or other wave-body problems are either based on linear computations in the frequency domain which are fast but cannot handle non-linear effects, or on finite volume methods which are more sophisticated but require a great amount of computational effort. In contrast to this, the present approach is able to compute the boat-landing maneuver in the time domain considering the non-linear effects with a moderate effort regarding the modeling and the computation time.

The developed simulation method is based on the low-order boundary panel method *pan*MARE which solves the velocity potential for the fluid problem, and which was originally developed for the simulation of propeller flows. In addition to the treatment of the velocity potential, this work includes an approach to solve the acceleration potential. This is an important aspect of the free motion simulation of the catamaran regarding the computed hydrodynamic forces which particularly improves the numerical stability of the time integration of the motion. Furthermore, an approach for the consideration of the non-linear free surface has been derived. It is based on the mixed-Eulerian-Lagrangian method and it allows the simulation of wave-body interaction problems in the time domain. The incoming waves are considered as external potential using the analytic formulation for linear Airy waves or non-linear Stokes waves. Apart from this, an analytic formulation of the cylinder diffraction is implemented and the description of natural seaways is included as well via the spectral representation of irregular waves.

In addition to the hydrodynamic models, a simple fender contact model was developed and included to the simulation method. It efficiently solves the contact problem between the bow fender of the crew transfer vessel and the boat-landing structure. The model computes the reaction forces due to the deformation of the fender and it is able to describe the friction forces in the tangential direction of the contact plane. Here, the model distinguishes between static and kinematic friction and can therefore detect whether the fender slips or not during the landing maneuver.

Supplementary to the development of the numerical simulation approach, the boat-landing maneuver has been investigated experimentally. The tests provided validation data and helped to gain more insight into the important hydrodynamic interaction effects during the landing maneuver. In the first part of the experimental investigation, the hydrodynamic influence of a monopile was tested. A new approach to measure the wave elevation using optical infra-red cameras is presented. It allows evaluating the wave field in circumstance of the monopile and the diffraction effects. The second part of the experimental investigation deals with the boat-landing maneuver itself. Within these tests, the motion of the catamaran and the forces at the boat-landing were measured in regular and irregular waves. The encounter angles of the waves were varied by rotating the position of the boat-landing structure around the monopile center between 0° to 15°. Furthermore, the thrust of the catamaran propeller was varied in order to increase or decrease the contact forces between fender and boat-landing. Thus, both scenarios showing that the fender stays fixed or starts to slip during the maneuver could be considered.

The verification and validation of the developed numerical method is conducted considering several hydrodynamic problems. First, the numerical description of the non-linear free water surface and the simulation of wave-body interaction addressing the different hydrodynamic effects is validated. Results are evaluated for a submerged spheroid with forward speed and for the diffraction and the radiation problem of spheres below the free surface. Apart from this, free surface problems concerning surface piercing bodies are addressed. Here, the non-linear forces on a monopile in waves are validated and the diffraction effects are simulated in comparison with the tank test results. The results are also compared with published data from other non-linear methods and the comparison indicated a fair agreement. Furthermore, the seakeeping problem of a freely moving body is validated by the simulation of a Wigley hull with forward speed in head waves. Two different Wigley models are tested. The response amplitude operators of the hydrodynamic forces with constrained heave and pitch motion match very well with the validation data from published experimental investigations.

The boat-landing maneuver is validated on the basis of the experimental data from the tank tests. Here, two different crew transfer vessels are tested in regular and irregular waves. The response amplitude operators for the motion in regular waves are compared for a freely-moving catamaran in the circumstance of the monopile and for a catamaran in contact with the boat-landing structure. Furthermore, the validation is done for the boat-landing maneuver in irregular waves. In general, the results are satisfactory as the motion of the vessel fairly match the tank test results and the results further prove that the simulation approach is able to forecast the occurrence of slip during the maneuver.

In conclusion, a numerical method for the simulation of a boat-landing maneuver is developed of which numerical effort regarding the setup and the computation is relatively small compared to more sophisticated fluid-structure interaction approaches using finite volume methods. Furthermore, it has been demonstrated within the presented work that the developed method can consider non-linear effects, and that it is a suitable and

efficient approach to simulate the safety relevant aspects of the maneuvers at offshore platforms.

However, improvements regarding the accuracy and the numerical stability of the approach should be taken into account for future work. In this context, using higher-order panels for the solution of the boundary value problem is desirable. This would allow the usage of coarser grids and it would overcome the problem at the body waterline, as higher-order panels would provide a solution of the potential not only at the panel center but also at the corners and at the middle of each edge of the panel. It is to be expected that this would significantly increase the accuracy and the numerical stability of the method.

Another aspect to improve the approach regarding the non-linear water surface is the treatment of the external wave potential when evaluating the properties at the free surface panels. Due to the non-linearity of the boundary conditions, the values are determined at the current elevation position which may be outside the definition domain of the respective wave potential. In order to overcome this problem, an approach to expand the definition range should be implemented.

Furthermore, a condition for the transom stern of ships should be aimed. Apart from the simulation of boat-landing maneuvers, this would also allow the investigation of added resistance problems of crew transfer vessels during the transfer of personnel and equipment from the harbor to the wind farm. Another important aspect to improve the present method is related to the propeller flow as the thrust force, by which the fender of the crew transfer vessel is pushed against the boat-landing structure. The actual thrust of the propulsion depends on the environmental conditions as well as the inflow due to current and waves, but also the distance to the free surface may have a strong effect, for example when the propeller starts to ventilate. Therefore, numerical models should be included to consider these effects on the thrust of the catamaran. In addition to this, computations with more sophisticated fluid-structure interaction approaches should be conducted in order to compare the results with the developed method and, thus, improve the approach in the following.

Full scale or model scale tests provide essential data which help to validate and improve numerical methods. Therefore, future work should further focus on experimental investigation of the boat-landing maneuver considering also promising concepts, e.g. heave compensation platforms, that may increase the accessibility of offshore plants and the safety during the boat-landing maneuver. In addition to this, the effects between the propeller thrust, the waves and the ship motion are of interest and should be particularly regarded in model tests to learn how they interact in detail and how to take advantage of the interaction effects.

Bibliography

Abramowitz, M. and I. A. Stegun, eds. (1965). *Handbook of mathematical functions with formulas, graphs, and mathematical tables*. 4. printing, December 1965, with corrections. National Bureau of Standards applied mathematics series. Originally issued 1964. - Erscheint auch als Reprint beim Verl. Dover, New York u.d.T.: Handbook of mathematical functions. Washington, D.C.: Superintendent of Documents, U.S. Gov. Print. Off.

Bandyk, P. J. and R. F. Beck (2011). "The acceleration potential in fluid–body interaction problems". In: *Journal of Engineering Mathematics* 70.1, pp. 147–163.

Bauer, M. and M. Abdel-Maksoud (2012). "A 3-D Potential Based Boundary Element Method for the Modelling and Simulation of Marine Propeller Flows". In: *7th Vienna International Conference on Mathematical Modelling*. Vol. **7**.

Cao, Y. and R. F. Beck (2016). "Desingularized boundary integral equations and their applications in wave dynamics and wave–body interaction problems". In: *Journal of Ocean Engineering and Science* 1.1, pp. 11–29.

Cao, Y., W. W. Schultz, and R. F. Beck (1991a). "Three-dimensional desingularized boundary integral methods for potential problems". In: *International Journal for Numerical Methods in Fluids* 12.8, pp. 785–803.

– (1991b). "Three-dimensional, unsteady computations of nonlinear waves caused by underwater disturbances". In: *Eighteenth Symposium on Naval Hydrodynamics*. Vol. 1, pp. 417–425.

Celebi, M. and M. Kim (1997). "Nonlinear wave body interactions in a numerical wave tank". In: *Proceedings of the 12th International Workshop on Water Waves and Floating Bodies, France*, pp. 25–29.

Chakrabarti, S. K. (1987). *Hydrodynamics of Offshore Structures*. Computational Mechanics Publications and Springer-Verlag.

Clauss, G., E. Lehmann, and C. Östergaard (2014). *Offshore structures: volume I: conceptual design and hydromechanics*. Springer.

Dold, J. (1992). "An efficient surface-integral algorithm applied to unsteady gravity waves". In: *Journal of Computational Physics* 103.1, pp. 90–115.

Dommermuth, D. G. and D. K. Yue (1987). "Numerical simulations of nonlinear axisymmetric flows with a free surface". In: *Journal of Fluid Mechanics* 178, pp. 195–219.

Faltinsen, O. M. (1977). "Numerical Solutions of Transient Nonlinear Free-Surface Motion Outside or Inside Moving Bodies". In: *2nd International Conference on Numerical Ship Hydrodynamics*.

Faltinsen, O., J. Newman, and T. Vinje (1995). "Nonlinear wave loads on a slender vertical cylinder". In: *Journal of Fluid Mechanics* 289, pp. 179–198.

Farell, C. (1973). "On the Wave Resistance of a Submerged Spheroid". In: *Journal of Ship Research* 17, pp. 1–11.

Fenton, J. D. (1985). "A fifth-order Stokes theory for steady waves". In: *Journal of waterway, port, coastal, and ocean engineering* 111.2, pp. 216–234.

Ferrant, P. (1999). "Fully Nonlinear Interactions of Long-Crested Wave Packets with a Three-Dimensional Body". In: *Twenty-Second Symposium on Naval Hydrodynamics*.

Ferrant, P., D. L. Touzé, and K. Pelletier (2003). "Non-linear time-domain models for irregular wave diffraction about offshore structures". In: *International Journal for Numerical Methods in Fluids* 43.10-11, pp. 1257–1277.

Ferziger, J. H., M. Peri, and R. L. Street (2002). *Computational methods for fluid dynamics*. Vol. 3. Springer.

Greve, M. (2015). "Non-viscous calculation of propeller forces under consideration of free surface effects". PhD thesis. Hamburg University of Technology.

Hasselmann, K., T. Barnett, E. Bouws, H. Carlson, D. Cartwright, K. Enke, J. Ewing, H. Gienapp, D. Hasselmann, P. Kruseman, et al. (1973). "Measurements of wind-wave growth and swell decay during the Joint North Sea Wave Project (JONSWAP)". In: *Hydraulic Engineering Reports*. Deutches Hydrographisches Institut.

Havelock, T. H. (1940). "The pressure of water waves upon a fixed obstacle". In: *Proceedings of the Royal Society of London. Series A. Mathematical and Physical Sciences* 175.963, pp. 409–421.

Hedges, T. (Jan. 1995). "Regions of validity of analytical wave theories". In: *Proceedings of The Ice - Water Maritime and Energy*. Vol. 112, pp. 111–114. DOI: 10.1680/iwtme.1995.27656.

Hess, J. and A. Smith (1962). *Calculation of non-lifting potential flow about arbitrary three-dimensional bodies*. Tech. rep. E.S. 40622. Douglas Aircraft Company, Inc.

Isaacson, M. D. S. Q. (1982). "Nonlinear-wave effects on fixed and floating bodies". In: *Journal of Fluid Mechanics* 120, pp. 267–281.

Kashiwagi, M. (2013). "Hydrodynamic study on added resistance using unsteady wave analysis". In: *Journal of Ship Research* 57.4, pp. 220–240.

Katz, J. and A. Plotkin (2001). *Low-Speed Aerodynamics*. 2nd. Cambridge Aerospace Series 13. Cambridge University Press.

Kim, K.-H. and Y. Kim (2011). "Numerical study on added resistance of ships by using a time-domain Rankine panel method". In: *Ocean Engineering* 38.13, pp. 1357–1367.

Kim, M., M. Celebi, and D. Kim (1998). "Fully nonlinear interactions of waves with a three-dimensional body in uniform currents". In: *Applied Ocean Research* 20.5, pp. 309–321.

Kim, M. W., W. Koo, and S. Y. Hong (2014). "Numerical analysis of various artificial damping schemes in a three-dimensional numerical wave tank". In: *Ocean Engineering* 75, pp. 165–173.

Kim, M.-H. and D. K. P. Yue (1989). "The complete second-order diffraction solution for an axisymmetric body Part 1. Monochromatic incident waves". In: *Journal of Fluid Mechanics* 200, pp. 235–264.

Kim, Y., K.-H. Kim, J.-H. Kim, T. Kim, M.-G. Seo, and Y. Kim (2011). "Time-domain analysis of nonlinear motion responses and structural loads on ships and offshore structures: development of WISH programs". In: *International Journal of Naval Architecture and Ocean Engineering* 3.1, pp. 37–52.

König, M., D. Ferreira González, M. Abdel-Maksoud, and A. Düster (2017). "Numerical investigation of the landing manoeuvre of a crew transfer vessel to an offshore wind turbine". In: *Ships and Offshore Structures* 12.sup1, pp. 115–133. DOI: 10.1080/17445302.2016.1265883. eprint: https://doi.org/10.1080/17445302.2016.1265883. URL: https://doi.org/10.1080/17445302.2016.1265883.

Koo, W. and M.-H. Kim (2004). "Freely floating-body simulation by a 2D fully nonlinear numerical wave tank". In: *Ocean Engineering* 31.16, pp. 2011–2046.

Krogstad, J. R. and C. T. Stansberg (1995). "Ringing Load Models Verified Against Experiments". In: *Proceedings of the 14th International Conference on Offshore Mechanics and Arctic Engineering, OMAE 1995 : Copenhagen, Denmark*. Vol. 1. New York: American Society of Mechanical Engineers.

Lewandowski, E. M. (2004). *The dynamics of marine craft: maneuvering and seakeeping*. Ed. by P. L.-F. Liu. Vol. 22. World scientific.

Liu, Y., M. Xue, and D. K. Yue (2001). "Computations of fully nonlinear three-dimensional wave–wave and wave–body interactions. Part 2. Nonlinear waves and forces on a body". In: *Journal of Fluid Mechanics* 438, pp. 41–66.

Longuet-Higgins, M. S. and E. Cokelet (1976). "The deformation of steep surface waves on water. I. A numerical method of computation". In: *Proceedings of the Royal Society of London A: Mathematical, Physical and Engineering Sciences*. Vol. 350. The Royal Society, pp. 1–26.

Lui, Y., B. Teng, P.-w. Cong, C.-f. Liu, and Y. Gou (2012). "Analytical study of wave diffraction and radiation by a submerged sphere in infinite water depth". In: *Ocean Engineering* 51, pp. 129–141.

Luo-Theilen, X. and T. Rung (2017). "Computation of mechanically coupled bodies in a seaway". In: *Ship Technology Research* 64.3, pp. 129–143.

Mccamy, R. and R. Fuchs (1954). *Wave forces on piles: a diffraction theory*. Tech. rep. TM-69. Corps of engineers Washington DC beach erosion board.

Mei, C. C. (1989). *The applied dynamics of ocean surface waves*. Vol. 1. World scientific.

Moore, D. (1983). "Resonances introduced by discretization". In: *IMA Journal of Applied Mathematics* 31.1, pp. 1–11.

Newman, J. N. (1986). "Distributions of sources and normal dipoles over a quadrilateral panel". In: *Journal of Engineering Mathematics* 20.2, pp. 113–126.

Popov, V. L. (2010). *Contact mechanics and friction*. Springer.

Proceedings of the 26th International Towing Tank Conference (2011). Vol. I.

Proceedings of the 27th International Towing Tank Conference (2013). Vol. I.

Sichermann, W. (2008). "Zur Simulation und Vorhersage extremer Schiffsbewegungen im natürlichen Seegang". PhD thesis. Hamburg University of Technology.

Söding, H. (2004). "How to integrate free motions of solids in fluids". In: *4th International Towing Tank Symposium*.

– (2019). "A potential method for fully non-linear wave respones of ships". In: *11th International Workshop on Ship and Marine Hydrodynamics*.

– (2020). "Fast accurate seakeeping predictions". In: *Ship Technology Research* 67.3, pp. 121–135. DOI: 10.1080/09377255.2020.1761618. eprint: https://doi.org/10.1080/09377255.2020.1761618. URL: https://doi.org/10.1080/09377255.2020.1761618.

Söding, H. and V. Bertram (2009). "A 3-D Rankine source seakeeping method". In: *Ship Technology Research* 56.2, pp. 50–68.

Sun, H. (May 2007). "A boundary element method applied to strongly nonlinear wave-body interaction problems". PhD thesis. Norwegian University of Science and Technology, Trondheim.

Teng, B. and R. E. Taylor (1995). "New higher-order boundary element methods for wave diffraction/radiation". In: *Applied Ocean Research* 17.2, pp. 71–77.

Tucker, M. J. and E. G. Pitt (2001). *Waves in ocean engineering*. Ed. by R. Bhattacharyya and M. McCormick. Volume 5. Elsevier.

WindEurope (2020). *Offshore wind in Europe - key trends and statistics 2019*. URL: https://windeurope.org/wp-content/uploads/files/about-wind/statistics/WindEurope-Annual-Offshore-Statistics-2019.pdf.

Xue, M., H. Xü, Y. Liu, and D. K. Yue (2001). "Computations of fully nonlinear three-dimensional wave–wave and wave–body interactions. Part 1. Dynamics of steep three-dimensional waves". In: *Journal of Fluid Mechanics* 438, pp. 11–39.

Yang, W., W. Tian, K. Wei, Z. Peng, and Z. Huang (2019). "Research on a cost-effective measure dedicated to stabilizing offshore wind farm crew transfer vessels". In: *Renewable Energy* 133, pp. 275–283. ISSN: 0960-1481.

Zhang, X., P. Bandyk, and R. F. Beck (2010a). "Seakeeping computations using double-body basis flows". In: *Applied Ocean Research* 32.4, pp. 471–482.

Zhang, X., P. Bandyk, and R. F. Beck (2010b). "Time-domain simulations of radiation and diffraction forces". In: *Journal of Ship Research* 54.2, pp. 79–94.

A. Appendix

A.1. Experimental Results of Cylinder Diffraction

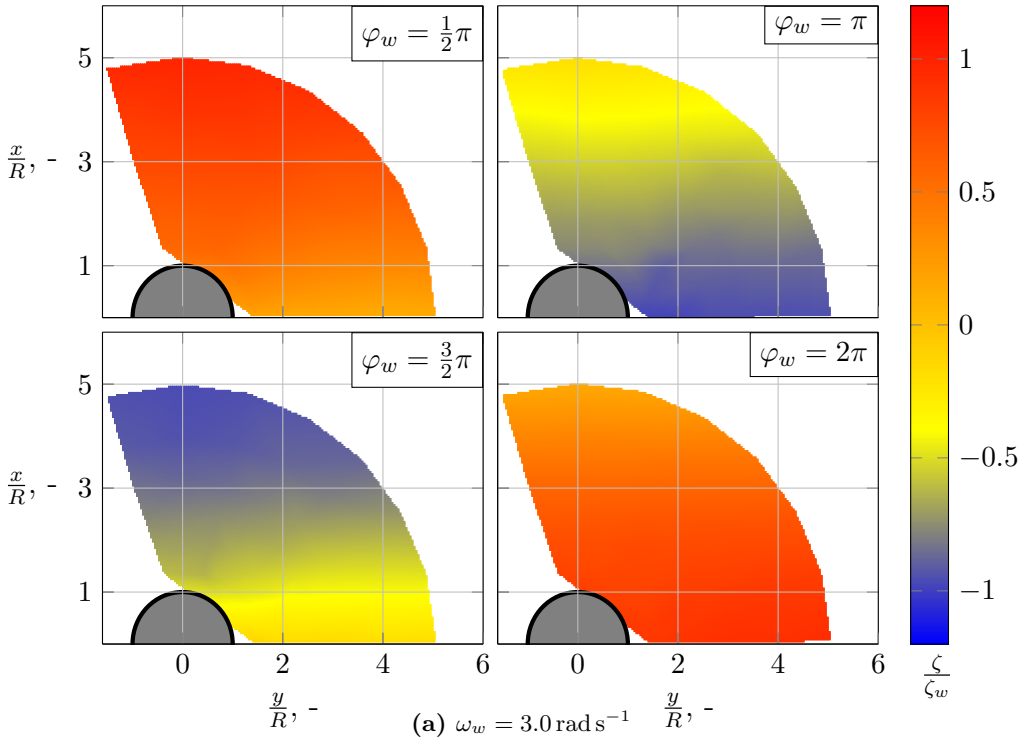

(a) $\omega_w = 3.0\,\mathrm{rad\,s^{-1}}$

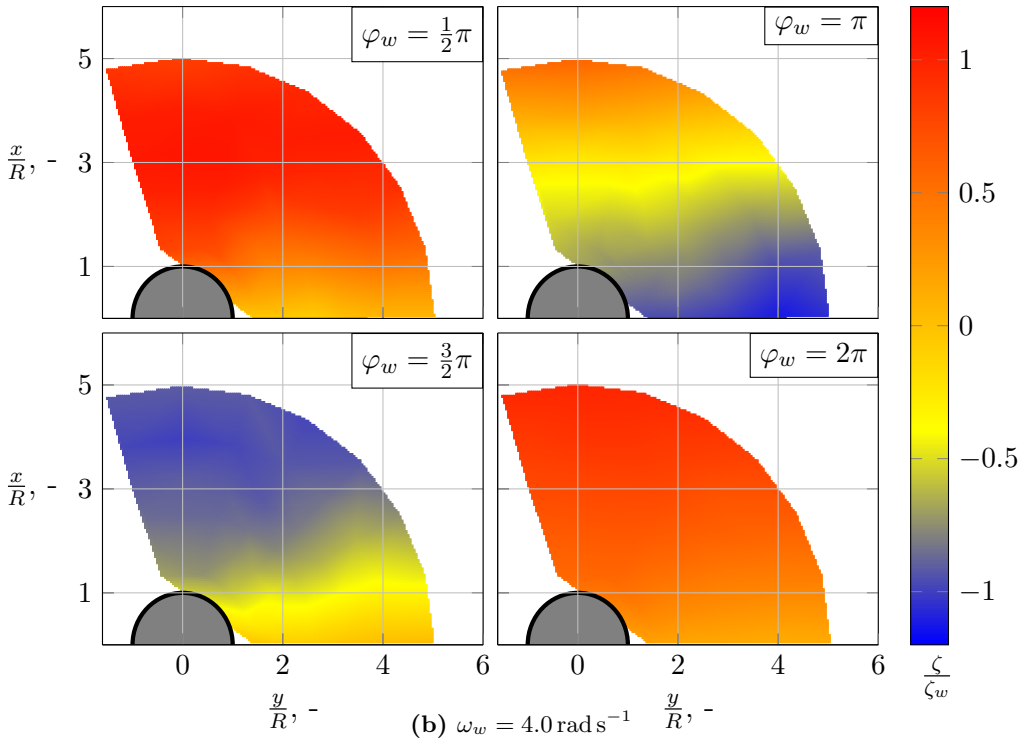

(b) $\omega_w = 4.0\,\mathrm{rad\,s^{-1}}$

Figure A.1.: Results of the water elevation $\zeta/\hat{\zeta}_w$ in circumstance of the cylinder in regular waves ($\hat{\zeta}_w = 0.05\,\mathrm{m}$) from experimental measurements.

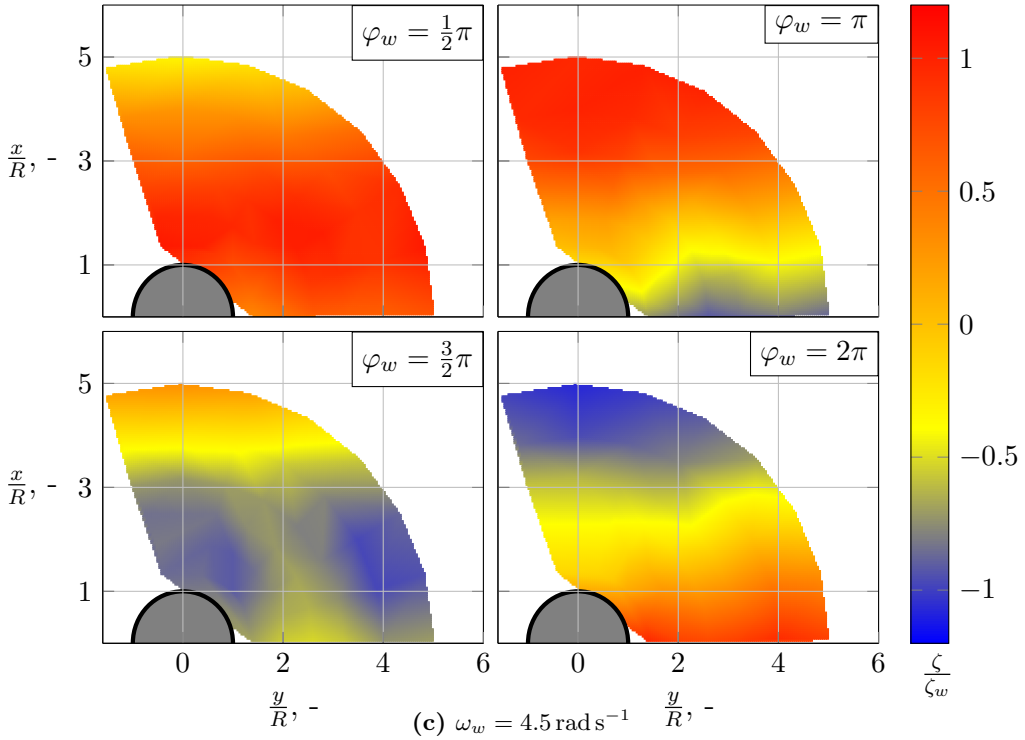

(c) $\omega_w = 4.5\,\mathrm{rad\,s^{-1}}$

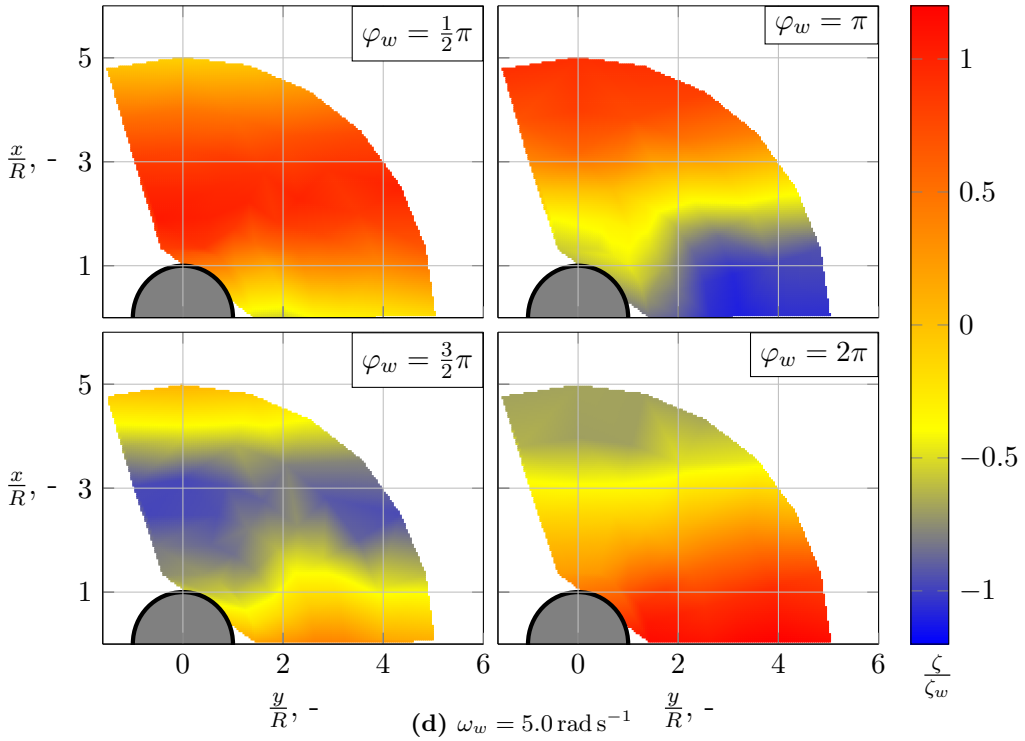

(d) $\omega_w = 5.0\,\mathrm{rad\,s^{-1}}$

Figure A.1.: Results of water elevation $\zeta/\hat{\zeta}_w$ in circumstance of the cylinder in regular waves ($\hat{\zeta}_w = 0.05\,\mathrm{m}$) from experimental measurements.

A.2. Simulation of Boat Landing Maneuvers

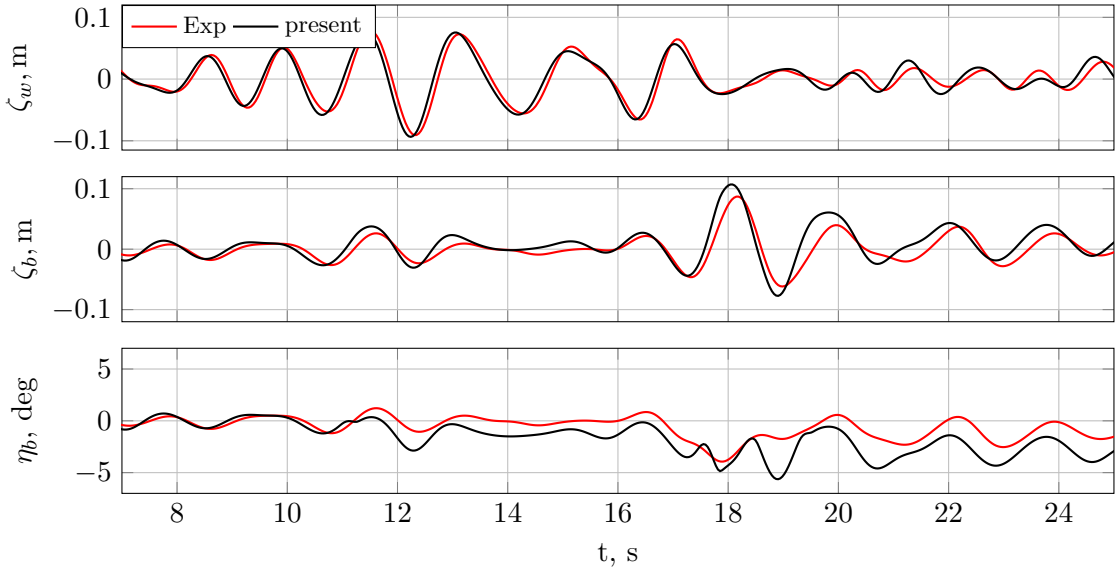

(a) Wave elevation ζ_w, heave motion ζ_b and pitch motion η_b of the catamaran model.

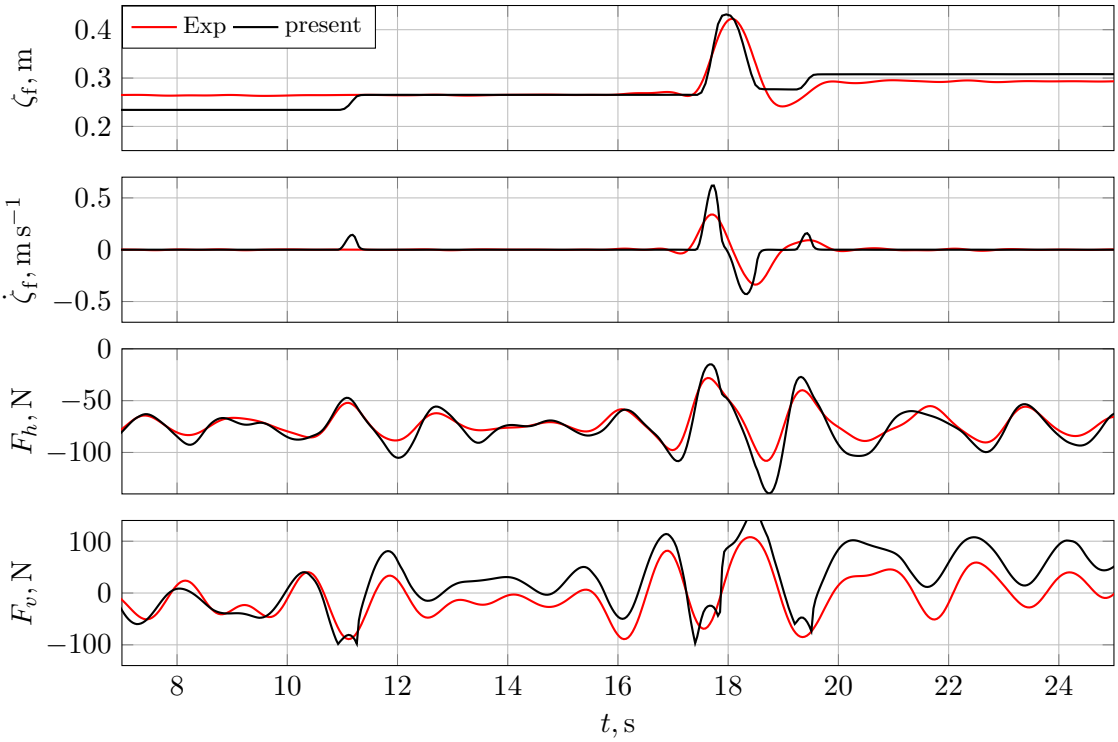

(b) Vertical fender displacement ζ_f and velocity $\dot{\zeta}_f$, horizontal F_h and vertical force F_v at fender.

Figure A.2.: Comparison of the boat landing maneuver simulation (present) of catamaran *Model 2* in irregular waves (JONSWAP: $H_s = 0.125\,\mathrm{m}$, $\omega_p = 3.31\,\mathrm{rad\,s^{-1}}$,$\nu_w = 0°$) with experiments (Exp).

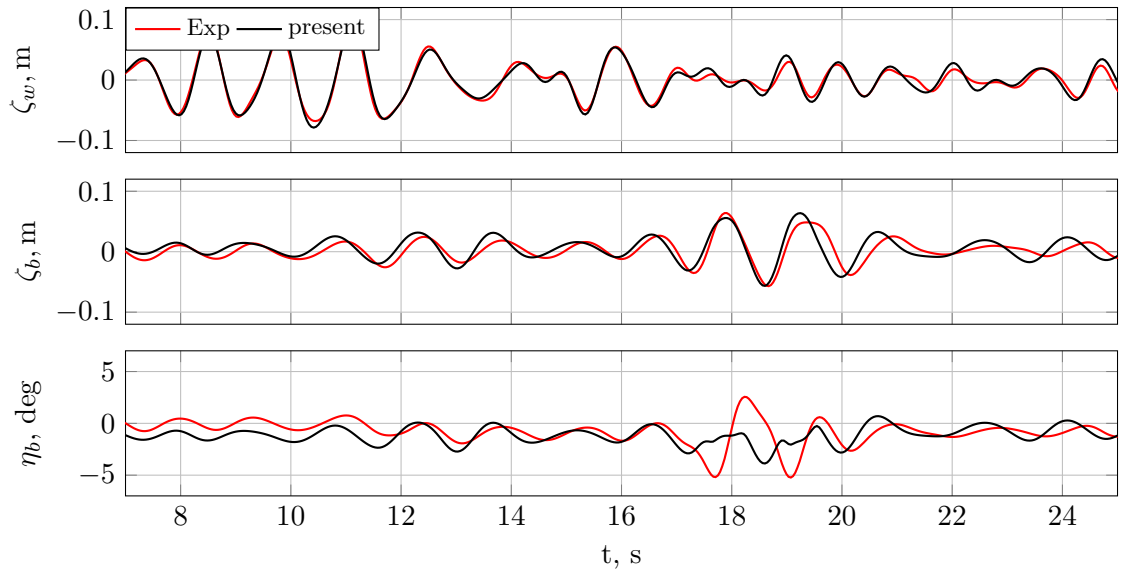

(a) Wave elevation ζ_w and motion of the catamaran model in heave ζ_b and pitch η_b.

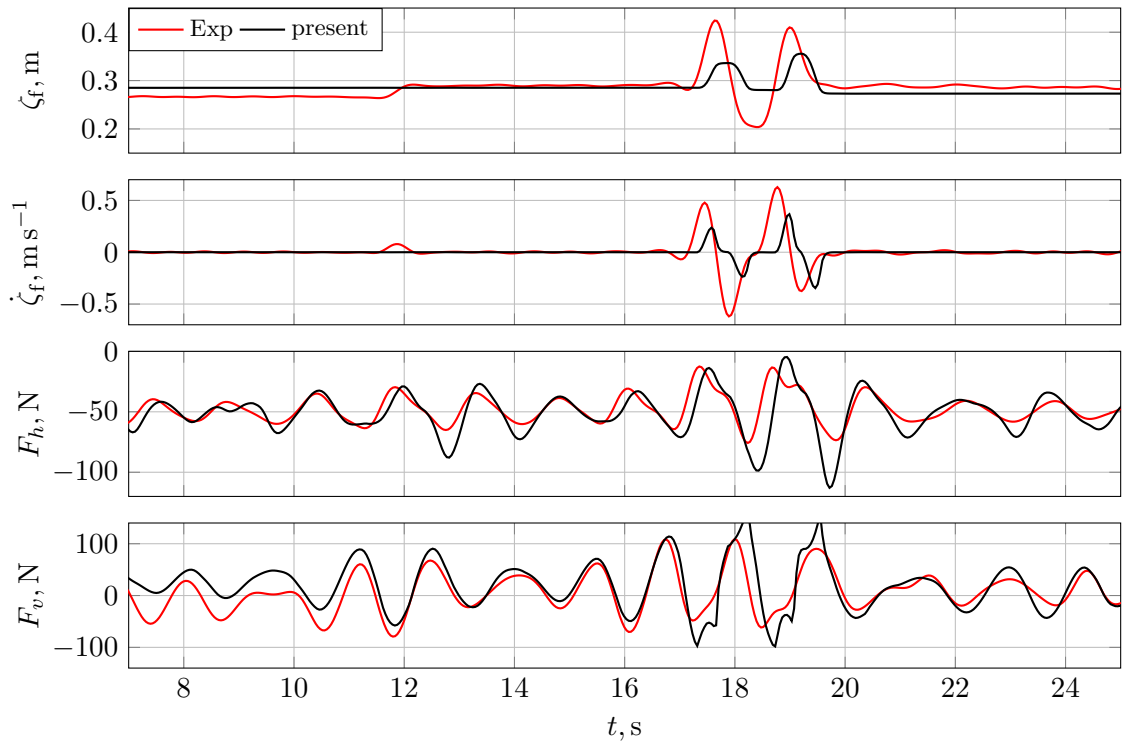

(b) Vertical fender displacement ζ_f and velocity $\dot{\zeta}_f$, horizontal F_h and vertical force F_v at fender.

Figure A.3.: Comparison of the boat landing maneuver simulation (present) of catamaran *Model 2* in irregular waves (JONSWAP: $H_s = 0.125\,\mathrm{m}$, $\omega_p = 4.4\,\mathrm{rad\,s^{-1}}$,$\nu_w = 0°$) with experiments (Exp).